

Irrigation lateral hydraulic simulation model based on the gradient method

D. Zerihun and C.A. Sanchez
University of Arizona
Maricopa Agricultural Center
37860 W. Smith-Enke Rd.
Maricopa, Arizona 85138

Internal report
August, 2016

Content

Chapter 1. Introduction	9
Chapter 2. Basic pipeline hydraulics, a review	12
2.1. Flow in a flow-through pipe segment, steady-state condition	13
2.2. Equations for computing friction head loss	14
2.3. Equations for computing local head losses	16
Chapter 3. Lateral hydraulics, simulation: problem description and formulation with the gradient method	17
3.1. Description of a lateral as a hydraulic network	17
3.2. Schematics of lateral hydraulic computational elements	18
3.3. Pipe network computational methods	19
3.4. Problem fomulation with the gradient method	22
3.4.1. Link energy balance	23
3.4.2. Continuity at junction nodes	27
3.4.3. System of Equations	28
Chapter 4. Lateral hydraulics, simulation: Numerical solution with the gradient method	35
4.1. Iterative solution	35
4.2. Initialization of variable vectors and updating matrices in each gradient iteration	44
4.2.1. Initialization of the system variable vectors, \mathbf{Q} and \mathbf{H}	44
4.2.2. Constant vectors \mathbf{q} and \mathbf{H}_0	44
4.2.3. Network connectivity matrices Ψ_{10} , Ψ_{12} , and Ψ_{21} and the vector $\Psi_{10}\mathbf{H}_0$	44
4.2.4. Computation of the Ψ_{11} matrix (Table 6 and Eq. 29) at the $(m+1)th$ iteration	45
4.2.5. Computation of the Ψ'_{11} matrix (Table 8 and Eq. 33) at the $(m+1)th$ iteration	46

4.2.6. Computation of the inverses of the $(\Psi'_{11})^n$ and	
$\left(\Psi_{21} \left[(\Psi'_{11})^n \right]^{-1} \Psi_{12} \right)$ matrices	49
4.3. Numerical algorithm	50
4.4. Model inputs and outputs	55
Chapter 5. Model evaluation	55
5.1. Data description	55
5.2. Consistency test of the numerical solution implemented in the model	57
5.2.1. Test factors and criterion	57
5.2.2. Results of consistency test	59
5.3. Comparison of the current lateral hydraulic model with that based on manifold hydraulics	62
5.3.1. Introductory discussion	62
5.3.2. Results of model comparison	63
5.4. Comparison of the lateral hydraulic model with EPANET	67
5.4.1. Introductory discussion	67
5.4.2. Results of model comparison	68
5.5. Model evaluation with measured data	73
5.6. Sensitivity analysis	75
5.6.1. Introductory discussion	75
5.6.2. Lateral slope	76
5.6.3. Lateral diameter	80
5.6.4. Lateral pipe absolute roughness	82
Chapter 6. Summary and Conclusion	85
References	88
Appendix I. Derivation of expressions for the elements of the inverse of the Jacobian matrix	91
Appendix II. Algorithm for iterative computation of the Darcy-Weisbach friction factor	93

Appendix III. Algorithm for computing the Ψ_{II} matrix at the $(m+1)th$ gradient iteration	95
Appendix IV. Algorithm for computing the Ψ'_{II} matrix at the $(m+1)th$ iteration	97
Appendix V. Expressions for the derivatives of the friction factor with respect to pipe segment discharge	99
Appendix VI. Computation of the inverse of a matrix with LU factorization	101
Appendix VII. The effect of lateral slope on the broad spatial trends of lateral pressure head	107

List of Tables

Table 1. A system of equations describing flow in a lateral with n_l links (pipe segments and emitters) and n_l+1 nodes, Eqs. 19 and 21	30
Table 2. A system of equations describing flow in a lateral with n_l links and n_l+1 nodes, partitioned for block matrix representation as shown in Eq. 23	31
Table 3. Hydraulic network topological incidence matrix (network connectivity matrix), Ψ	32
Table 4. Hydraulic network connectivity matrix, Ψ_{2l}	33
Table 5. A system of equations describing flow in a lateral with n_l links and n_l+1 nodes, partitioned for block matrix representation as shown in Eq. 27	34
Table 6. Matrix representation of the nonlinear system of equations (Eq. 29)	36
Table 7. A system of nonlinear equations describing flow in a lateral with n_l links and n_l+1 nodes, partitioned for block matrix representation as shown in Eq. 30	38
Table 8. Matrix representation of the linear system of equations solved in each Newton iteration, Eq. 33	40
Table 9. Data used in model evaluation	56

List of Figures

- Figure 1. Schematic of irrigation lateral pipe configuration and components of specific mechanical energy along a lateral (Notations: D is lateral diameter (m); Q is discharge (L/s); h is pressure head (m); h_f is friction head loss (m); g is gravitational acceleration (m/s^2); S_L is emitter spacing along lateral (m); n_l is number of hydraulic links (lateral pipe segments and emitters) (-); L is lateral length (m); V is average cross-sectional flow velocity (m/s); Z is nodal elevation (m); a and b are upstream and downstream end sections of lateral, respectively; HGL is hydraulic grade line; and EGL is energy grade line) 10
- Figure 2. Components of specific energy and energy loss in a pipe without outlets 13
- Figure 3. Friction factor for pipe flow 15
- Figure 4. (a) Schematics of a lateral as a branched hydraulic network with n_l hydraulic links and n_l+1 nodes and (b) Schematization of energy relations across an emitter or riser-emitter ensemble (Notations: $(.)$ is node index and $[.]$ is link index, H is total head [m], and V is velocity in the lateral segment just upstream of a junction node and the stream exit velocity at the emitter (m/s), note that discharges are subscripted with link indices and heads are subscripted with node indices) 19
- Figure 5. Junction node along a lateral with a riser-emitter ensemble (Notations: $[.]_j^u$, $[.]_j^d$, and $[.]_k$ are components of nodal specific energy and flow velocity at points immediately upstream and downstream of node j and at the boundary node k , respectively, and q_j is constant supply or demand at the junction node) 24
- Figure 6. Flow chart depicting the gradient algorithm implemented in the lateral hydraulic model (where m is gradient iteration index; \mathbf{Q} and \mathbf{H} are link discharge and nodal continuity vectors, respectively; \mathbf{H}_0 and \mathbf{q} are fixed nodal heads and discharge vectors, respectively; Ψ_{10} , Ψ_{12} , Ψ_{21} are network connectivity matrices; Ψ_{11} and Ψ_{11}' are matrices in Eqs. 29 and 33, respectively; \mathbf{F}_e and \mathbf{F}_c are residuals of the link energy balance and nodal continuity equations, respectively; $step$ is index of intermediate computational steps; and Θ_1 - Θ_5 are variables for representing intermediate outputs) 52

- Figure 7. Simplified flow chart showing the sequence of matrix computations for determining the system variables Q and H at the $(m+1)th$ gradient iteration (where: $step$ is index for intermediate computational steps; Ω_1 to Ω_{10} and Θ_1 to Θ_5 are labels for representing intermediate outputs; Note: Details of matrix operations relating to the computation of the inverse of a matrix, as implemented in the current model, are presented in Appendix VI) 54
- Figure 8. Graphs showing percent differences between model computed and manually calculated hydraulic variables and parameters, expressed as percentage of the manually calculated values: (a) Percent difference in friction factor, δf , (b) Percent difference in sprinkler discharge, δQ_s , (c) Percent difference in lateral discharge, δQ , and (d) Percent difference in total nodal head, δH 60
- Figure 9. Comparison of lateral pressure heads, h , and sprinkler discharges, Q_s , computed with the lateral hydraulic simulation model, developed based on the gradient method, and that based on the manifold method: (a) Data set 1, (b) Data set 2, (c) Data set 3, (d) Data set 4, and (e) Data set 5 64
- Figure 10. Graphs depicting comparisons of the lateral hydraulic simulation model, presented here, with a model based on manifold hydraulics and with EPANET: (a) Percent differences between lateral pressure heads computed with the gradient and manifold models, δh , (b) Percent differences between sprinkler discharges computed with the gradient and manifold models, δQ_s , (c) Percent differences between lateral pressure heads computed with the lateral hydraulic simulation model and EPANET, δh , and (d) Percent differences between sprinkler discharges computed with the lateral hydraulic model and EPANET, δQ_s 66
- Figure 11. Comparison of lateral pressure heads, h , and sprinkler discharges, Q_s , computed with the lateral hydraulic simulation model and EPANET: (a) Data set 1, (b) Data set 2, (c) Data set 3, (d) Data set 4, and (e) Data set 5 69
- Figure 12. Comparison of lateral pressure head computed with the lateral hydraulic simulation model, presented here, and measured data: (a) Data set 4, (b) Data set 5, (c) Data set 6, and (d) Data set 7 74
- Figure 13. Percent differences between field measured lateral pressure head profiles and those computed with the lateral hydraulic simulation model, δh , expressed as percentage of measurements 75

Figure 14. Sensitivity of (a) Lateral pressure head to lateral slope, (b) Sprinkler discharge to lateral slope, (c) Lateral pressure head to diameter, (d) Sprinkler discharge to diameter, (e) Lateral pressure head to pipe absolute roughness, and (f) Sprinkler discharge to pipe absolute roughness 77

Figure II.1. Flow chart for computing the Darcy-Weisbach friction factor, f , for the i th link (i.e., lateral pipe segment or riser pipe) evaluated based on the link discharge at the m th iteration, Q_i^m (where f^c is current estimate of f ; f^r is a revised estimate (computed in the $(j+1)$ th iteration) of f ; f_{fi} is the value of f for the i th lateral pipe segment when the flow is in the fully turbulent zone) 95

Figure III.1. Flow chart for updating the Ψ_{11} matrix at the $(m+1)$ th iteration based on the discharge vector at the m th iteration, \mathbf{Q}^m (where i is link index, f_i is the friction factor for the i th link computed iteratively based on the link discharge at the m th gradient iteration, and n_l is number of links in the lateral) 96

Figure V.1. Flow chart for updating the Ψ_{11}' matrix at the $(m+1)$ th iteration based on the discharge vector at the m th gradient iteration, \mathbf{Q}^m (where $F'_{eQ_i} \Big|_{Q_i^m}$ is the derivative of the i th link energy balance equation with respect to the i th link discharge evaluated based on Q_i^m ; and f'_i is the derivative of f with respect to the i th link discharge evaluated based on Q_i^m) 100

1. Introduction

Laterals constitute the basic elements of a pressurized irrigation hydraulic network. A lateral is a hydraulic manifold consisting of multiple outlets distributed along its length (Figure 1). The spacing between outlets of a lateral can be constant (as in the case of solid-set and set-move sprinkler systems) or variable (e.g., center-pivot systems). Lateral outlets are various emission devices, including sprinklers placed on the tip of riser pipes or hoses, which in turn are mounted onto laterals. They could also be emitters that are placed directly on the laterals as in the case of trickle systems. In solid-set and set-move sprinkler and trickle systems, laterals obtain their supply from a main or submain line. The hydraulic network of a continuous-move sprinkler system is typically composed of a single large diameter lateral that either rotates about a pivot point (center-pivot system) or moves in a straight line path (linear move systems). Water could be pumped into the field-scale system from a local surface or subsurface source or the system may obtain its supply from a larger pressurized distribution line through a hydrant. The model presented here can potentially be applied to a wide range of pressurized irrigation laterals. However, model evaluation reported in this document is based on laterals used in solid-set and set-move sprinkler systems.

Field-scale pressurized irrigation systems are designed and operated assuming a constant head and inflow at the system inlet and hence constant discharge at all points in the network for the duration of irrigation. Evidently, outlet discharges vary along a lateral or mainline, nonetheless, the discharge at any given outlet or within a segment of a lateral or a mainline, in between outlets, is invariant with time. At the scale of an irrigated field transient flow does occur, but it typically takes place only over short durations following valve opening or closure (e.g., when a pump is turned on or off). Hence, for regular irrigation operations flow in such systems can be described as steady and nonuniform without loss of generality. The preceding implies that forms of the energy conservation and mass continuity equations, applicable to steady incompressible flow (Granger, 1995; Larock et al., 2000; Boulos et al., 2006; Miller, 2009), can be used to describe the hydraulics of such systems.

Hydraulic modeling problems of field-scale pressurized irrigation systems consist of: (1) hydraulic design, (2) hydraulic simulation, and (3) hydraulic characterization. In a limited sense,

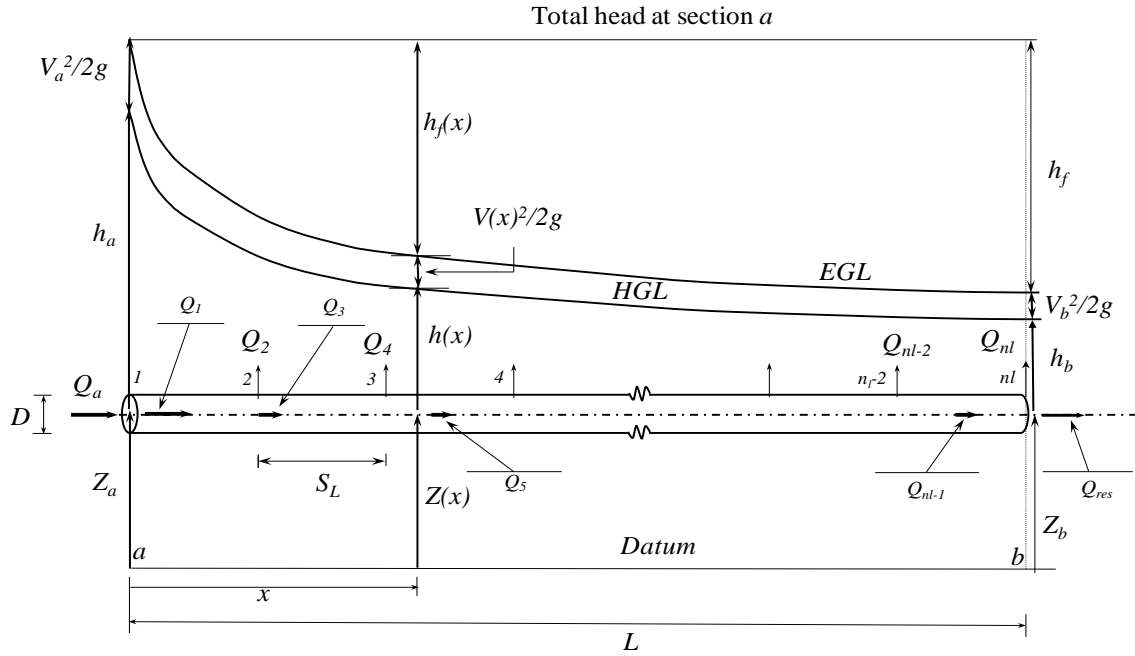


Figure 1. Schematic of irrigation lateral pipe configuration and components of specific mechanical energy along a lateral (Notations: D is lateral diameter (m); Q is discharge (L/s); h is pressure head (m); h_f is friction head loss (m); g is gravitational acceleration (m/s^2); S_L is emitter spacing along lateral (m); n_l is number of hydraulic links (lateral pipe segments and emitters) (-); L is lateral length (m); V is average cross-sectional flow velocity (m/s); Z is nodal elevation (m); a and b are upstream and downstream end sections of lateral, respectively; HGL is hydraulic grade line; and EGL is energy grade line)

hydraulic design of a field-scale pressurized irrigation network aims at sizing the network elements, including appurtenances such that the pressure and discharge variation in the irrigated field is maintained within a preset threshold, which is selected based on economic and irrigation uniformity considerations (e.g., Keller and Bliesner, 1990; Martin et al. 2007). Hydraulic simulations determine the field-scale spatial distribution of pressure and discharge, given the hydraulic, geometric, and topographic characteristics of the system, including the total head at the system inlet. Hydraulic characterization computations determine the system hydraulic characteristics at the inlet and the head-discharge curves at junction nodes, such as those of the intersection of the mainline and laterals. Hydraulic characterization computations are essentially repeated hydraulic simulations aimed at mapping the lateral downstream boundary conditions (specified in terms of pressure heads that vary within a preset range) to the corresponding lateral inlet head-discharge characteristics function (Zerihun and Sanchez, 2012).

Evidently, the design of laterals should be undertaken as part of the design of the entire field-scale pressurized irrigation system, which is outside the scope of the study presented here. Furthermore, hydraulic characterization computations are useful only if they are performed in the context of a field-scale pressurized irrigation system hydraulic simulation or design computations, a scale of analysis not envisaged in the current development. Thus the objective of the study reported here is limited to the formulation of the lateral hydraulic simulation problem, development of applicable numerical solutions, and model evaluation.

The formulation and numerical solution of the irrigation lateral hydraulic simulation problem, presented here, is based on an adaptation of the gradient method, developed originally for the simulation of pipeline networks with complex topologies. For computational purpose, an irrigation lateral is described here as a branched hydraulic network comprised of a series of interconnected links, each delimited by nodes. Lateral pipe segments and riser-emitter ensembles or emitters are considered as hydraulic links. The network nodes consist of junction nodes with unknown heads (marking the intersections of hydraulic links) and fixed head nodes, comprised of boundary nodes with externally imposed constant heads. Pipe appurtenances such as valves and fittings and other features that introduce local head losses are treated as properties of the lateral pipe segment they are placed on. Inline devices that add energy into or remove energy from the flow are not considered. A lateral segment (i.e., a flow-through pipe section connecting two consecutive emitters) is characterized by a single set of pipe diameter, slope, and hydraulic resistance parameter.

The energy balance and continuity equations for one-dimensional steady incompressible flow are used to describe the hydraulics of this system. The energy conservation equation is applied across each link and the continuity equation is written for each junction node in a lateral. These equations are then coupled to form a nonlinear system, which is partitioned for block matrix representation. The resultant system of equations are solved, for the variables (link discharges and nodal heads), iteratively with the Newton-Raphson method (e.g., Todini and Pilati, 1987; Nielson, 1989; Rossman, 2000; Lansley and Mays, 2000; Boulos et al., 2006; Estrada et al., 2009).

Evaluation of the lateral hydraulic simulation model, developed in the study reported here, is conducted at different levels. First the consistency of the numerical solution implemented in the model was tested by comparing intermediate and final outputs of the model with manual

calculations. Then outputs of the model are compared with outputs of EPANET (Rossman, 2000) and another model developed based on manifold hydraulics (Zerihun et al., 2014). The model is further evaluated based on comparisons of its outputs with field measured data. In addition, sensitivity analysis is conducted in order to evaluate the spatial patterns of model predicted lateral hydraulic characteristics under a range of conditions. Seven data sets, consisting of both hypothetical and field measured data, covering a wide range of lateral hydraulic, geometric, and slope conditions are used in model evaluation. The results of model evaluation suggest that the numerical algorithm, implemented in the lateral hydraulic simulation model presented here, is sound.

The study, presented in this report, is limited to the development of a hydraulic model that can simulate steady flow processes in irrigation laterals. However, the numerical solution developed here can be readily integrated into a field-scale pressurized irrigation system hydraulic characterization and simulation model, following the approach described by Zerihun et al. (2014).

This document has six chapters. Chapter 1 is the introduction section. Chapter 2 presents a concise description of the basic hydraulic principles/concepts and equations used to model steady flow processes in a pipe network, including the principles of energy conservation and mass continuity and the formulas used for computing friction and local head losses in pipes. In Chapter 3 a pressurized irrigation lateral is described as a branched hydraulic network (consisting of hydraulic links and nodes) and the formulation of the lateral hydraulic simulation problem with the gradient method is presented. In Chapter 4 the numerical solution of the lateral hydraulic simulation problem is developed. Chapter 5 presents model evaluation based on sensitivity analysis and comparisons of model outputs with field data and with outputs of existing models. Chapter 6 presents summary and conclusion.

2. Basic pipeline hydraulics, a review

The hydraulics of a field-scale pressurized irrigation system is a physical description of water flow through a branched (open) pipeline network, consisting of possibly a main, submains, and a lateral or laterals, each with multiple outlets. At the scale of an irrigated field, transient flow typically occurs only over short durations following valve opening or closure (e.g., when a pump is turned on or off). During regular irrigation operations outlet discharges vary along a lateral or

a mainline, nonetheless, discharge through a given outlet or in a segment of a lateral or a mainline, in between outlets, is invariant with time. Hence, for simulation, design, and operational purposes flow in such systems can be described as steady and nonuniform without loss of generality. The implication is that forms of the energy conservation and mass continuity equations, applicable to steady incompressible flow systems (Granger, 1995; Karney, 2000; Larock et al., 2000; Boulos et al. 2006; Miller, 2009), can be used to model the hydraulics of such systems. Evidently, flow in a lateral segment, in between outlets, is essentially the same as flow in flow-through pipe under steady conditions, hence in the next section the basic hydraulic principles/concepts and equations for steady flow in a flow-through pipe will be presented.

2.1. Flow in a flow-through pipe segment, steady-state condition

The hydraulics of a flow-through pipe is based on the principles of energy and mass conservation (Figure 2). The components of specific mechanical energy of the fluid (which is water) at any given point along a pipe consist of: elevation from reference datum to the center line of pipe, Z , the (gage) pressure head, h , and the kinetic energy per unit weight of water (velocity head, $V^2/2g$). The energy conservation equation for one dimensional steady incompressible flow written between any two sections along the pipe, e.g., sections a and b (Figure 2), states that the specific mechanical energy of water at section a should be equal to the

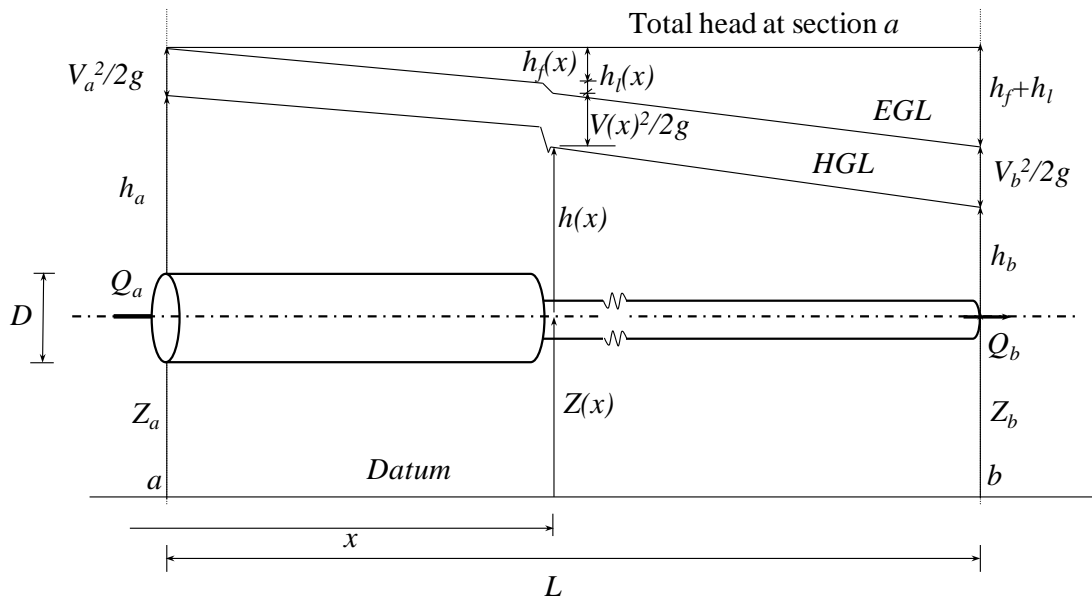


Figure 2. Components of specific energy and energy loss in a pipe without outlets

algebraic sum of the specific mechanical energy at section b and the friction head loss, h_f , and local head losses, h_l , between sections a and b :

$$Z_a + h_a + \frac{V_a^2}{2g} = Z_b + h_b + \frac{V_b^2}{2g} + h_f + h_l \quad (1)$$

If energy is added to the fluid in between sections a and b by a mechanical device such as a pump, it can be taken into account by adding it to the left-hand side expression of Eq. 1. For steady flow condition, the continuity equation applied to sections a and b of the flow-through pipe is

$$Q_a = Q_b \quad (2)$$

Although a third equation can be obtained from the application of the principle of momentum conservation (e.g., Karney, 2000), this equation is not used in the hydraulic simulation of field-scale pressurized irrigation pipe networks. Hence the momentum equation is not presented here.

2.2. Equations for computing friction head loss

The Darcy-Weisbach and the Hazen-Williams equations are commonly used to compute friction head loss, h_f (m), in sprinkler irrigation hydraulic applications (Keller and Bliesner, 1990; Martin et al., 2007). In the study presented here friction head loss is computed with the Darcy-Weisbach equation

$$h_f = k_l f \frac{Q^2}{D^5} L \quad (3)$$

where k_l is a dimensional constant $10^{7.917} \text{ mm}^5 \text{ s}^2 / \text{L}^2$, Q is discharge through the pipe segments (L/s), D is pipe diameter (mm), L is pipe length (m), and f is a dimensionless friction factor (-), which is a function of the surface roughness characteristics of the pipe material, the pipe diameter, and the Reynolds number, R_e (-). R_e is a dimensionless number used as a measure of the relative strengths of the inertial and viscous forces in the flow field

$$R_e = \frac{VD\rho}{\mu} = k_2 \frac{Q}{\nu D} \quad (4)$$

In Eq. 4, ρ is mass density of water (Kg/m^3), μ is dynamic viscosity of water (Kg/(ms)) which is a function of the water temperature, ν is kinematic viscosity of water (m^2/s), and k_2 is

dimensionless constant equal to $1.273 (m^2(mm)/L)$. Given pipe material and diameter, the relative roughness (defined as the ratio of the pipe absolute roughness, e , to pipe inside diameter, D) is used as a measure of the effect of pipe surface roughness on the friction factor, f (e.g., Keller and Bliesner, 1990; Larock et al., 2000). The relationship $f(R_e, e/D)$ is summarized in a logarithmic scale graph, the Moody diagram, Figure 3. The Moody diagram has four regions: the laminar, the critical, turbulent transition, and fully turbulent rough. In the laminar range ($R_e \leq 2000$) where viscous forces are dominant, energy loss is entirely due to internal (viscous) friction and the friction factor f is a function of R_e

$$f = \frac{64}{R_e} \quad (5)$$

The Darcy-Weisbach equation is in principle for turbulent flow, however, Eq. 5 is obtained by substituting, in Eq. 3, the head loss for laminar flow, expressed with the Hagen-Poiseuille equation, and solving the resulting expression for f (e.g., Marriott et al., 2009). Furthermore, when flow velocity increases to an extent that R_e exceeds 4000 (turbulent transition zone, Figure 3), the friction factor, f , becomes a function of both the Reynolds number and the relative roughness. Note that the turbulent transition zone is bounded by the dashed line at the top and the curve for smooth pipe at the bottom. In this zone, f is computed with the Colebrook-White equation, Eq. 6.

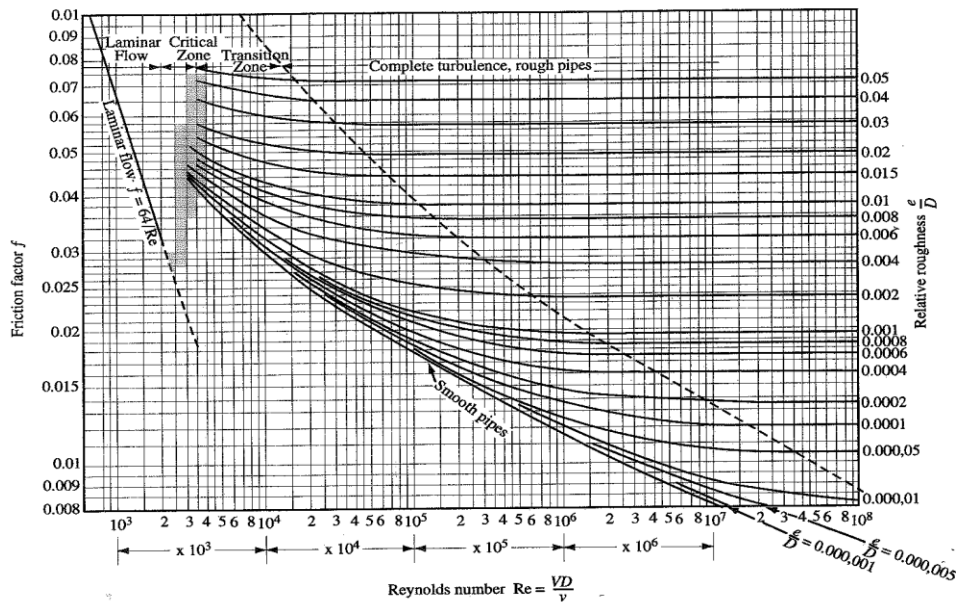


Figure 3. Friction factor for pipe flow

$$\frac{1}{\sqrt{f}} = 1.14 - 2 \log \left(\frac{e}{D} + \frac{9.35}{Re \sqrt{f}} \right) \quad (6)$$

With a further increase in the Reynolds number beyond a threshold that varies as a function of the relative roughness, shown by the dashed line in Figure 3, the flow is in the fully turbulent–rough zone. In this zone, the friction factor, f , is a function of the relative roughness, e/D , only (Figure 3). Hence, Eq. 6 simplifies to

$$\frac{1}{\sqrt{f}} = 1.14 - 2 \log \left(\frac{e}{D} \right) \quad (7)$$

For smooth pipes such as plastic with near zero relative roughness, which represents the lower limit of the turbulent transition zone (Figure 3), Eq. 6 reduces to

$$\frac{1}{\sqrt{f}} = 2 \log (Re \sqrt{f}) - 0.8 \quad (8)$$

As can be noted from Figure 3, the region between $2000 < Re \leq 4000$ is not covered in the moody diagram. Approximations of f in this range of Re may involve simply extending the curve for the laminar region through the range $2000 < Re \leq 4000$ or the use of interpolation schemes from the moody diagram. In the model presented here the simple approach of extending the laminar flow curve to the range $2000 < Re \leq 4000$ is used.

2.3. Equations for computing local head losses

Local head losses occur in pipe transitions (such as pipe contractions or expansions, fittings, tees, elbows, valves) where the flow is constrained, changes direction, or changes velocity and as a result turbulent eddies are generated and dissipated, in the process converting part of the mechanical energy to other forms of energy including heat. Local losses occur over finite distances, however, these distances cannot be readily determined, hence for practical applications they are typically assumed to occur essentially at a point (the location of the appurtenance). Generally local head losses are computed as a product of a local head loss coefficient, k_L , and the local velocity head

$$h_L = k_L k_3 \left(\frac{Q}{D^2} \right)^2 \quad (9)$$

In Eq. 9, k_3 is dimensional constant of the velocity head term, equivalent to $10^{4.917} \text{ mm}^4 \text{ m}(\text{s/L})^2$. The velocity head (discharge and diameter) typically used for computing local head losses is that just upstream of the pipe transition (e.g., Miller, 2009). However, if the local head loss is associated with reduction in pipe size, the velocity head typically used is the one in the downstream pipe segment (Granger, 1995). Furthermore, for changes in pipe diameters (pipe size reduction or increase), the local head loss coefficient is a function of the ratio of the upstream and downstream cross-sectional areas only (Keller and Bliesner, 1990; Granger, 1995). For other kinds of pipe transitions, given the type and geometry, local head loss coefficients in theory can vary as a function of the local Reynolds number, inflow and outflow conditions, and surface roughness (Miller, 2009). However, accurate determination of the effects of these factors for sprinkler system modeling applications is often impractical, hence they are typically treated as constant parameters that depend on the type and geometry of the pipe transition. They can be obtained from manufacturer's catalogue or from literature sources (e.g., Keller and Bliesner, 1990; Granger, 1995) or in principle can be determined through measurements.

3. Lateral hydraulics, simulation: problem description and formulation with the gradient method

3.1. Description of a lateral as a hydraulic network

For computational purposes a lateral is described here as a simple branched hydraulic network consisting of a series of interconnected links, each delimited by nodes. Any hydraulic network element (including valves, pumps) across which a head-discharge relationship exists can be treated as a link (Boulos et al., 2006). However, as an initial approximation only lateral pipe segments (i.e., sections of lateral pipe connecting two consecutive emitters) and riser-emitter ensembles (or emitters) are treated here as hydraulic links. Valves, couplers, bends, and other pipe appurtenances that introduce local head losses are treated as properties of the pipe segment they are placed on. In addition, inline devices that add energy into and/or remove energy from the system are not considered.

The network nodes consist of junction nodes (marking the intersections of hydraulic links) and fixed head nodes (i.e., nodes with externally imposed constant heads). In the current development, the points of intersection of the centerlines of the lateral and each riser-emitter ensemble or emitter represent the junction nodes. The heads at the junction nodes and the link discharges are the system variables and need to be determined as part of the numerical solution. Furthermore, in network hydraulics the junction nodes are also treated as points at which, externally imposed, constant inflows into or outflows from the system occur. However, in irrigation laterals these nodal discharges are typically zero, but an exception is made here for the downstream end node. Accordingly, the lateral considered here represents a more general scenario in which there is a constant residual outflow at the downstream end, Q_{res} (with $0 \leq Q_{res}$). The fixed head nodes represent boundary nodes, which include the inlet end of a lateral and the downstream ends of each riser-emitter ensemble or emitter. As will be shown subsequently each of these nodes have known constant heads.

Note that the term emitter is used here in the general sense to describe a water emission device commonly used in field-scale pressurized irrigation systems, including emitters used in trickle irrigation systems and various types of sprinklers used in sprinkle systems.

3.2. Schematics of lateral hydraulic computational elements

Figure 4 shows a schematic of a lateral with a series of emitters or riser-emitter ensemble distributed along its length. The spacing between emitters (the length of a lateral pipe segment) can be constant or variable and the individual emitters along the lateral can have the same or variable hydraulic characteristics. Each lateral pipe segment may have appurtenances, (such as valves, fittings, bends, and cross-sectional changes) arranged in series, that introduce local energy losses. Note that an important constraint on the application of the friction head loss equation to pipe segments between outlets, and also between appurtenances, is that the spacing between outlets as well as appurtenance must be sufficiently large for the flow within the pipe segment to be fully developed (Larock et al., 2000).

As noted in a preceding section, each lateral pipe segment and each emitter or riser-emitter ensemble represents a hydraulic link, the end points of which are labeled as nodes. It is assumed here that a lateral has at least one pipe segment and one emitter or riser-emitter ensemble. Hence, with such a configuration the number of links in a lateral, n_l , is an even integer

and is equally divided between the pipe segments and the emitters (Figure 4). The number of nodes in a lateral is then $n_l + 1$, with $n_l/2$ junction nodes (labeled here as n_j) and $n_l/2 + 1$ fixed head nodes, n_f . In a pipe network the number of junction nodes, n_j , fixed head nodes, n_f , links, n_l , and loops, n_L , are related by the network topological equation, Eq.10 (e.g., Wood and Rayes, 1981; Boulos and Altman, 1991):

$$n_l = n_j + n_f + n_L - 1 \quad (10)$$

Substituting the expressions for n_f and n_j in Eq. 10 and noting that n_L for a lateral is zero, it can be observed that Eq.10 is satisfied for the lateral configuration considered here (Figure 4).

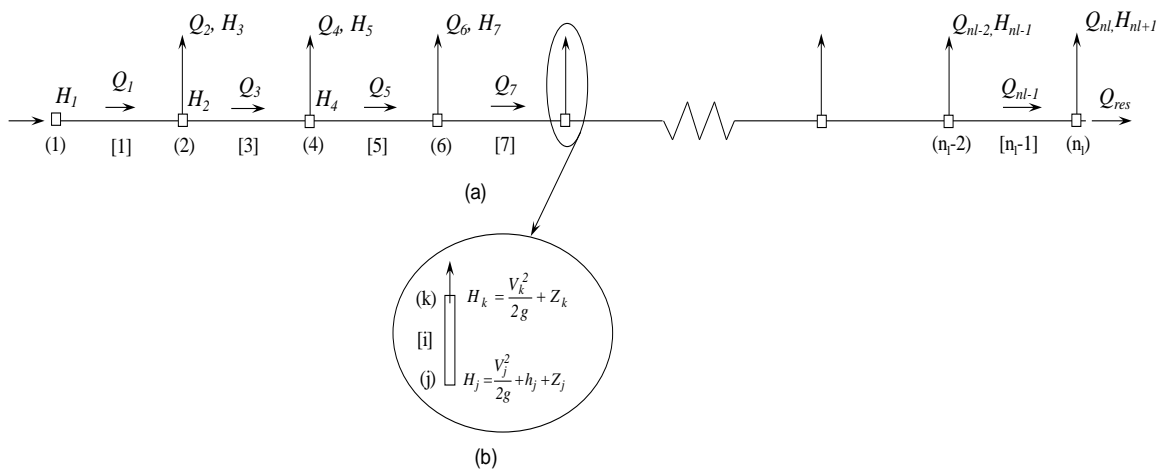


Figure 4 (a) Schematics of a lateral as a branched hydraulic network with n_l hydraulic links and $n_l + 1$ nodes and (b) Schematization of energy relations across an emitter or riser-emitter ensemble (Notations: (.) is node index and [.] is link index, H is total head [m], and V is velocity in the lateral segment just upstream of a junction node and the stream exit velocity at the emitter (m/s), note that discharges are subscripted with link indices and heads are subscripted with node indices)

3.3. Pipe network computational methods

In the simulation of a hydraulic network, operating under steady-state conditions, the modeling objective is to determine all the link discharges, Q , and nodal heads, H . A system of equations obtained through the application of the principles of conservation of mass and energy are used to formulate the simulation problem. These equations are nonlinear, because of the nonlinear dependence of head losses on discharge, and are solved iteratively. The most

commonly used technique, for solving these equations, is the Newton-Raphson method coupled with a suitable linear systems solver (e.g., Shamir and Howard, 1968; Epp and Fowler, 1970; Todini and Pilati, 1987; Boulos et al., 2006). One may discern four approaches for formulating the hydraulic network simulation problem (Boulos et al., 2006): (1) the loop method, (2) the node method, (3) the loop-node method, and (4) the pipe-node method. In subsequent paragraphs a concise description of each of these methods is presented, before that, however, we will define a few terms that are used in subsequent discussion. A *path*: is a series of links that connect two nodes in a hydraulic network. A *loop*: in the context of a pressurized hydraulic network analysis, a loop is a closed hydraulic circuit, it is a path that starts and ends at the same node. A *pseudo-loop*: is a path between two fixed head nodes of the network.

The loop method: With this method one energy conservation equation is written for each loop and pseudo-loop. The resultant system of equations is nonlinear in the link discharges, hence need to be solved iteratively. In each iteration, the energy equation for each loop is linearized about the current link discharges and is expressed in terms of the unknown incremental discharge, ΔQ . In addition continuity requirements need to be met at each node. The nodal continuity requirements remain satisfied through the iterative solution provided the solution starts with assumed discharges that meet the criteria at each of the nodes. In each iteration, the locally linearized loop energy equations can be assembled forming a system (with the same number of equations as unknowns) and are solved for the unknowns (the ΔQ vector) simultaneously (e.g., Epp and Fowler, 1970) or each linearized loop equation can be solved separately for the respective loop ΔQ 's (Cross, 1936). At the end of an iterative step, the discharge corrections are applied to the discharges in all the pipes in the respective loops (taking into account the direction of flow in each pipe relative to the path and noting that if a pipe is shared by two loops, the corrections from both loops need to be applied to that pipe). If the computed discharge corrections for all the loops are within a preset error tolerance, then the solution is obtained. If not, the iterative computation continues, until either a solution is obtained or a fixed number of maximum iterations is exceeded. Following a solution, the corresponding nodal heads can be calculated from the head discharge relationships, beginning at the point of known nodal head. An advantage of the loop method, compared to the other methods, is that it involves the least number of equations.

The node method: With the node method, a continuity equation is written for each junction node. Then using the link head discharge relationship each discharge going into or from a node is expressed in terms of the ratio of the difference between the respective nodal heads and the link hydraulic resistance coefficient. Note that this formulation combines the continuity and energy conservation equations (e.g., Shamir and Howard, 1968). The resultant nonlinear system with the same number of equations as unknowns can then be solved for the nodal heads iteratively with the Newton method. Once the nodal heads are determined, the link discharges can then be evaluated based on the link head discharge equations beginning at the point of known nodal head.

The node-loop method: In the node-loop method, the energy conservation equation is written for each loop and pseudo-loop in the network and the continuity equation is formulated for each junction node (Wood and Charles, 1972; Wood and Rayes, 1981). However, in contrast to the loop method, here the energy conservation and continuity equations are expressed in terms of the pipe discharges. The resultant nonlinear system with equal number of equations and unknowns can be solved with the linear theory method (Wood and Charles, 1972) or with the Newton-Raphson method (Boulos et al., 2006). Once the link discharges are computed, the nodal heads are calculated using the head-discharge relationships, beginning at the point of known nodal head.

The pipe-node method: the pipe-node method, commonly referred to as the gradient method, was proposed for application in pipe network analysis by Todini and Pilati (1987). The method writes one energy balance equation for each pipe and a continuity equation for each junction node. The resultant nonlinear system of equations has the same number of equations and unknowns (consisting of link discharges and nodal heads) that can be solved iteratively. Typically, the Newton iterative method, combined with a suitably selected linear system solver, is used to solve this system of equations (e.g., Todini and Pilati, 1987; Salgado et al., 1987; Boulos, 2006). Compared to other approaches, this formulation leads to a system with the largest number of equations. However, it is generally considered to be numerically as robust and efficient as the other methods or better (e.g., Salgado et al., 1987; Boulos et al., 2006). Todini and Pilati (1987) indicated that the gradient method (i.e., the pipe-node method) represents a more general formulation that guarantees a unique solution, compared to that of the loop method. Nielsen (1989) has shown that the node and loop methods are special cases of the pipe-node method.

Hence there is some ground to consider the pipe-node method as a more general representation of the hydraulic network simulation problem.

Among the four hydraulic network formulation approaches described above, the pipe-node method and the node method in principle can be directly applied to the lateral hydraulic (branched network) simulation problem considered here. In the study reported here, the pipe-node method, henceforth referred to as the gradient method (e.g., Todini and Pilati, 1987). is used to formulate and solve the lateral hydraulic simulation problem.

3.4. Problem fomulation with the gradient method

As noted in a preceding section, for a hydraulic simulation problem the modeling objective is to determine all the link discharges, Q , and the nodal (total) heads, H , of a lateral. It can be noted from Figure 4 that the hydraulics of a lateral, described here as a branched network, can be defined in terms of $2(n_l+1)$ discharges and nodal heads equally divided between Q and H . Evidently, a lateral has n_l link discharges, which are unknown, plus the residual discharge at the downstream end of the lateral, Q_{res} , which is given.

Furthermore, for a simulation problem, the head at the upstream end of the lateral is considered known and is used as the datum. In addition, as will be shown subsequently, the elevation of each emitter, which is known, can be treated as an imposed head on the emitter (e.g., Rossman, 2000, Estrada et al., 2009). Noting that there are $n_l/2$ emitters in a lateral (Figure 4), it then follows that the number of fixed head nodes, n_f , in a lateral can be given as $n_l/2+1$.

Considering that the residual outflow discharge, Q_{res} , as well is given, the total number of known heads and discharges become $n_l/2+2$. In which case, the number of system variables (unknowns) for a lateral is $3n_l/2$ link discharges and nodal heads. Out of these variables, the number of unknown nodal heads (located at the junction nodes) is $n_l/2$ and the number of unknown link discharges is n_l . Furthermore, it can be observed that for the branched network (lateral) configuration presented in Figure 4, n_l link head loss equations and $n_l/2$ junction continuity equations can be written, leading to a total of $3n_l/2$ equations. Recalling that n_l is an even integer, it follows that the product $3n_l/2$ is also integer. Hence, the resultant set of equations represents a coupled system with $3n_l/2$ equations and $3n_l/2$ unknowns with a possible unique solution.

3.4.1. Link energy balance

Energy equation, lateral pipe sections: Note that the following development assumes the flow direction indicated in Figure 4. Now consider a path connecting two consecutive nodes on a lateral, labeled here as nodes j and k , such that $j < k$. Further assume that the path proceeds from node j to node k , then the energy balance equation for the lateral segment linking these nodes can be expressed as

$$\left. \begin{aligned} & \left(\beta_i |Q_i|^{\xi_i-1} + \sum_p \pi_i^p |Q_i|^{\gamma-1} \right) Q_i = H_j - H_k \\ & \text{for } i = 1, 3, 5, \dots, n_l - 1, \\ & \quad j = 1, 2, 4, 6, \dots, n_l - 2, \quad k = 2, 4, 6, \dots, n_l \quad \text{and } j < k \end{aligned} \right\} \quad (11)$$

In Eq. 11, i is link index and j and k are indices of the upstream and downstream nodes of the i th pipe segment, respectively, and H_j and H_k are the total heads at the respective nodes (Figure 4). The first term in the parenthesis in Eq. 11 is related to friction head loss in the i th pipe segment and the parameters β_i and ξ_i are the hydraulic resistance coefficient and exponent of discharge in the friction head loss equation, respectively

$$\beta_i = k_1 \frac{f_i L_i}{D_i^5} \quad \text{and} \quad \xi_i = 2.0 \quad (12)$$

and the second term in parenthesis is related to the sum of local head losses that occur along the i th pipe segment. The parameters π_i^p and γ can be expressed as

$$\pi_i^p = k_3 \frac{k_{Li}^p}{D_i^4} \quad \text{and} \quad \gamma = 2.0 \quad (13)$$

where p is index of an appurtenance in a pipe segment, k_{Li}^p is the local head loss coefficient for the p th appurtenance in the i th pipe segment (-), and γ (-) is the exponent of discharge in the local head loss equation (Eq. 9). As will be explained shortly, local head losses considered here do not include those occurring at a junction node. Pipe appurtenances such as valves and fittings as well as changes in the orientation of the direction of pipe can be placed anywhere along the pipe segment. The exceptions are that the appurtenances cannot be placed at junction nodes and in the

current formulation reduction in pipe diameter is assumed to occur only at the upstream end of the lateral pipe segment. Furthermore, increases in pipe diameter cannot be handled by the model.

Note that in the simple branched network considered here, the flow directions are known. Furthermore, the paths assumed in problem formulation, Eq. 11, follow the same direction as those of the link flows, hence the algebraic sign of the discharges is always positive. Therefore, the use of absolute values in Eq. 11 is only meant to conform with accepted convention, in the formulation of the energy balance equation, for more general network problems, where flow directions in some of the links can be opposite to the path and the effect of the algebraic sign of the discharge on head loss and its derivative has to be taken into account implicitly as in the form given in Eq. 11 or explicitly as that used, for example, by Boulos et al (2006).

Energy equation, emitter or riser-emitter ensemble: In this section first the energy relations for the general case of a riser-emitter ensemble will be presented and the equation for the case in which emitters are placed directly on a lateral will then be shown to be a reduced form of that for a riser-emitter ensemble. Figure 5 depicts discharges into and from the lateral junction node along with components of specific energy and velocity at points immediately upstream and downstream of the junction node and at the boundary node (downstream end of the emitter).

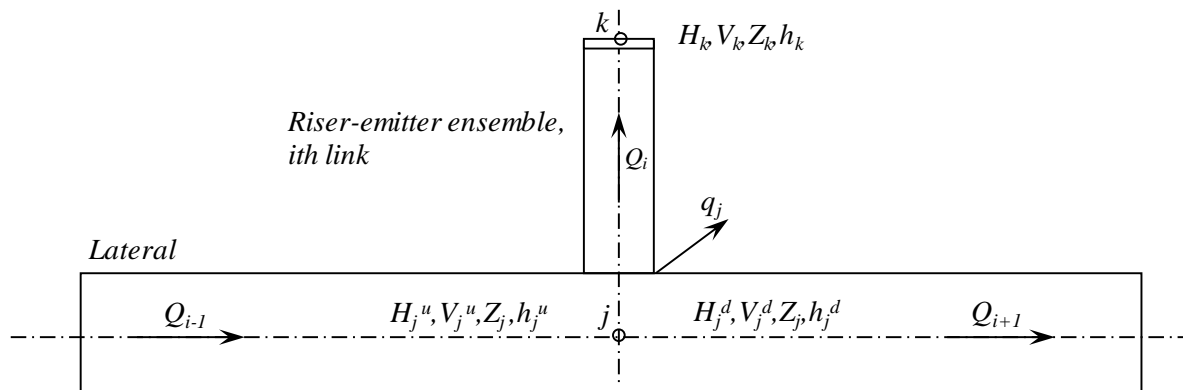


Figure 5. Junction node along a lateral with a riser-emitter ensemble (Notations: $[.]_j^u$, $[.]_j^d$, and $[.]_k$ are components of nodal specific energy and flow velocity at points immediately upstream and downstream of node j and at the boundary node k , respectively, and q_j is constant supply or demand at the junction node)

Note that the differentiation of the fluid specific energy at the junction node, j , into those at points immediately upstream and downstream of the node is a conceptual mechanism designed to acknowledge (for computational and presentation purposes) the existence of a discontinuity (i.e., two different levels) in the specific energy curve at a junction node, which stems from the fact that for practical computational purposes local head losses are assumed to occur at a point. Thus, it needs to be pointed out that these points are spatially coincident with the junction node at which they are presumed to occur (i.e., there is no horizontal distance and elevation difference between these points).

The energy equation for the i th riser-emitter ensemble along the path connecting a point immediately upstream of node j (point u in Figure 5) and node k is given as

$$\frac{(V_j^u)^2}{2g} + h_j^u + Z_j = \frac{(V_k)^2}{2g} + h_k + Z_k + h_{ei} + h_{fi} \quad (14)$$

where h_{ei} is head loss in the i th emitter, including exit loss, and h_{fi} is the friction head loss in the i th riser pipe. Note that the junction node local head loss associated with the branching flow is not considered in Eq. 14 and the reason for this will be explained shortly. Noting that the left hand side of Eq. 14 is equal to H_j^u and that the emitter discharges into the atmosphere, hence $h_k = 0$, Eq. 14 reduces to

$$\frac{(V_k)^2}{2g} + h_{ei} = (H_j^u - h_{fi}) - Z_k \quad (15)$$

Note that in Eq. 15, the expression $H_j^u - h_{fi}$ is the residual head just upstream of the emitter and Z_k is the elevation of the emitter. Thus Eq. 15 states that the head differential across the emitter is equal to the sum of the velocity head at the nozzle and emitter losses. The left-hand side of Eq. 15 is typically represented as a power function of the emitter discharge. The friction head loss through the riser pipe as well can be expressed as a function of emitter discharge, thus Eq. 15 can be given as

$$\left. \begin{aligned} & \left(\beta_i^l | Q_i |^{\xi_i^l - 1} + \beta_i | Q_i |^{\xi_i - 1} \right) Q_i = H_j^u - Z_k \\ & \text{for } i = 2, 4, 6, \dots, n_l \\ & \quad j = 2, 4, 6, \dots, n_l, \quad k = 3, 5, 7, \dots, n_l + 1 \text{ and } j < k \end{aligned} \right\} \quad (16)$$

The parameters β_i^l and ξ_i^l are coefficients and exponents of the emitter head-discharge function. For sprinklers, the nozzle head-discharge relationships are customarily expressed in terms of pressure heads. Hence, the use of such data to determine the parameters β_i^l and ξ_i^l implies a level of approximation.

If emitters are placed directly on the lateral, the energy equation, Eq. 16, reduces to

$$\beta_i^l | Q_i |^{\xi_i^l - 1} Q_i = H_j^u - Z_k \quad (17)$$

In summary, Eqs. 11 and 16 or Eq. 17 as the case may be, constitute the basic forms of the energy conservation equations applicable to pipe segments and riser-emitter ensemble, respectively. Note that the preceding problem formulation presumes that emission device with different hydraulic characteristics can be used along a lateral. It also assumes that diameters, lengths, spatial orientations, slopes, and resistance characteristics of pipe segments can vary along a lateral and that a couple of different pipe appurtenances can be fitted into any of the lateral pipe segments. However, a single set of pipe diameter, slope, and hydraulic resistance is used to characterize a lateral pipe segment.

A note on junction node head losses

As noted above, the model presented here does not take into account the local head losses at junction nodes. The reason is that consideration of the junction node local head losses leads to forms of energy equations that are not readily solvable within the framework of the gradient method. The head loss equations for each riser-emitter ensemble, Eq. 16, eventually need to be coupled with the head loss equations for pipe segments, Eq. 11, to form a system that describes the hydraulics of the entire lateral. For the resultant system of equations to be readily solvable, the nodal head H_k in Eq. 11 and H_j^u in Eq. 16 should refer to the same total head. Furthermore, the energy equation for each link needs to be a function of a single discharge, if it is to produce a

consistent system, when coupled with the continuity equations. However, that will not be necessarily the case, if the junction node local head losses are taken into account.

At the j th junction node, the local head loss associated with the through-flow can be taken into account in two ways. It can be included in the energy equation written for the lateral pipe segment immediately upstream of the node. Alternatively it can be incorporated into the energy equation for the pipe segment immediately downstream of the node. If the first option is adopted, then H_k in Eq. 11 is equal to H_j^d and not H_j^u (Figure 5). In which case, in order to make Eq. 16 consistent with Eq. 11, the sum of H_j^d and the junction local head loss associated with the through-flow needs to be substituted for H_j^u in Eq. 16 (i.e., Eq. 16 need to be expressed in terms of H_j^d). However, with such a formulation it can readily be shown that the resultant riser-emitter ensemble energy equation becomes a function of two discharges, the discharge in the i th riser-emitter ensemble and the discharge in the pipe segment immediately upstream of the junction node. The implication is that the resultant system of equations has a structure that is not readily solvable within the framework of the gradient method.

Alternatively, if the junction head loss associated with the through-flow is included in the energy equation of the pipe segment immediately downstream of the node, then H_k in Eq. 11 and H_j^u in Eq. 16 would refer to the same total head and Eqs. 11 and 16 become consistent. However, the resultant equation for the downstream pipe segment would become a function of two discharges, the discharge in it and in the lateral pipe segment immediately upstream of it. Thus, the problem of solvability will crop up again.

A simplification implemented in the current model is to assume that the junction node local head losses both for the branching- and through-flow are negligible. Observe that once the junction loss associated with the branching-flow is neglected, the energy equation for a riser-emitter ensemble can be expressed in the form given in Eqs. 16 or Eq. 17. Thus Eqs. 11 and 16 or 17 represent the link energy balance equations for a lateral pipe segment and a riser-emitter ensemble, respectively. Note that the fact that the through-flow loss is not included in Eq. 11 implies that H_k is equal to H_j^u which in turn is equal to H_j^d .

3.4.2. Continuity at junction nodes

The principle of mass conservation, when applied to a junction node (e.g., Figure 5), requires that the sum of flows into a junction minus the sum of flows leaving a junction should be equal to the constant supply or demand at the junction node:

$$\sum_{i \in I} Q_i - \sum_{i \in L} Q_i \pm q_j = 0 \quad (18)$$

where Q_i is the discharge in the i th link that carries flow into or from the j th junction node, I is the set of pipes that carry discharge into node j , and L is the set of pipes that carry discharge leaving node j , and q_j is constant supply or demand at node j , which is generally zero for an irrigation lateral. Note that q_j is subtracted from the net nodal inflow if it represents demand is added to the net nodal inflow if it represents supply.

3.4.3. System of Equations

A more general form of the continuity equation applicable to the network problem can be expressed in a form analogous to that given by Nielsen (1989)

$$\sum_{i=1}^{n_l} (\zeta_{ij} Q_i) \pm q_j = 0, \quad \text{for } j = 2, 4, \dots, n_l \quad (19)$$

In Eq. 19, ζ_{ij} is the network connectivity coefficient and is given as

$$\zeta_{ij} = \begin{cases} +1, & \text{if link } i \text{ is connected to node } j \text{ and flow is into node } j \\ -1, & \text{if link } i \text{ is connected to node } j \text{ and flow is from node } j \\ 0, & \text{if link } i \text{ is not connected to node } j \end{cases} \quad (20)$$

For simplicity, let the expression in parenthesis in Eqs. 11 and 16 be labeled as θ_i , in which case the energy equation for the i th link can be expressed in a form analogous to Eq. 19

$$\sum_{q=1}^{n_l} (\tau_q \theta_i Q_i) + \sum_{j=1}^{n_l+1} (\alpha_{ij} H_j) = 0 \quad \text{for } i = 1, 2, \dots, n_l \quad (21)$$

In Eq. 21, τ_q is a coefficient defined as

$$\tau_q = \begin{cases} +1, & \text{if the link index } i = q \\ 0, & \text{if the link index } i \neq q \end{cases} \quad (22)$$

where q is an index of the coefficient τ and α_{ij} is the network connectivity coefficient defined in accordance with Eq. 20. Application of Eq. 21 to all links (pipe segments and emitters) results in n_l nonlinear equations. Applying the continuity equation, Eq. 19, to all the junction nodes results in $n_l/2$ linear equations. The nonlinear energy balance equations and the linear continuity equations can then be coupled resulting in the system of equations, summarized in Table 1. Note that the total heads in the link energy balance equations (the upper half of Table 1) are arranged into two separate blocks for convenience: unknown nodal heads, H 's, and known nodal heads, H_0 's. Furthermore, by comparing Eqs. 16 and 21 it can be noted that in Table 1 the known nodal head of an emitter is equal to its elevation.

Now, let the terms in the system of equations presented in Table 1 be partitioned into blocks as shown in Table 2 (i.e., horizontally divided into blocks of energy balance and continuity equations and vertically into terms that are functions of discharge and head). The vector representation of the corresponding system is

$$\left. \begin{array}{l} \Psi_{1l}Q + \Psi h = 0 \\ \Psi_{2l}Q + 0 = q \end{array} \right\} \quad (23)$$

In Eq. 23

$$\Psi_{1l} = \text{diag} \{ \theta_1, \theta_2, \theta_3, \dots, \theta_{nl-1}, \theta_{nl} \} \quad (24)$$

$$Q^T = \{ Q_1, Q_2, Q_3, \dots, Q_{nl-1}, Q_{nl} \} \quad (25)$$

$$h^T = \{ H_2, H_4, H_6, \dots, H_{nl}, H_{01}, H_{03}, \dots, H_{0nl-1}, H_{0nl+1} \} \quad (26)$$

and Ψ is an $n_l \times (n_l + 1)$ and Ψ_{2l} is an $n_l/2 \times n_l$ topological incidence matrices and q is a vector of constant nodal inflows or outflows with $n_l/2$ elements. Note that for a typical irrigation lateral, the elements of the q vector are zero except for the residual outflow.

Table 2. A system of equations describing flow in a lateral with n_l links and n_l+1 nodes, partitioned for block matrix representation as shown in Eq. 23

$\theta_1 Q_1 + 0 +$	$+ 0 + H_2 + 0 +$	$- H_{0l} + 0 +$	$= 0$
$0 + \theta_2 Q_2 + 0 +$	$+ 0 - H_2 + 0 +$	$+ 0 + H_{03} +$	$= 0$
$. + 0 + \theta_3 Q_3 + 0 +$	$+ 0 - H_2 + H_4 + 0 +$	$. + 0 + 0 +$	$= 0$
$. + . + 0 + \theta_4 Q_4 + 0 +$	$+ 0 + 0 - H_4 + 0 +$	$. H_{05} +$	$= 0$
$. + . + . + 0 + \theta_5 Q_5 + 0 +$	$+ 0 + 0 - H_4 + H_6 + 0 +$	$. 0 +$	$= 0$
$. + 0 + 0 +$	$. + 0 + 0$	$.$	$= 0$
$. +$	$.$	$. 0 +$	$= 0$
$. + + 0 +$	$.$	$. + H_{0n-1} + 0 = 0$	$= 0$
$. + 0 + \theta_{n-1} Q_{n-1} + 0 +$	$. + 0 - H_{n-2} + H_n +$	$. + 0 + 0 = 0$	$= 0$
$0 + 0 + 0 + + 0 + \theta_n Q_n + 0 + 0 +$	$. + . + 0 - H_n +$	$. + 0 + H_{0n+1} = 0$	$= 0$
$Q_1 - Q_2 - Q_3 + 0 + 0 + 0$	$. + 0 +$	$. + 0 + 0 = 0$	$= 0$
$0 + 0 + Q_3 - Q_4 - Q_5 +$	$.$	$.$	$= 0$
$. + . + 0 + 0 + Q_5 - . . . + 0 +$	$.$	$.$	$= 0$
$. + 0 +$	$.$	$.$	$= 0$
$. +$	$.$	$.$	$= 0$
$. + Q_{n-2} - Q_{n-1} + 0 +$	$.$	$. + 0 = 0$	$= 0$
$0 + + Q_{n-1} - Q_n + 0$	$.$	$. 0 + 0 = q_n$	$= q_n$

Matrices Ψ and Ψ_{21} define the hydraulic network connectivity configuration relative to flow direction and are often referred to as the network topological incidence matrices (e.g., Boulos and Altman, 1991). In this document, however, we will use the more practical phrase, network connectivity matrices (e.g., Boulos et al., 2006), to refer to these matrices. These matrices describe which node in the network is connected to which other node or nodes, by which link or links, and what the flow direction is in each of the links. The elements of matrices Ψ and Ψ_{21} are defined in accordance with Eq. 20, hence they take values of -1 , 0 , or $+1$ only. The exact form of matrix Ψ is shown in Table 3. Note that parts I and II of matrix Ψ represent elements of the network with unknown and known nodal heads, respectively. Furthermore, the form of matrix Ψ_{21} can be readily deduced by comparing Eqs. 19, 23 and Table 2 and is given in Table 4.

Table 3. Hydraulic network topological incidence matrix (network connectivity matrix), Ψ

		Node indices, j																		
		2	4	6	8	10	.	.	.	n_1		1	3	5	7	9	.	.	.	n_{l+1}
Link indices, i	1	1								0		-1	0	.						0
	2	-1	0							.		0	1	0	.					.
	3	-1	1							.		.	0	0	.					.
	4	0	-1	0						.		.	.	1						.
	5	.	-1	1						.		.	.	0						.
	.	.	0	-1					

						0		0	.	.						.
						-1		1	.	.						0
	n_l	0	.	.						0		-1	0			1

I (nodes with unknown heads)
II (nodes with known heads)

Note that a close look at Eqs. 19 and 21 and Tables 1 and 2 shows that the elements of the network connectivity matrices are coefficients of the terms in the energy balance and continuity equations, hence they are direct results of the physical description of steady flow in a pipe network. In general, an important computational utility of these matrices is that they automatically keep track of changes in flow direction during numerical solutions. However, it is

important to note that for the simple branched network considered here (Figure 4), the flow directions are known. Hence, once these matrices are initialized at the start of the numerical solution, they need not be updated during the computation.

Table 4. Hydraulic network connectivity matrix, Ψ_{21}

		Link indices, i										
		1	2	3	4	5	.	.	.	n_l		
Node indices, j	2	1	-1	-1	0	0		
	4	0	0	1	-1	-1	0	.	.	.		
	6				0	1	-1	.	.	.		
		-1	-1	0
n_l	0	0	1	-1

Now, if the terms of the energy equations with given total heads (Table 2) are moved to the right hand side as shown in Table 5, the resultant system is

$$\left. \begin{aligned} \Psi_{11}\mathbf{Q} + \Psi_{12}\mathbf{H} &= -\Psi_{10}\mathbf{H}_0 \\ \Psi_{21}\mathbf{Q} + \mathbf{0} &= \mathbf{q} \end{aligned} \right\} \quad (27)$$

Note that in Eq. 27 the Ψ_{12} and Ψ_{10} matrices are obtained by partitioning matrix Ψ into blocks representing elements of the network with known and unknown heads, respectively. Ψ_{12} is an $n_l \times n_l/2$ and Ψ_{10} is an $n_l \times (n_l/2 + 1)$ matrices and are shown as parts I and II of matrix Ψ (Table 3), respectively. Furthermore, comparing matrix Ψ_{12} (Part I of Table 3) and Ψ_{21} (Table 4) shows that $\Psi_{12} = \Psi_{21}^T$.

In addition, it can be observed that the \mathbf{H} and \mathbf{H}_0 vectors in Eq. 27 are obtained by partitioning the \mathbf{h} vector, Eq. 26, into the unknown and known head vectors, respectively:

$$\mathbf{H}^T = \{H_2, H_4, \dots, H_{n_l}\} \quad \text{and} \quad \mathbf{H}_0^T = \{H_{01}, H_{03}, \dots, H_{0n_l+1}\} \quad (28)$$

Table 5. A system of equations describing flow in a lateral with n_l links and n_l+1 nodes, partitioned for block matrix representation as shown in Eq. 27

$\theta_1 Q_1 + 0 + \dots$	+	$0 + H_2 + 0 + \dots$	=	$+ H_{01} + 0 + \dots$
$0 + \theta_2 Q_2 + 0 + \dots$	+	$0 - H_2 + 0 + \dots$	=	$0 - H_{03} + \dots$
$\dots + 0 + \theta_3 Q_3 + 0 + \dots$	+	$0 - H_2 + H_4 + 0 + \dots$	=	$\dots + 0 + 0 + \dots$
$\dots + \dots + 0 + \theta_4 Q_4 + 0 + \dots$	+	$0 + 0 - H_4 + 0 + \dots$	=	$\dots - H_{05} + \dots$
$\dots + \dots + \dots + 0 + \theta_5 Q_5 + 0 + \dots$	+	$0 + 0 - H_4 + H_6 + 0 + \dots$	=	$\dots 0 + \dots$
$\dots + \dots + \dots 0 + 0 + \dots$	+	$\dots + 0 + 0 + \dots$	=	$\dots + \dots + \dots$
$\dots + \dots + \dots + \dots + \dots$	+	$\dots + \dots + \dots + \dots$	=	$\dots + \dots + \dots$
$\dots + \dots + \dots + \dots + 0 + \dots$	+	$\dots + 0 + \dots$	=	$\dots - H_{0n-1} + 0$
$\dots + \dots + \dots + \dots + 0 + \theta_{n-1} Q_{n-1} + 0 + \dots$	+	$\dots + 0 - H_{n-2} + H_{n-1} = \dots$	=	$\dots + 0 + 0$
$0 + 0 + 0 + \dots + 0 + \theta_n Q_n + 0 + 0 + \dots$	+	$\dots + \dots + 0 - H_{n-1} = \dots$	=	$\dots + 0 - H_{0n+1}$
$Q_1 - Q_2 - Q_3 + 0 + 0 + \dots + 0 + \dots$	+	$\dots + 0 + \dots$	=	0
$0 + 0 + Q_3 - Q_4 - Q_5 + \dots + \dots + \dots$	+	$\dots + \dots$	=	0
$\dots + \dots + 0 + 0 + Q_5 - \dots + \dots + 0 + \dots$	+	$\dots + \dots$	=	0
$\dots + \dots + \dots 0 + \dots + \dots + \dots$	+	$\dots + \dots$	=	0
$\dots + \dots + \dots + \dots + \dots + \dots + \dots$	+	$\dots + \dots$	=	0
$\dots + \dots + \dots + \dots + \dots + \dots + Q_{n-2} - Q_{n-1} + 0 + \dots$	+	$\dots + \dots + \dots + \dots$	=	0
$0 + \dots + \dots + \dots + \dots + \dots + Q_{n-1} - Q_n + 0 + \dots$	+	$\dots + \dots + \dots + \dots$	=	q_n

The system in Eq. 27, with $3n/2$ equations and $3n/2$ unknowns (Table 5 and Eqs. 25 and 28), can be expressed in terms of block matrices as

$$\begin{pmatrix} \Psi_{11} & \Psi_{12} \\ \Psi_{21} & \mathbf{0} \end{pmatrix} \begin{pmatrix} Q \\ H \end{pmatrix} = \begin{pmatrix} -\Psi_{10}H_0 \\ q \end{pmatrix} \quad (29)$$

Details regarding the form of the triangular block matrix, the individual blocks, and the vectors in Eq. 29 are given in Table 6. Advantages of partitioning the matrix and vectors into blocks are: (i) As will be shown subsequently, the Ψ_{22} matrix, which is zero, does not add to the computational overhead and (ii) For simple branched networks, such as irrigation laterals, the network connectivity matrices Ψ_{10} , Ψ_{12} , and Ψ_{21} are constants and once initialized they need not be updated during subsequent computation, thus differentiation of these matrices from the Ψ_{11} matrix provides a more convenient way of handling them, which contributes to a more efficient numerical solution.

4. Lateral hydraulics, simulation: Numerical solution with the gradient method

4.1. Iterative solution

In order to develop the iterative solution, Eq. 27 will be recast in the following form

$$\left. \begin{aligned} \Psi_{11}Q + \Psi_{12}H + \Psi_{10}H_0 &= \mathbf{0} \\ \Psi_{21}Q - q &= \mathbf{0} \end{aligned} \right\} \quad (30)$$

The form of the corresponding system of equations is presented in Table 7. The system in Eq. 30 is nonlinear and needs to be solved iteratively. The most commonly used technique for solving Eq. 30 is the Newton-Raphson method. With this method, in each iteration, a linear system of equations (which represent the first-order Taylor series approximation of the solution about the current iterates) are solved with an appropriate linear systems solver. In vector form, this system of equations is given as:

$$\theta^m \delta x^{m+1} = -F^m \quad (31)$$

where m is iteration index, θ^m is the Jacobian matrix of the system, evaluated at the m th estimate of the variable vector, \mathbf{x} ; and $\delta\mathbf{x}^{m+1}$ is the vector of incremental changes in the variables at the $(m+1)$ th iteration. Noting that each iteration produces a variable vector that only approximates the solution, substituting the m th estimate of the variables in Eq. 30 yields \mathbf{F}^m , which is a vector of the residuals of energy balance and continuity. Considering the system of equations presented in Table 7, it can be noted that in Eq. 31

$$\theta^m = \begin{pmatrix} (\nabla F_{e1}^m)^T \\ (\nabla F_{e2}^m)^T \\ \cdot \\ \cdot \\ \cdot \\ (\nabla F_{enl}^m)^T \\ (\nabla F_{c2}^m)^T \\ (\nabla F_{c4}^m)^T \\ \cdot \\ \cdot \\ \cdot \\ (\nabla F_{cn_i}^m)^T \end{pmatrix}, \quad \delta\mathbf{x}^{m+1} = \begin{pmatrix} \delta Q_1^{m+1} \\ \delta Q_2^{m+1} \\ \cdot \\ \cdot \\ \cdot \\ \delta Q_{nl}^{m+1} \\ \delta H_2^{m+1} \\ \delta H_4^{m+1} \\ \cdot \\ \cdot \\ \cdot \\ \delta H_{nl}^{m+1} \end{pmatrix}, \quad \text{and} \quad \mathbf{F}^m = \begin{pmatrix} F_{e1}^m \\ F_{e2}^m \\ \cdot \\ \cdot \\ \cdot \\ F_{enl}^m \\ F_{c2}^m \\ F_{c4}^m \\ \cdot \\ \cdot \\ \cdot \\ F_{cnl}^m \end{pmatrix} \quad (32)$$

In Eq. 32, $(\nabla F_{ei}^m)^T$ is the transpose of the gradient vector of the energy balance equation, for the i th link, evaluated based on the m th estimate of the variables; $(\nabla F_{cj}^m)^T$ is the transpose of the gradient vector of the continuity equation, for the j th junction node, (note that these vectors are constants and will be discussed subsequently); δQ_i^{m+1} is the incremental change in the discharge in the i th link at the $(m+1)$ th iteration; δH_j^{m+1} is the incremental change in the unknown head at the j th node and at the $(m+1)$ th iteration; F_{ei}^m is the residual of the i th energy balance equation evaluated based on the m th estimate of the variables; and F_{cj}^m is the residual of the continuity equation, at the j th junction node, evaluated based on the m th estimate of the variables.

Table 7. A system of nonlinear equations describing flow in a lateral with n_l links and n_l+1 nodes, partitioned for block matrix representation as shown in Eq. 30

$$\begin{array}{l}
 F_{d1} = \theta_1 Q_1 + 0 + \dots + 0 + H_2 + 0 + \dots - H_{01} + 0 + \dots = 0 \\
 F_{d2} = 0 + \theta_2 Q_2 + 0 + \dots + 0 - H_2 + 0 + \dots + 0 + H_{02} + \dots = 0 \\
 F_{d3} = \dots + 0 + \theta_3 Q_3 + 0 + \dots + 0 - H_2 + H_4 + 0 + \dots + 0 + 0 + \dots = 0 \\
 F_{d4} = \dots + \dots + 0 + \theta_4 Q_4 + 0 + \dots + 0 + 0 - H_4 + 0 + \dots + H_{05} + \dots = 0 \\
 F_{d5} = \dots + \dots + \dots + 0 + \theta_5 Q_5 + 0 + \dots + 0 + 0 - H_4 + H_6 + 0 + \dots + 0 + \dots = 0 \\
 \dots + \dots + \dots + 0 + 0 + \dots + \dots + 0 + 0 + \dots + \dots + \dots = 0 \\
 \dots + \dots = 0 \\
 \dots + 0 + \dots = 0 \\
 \dots + \dots + \dots + \dots + \dots + \dots + 0 + \dots + H_{0n-1} + 0 = 0 \\
 \dots + \dots + \dots + \dots + \dots + \dots + 0 + \theta_{n,l} Q_{n,l} + 0 + \dots + 0 - H_{n-2} + H_{n,l} + \dots + 0 + 0 = 0 \\
 F_{enl} = 0 + 0 + 0 + \dots + \dots + \dots + 0 + \theta_{n,l} Q_{n,l} + 0 + 0 + \dots + 0 - H_{n,l} + \dots + 0 + H_{0n+1} = 0 \\
 \hline
 F_{c2} = Q_1 - Q_2 - Q_3 + 0 + 0 + \dots + 0 + \dots + \dots + 0 = 0 \\
 F_{c4} = 0 + 0 + Q_3 - Q_4 - Q_5 + \dots + \dots + \dots + \dots = 0 \\
 F_{c6} = \dots + \dots + 0 + 0 + Q_5 - \dots + \dots + 0 + \dots = 0 \\
 \dots + \dots + \dots + 0 + \dots + \dots + \dots + \dots = 0 \\
 \dots + \dots = 0 \\
 \dots + \dots = 0 \\
 \dots + \dots + \dots + \dots + \dots + \dots + Q_{n-2} - Q_{n-1} + 0 + \dots + \dots + \dots + \dots + 0 = 0 \\
 F_{cnl} = 0 + \dots + \dots + \dots + \dots + \dots + Q_{n-1} - Q_{nl} + 0 + \dots + \dots + \dots + \dots + 0 - q_{nl} = 0
 \end{array}$$

F_{ei} = the i th link energy balance equation and F_{cj} = is the j th junction node continuity equation

If the Jacobian matrix, the variable vector, and the vector of residuals (Eq. 32) are partitioned as shown in Table 8, then the system in Eqs. 31 can be expressed in terms of block matrices as

$$\begin{pmatrix} (\Psi'_{11})^m & \Psi_{12} \\ \Psi_{21} & \mathbf{0} \end{pmatrix} \begin{pmatrix} \delta Q^{m+1} \\ \delta H^{m+1} \end{pmatrix} = - \begin{pmatrix} F_e^m \\ F_c^m \end{pmatrix} \quad (33)$$

Comparing Eqs. 31 and 33, it can be observed that

$$\theta^m = \begin{pmatrix} (\Psi'_{11})^m & \Psi_{12} \\ \Psi_{21} & \mathbf{0} \end{pmatrix}, \quad \delta x^{m+1} = \begin{pmatrix} \delta Q^{m+1} \\ \delta H^{m+1} \end{pmatrix}, \quad \text{and} \quad F^m = \begin{pmatrix} F_e^m \\ F_c^m \end{pmatrix} \quad (34)$$

As noted in the preceding section, each row of the Jacobian matrix represents the transpose of the gradient vector of the *i*th link energy balance or the *j*th nodal continuity equations. It can then be readily observed that the rows of each of the $(\Psi'_{11})^m$, Ψ_{12} , and Ψ_{21} matrices, in Eq. 34, are subsets of their respective gradient vectors (Table 8). In Eqs. 33 and 34, $(\Psi'_{11})^m$ is the Ψ'_{11} matrix (which is a diagonal matrix) evaluated based on Q^m . Exact mathematical expressions for the derivatives of the link energy balance equations with respect to the link discharges (i.e., diagonal elements of Ψ'_{11} matrix) are presented in section 4.2.5.

Although matrices Ψ_{12} and Ψ_{21} appear in both equations 29 and 33 (see also Tables 6 and 8), it needs to be pointed out that these matrices are related to different systems of equations when used in Eqs. 29 and 33. In the context of Eq. 29, they are related to the system comprised of the energy balance and continuity equations and are derived in accordance with Eq. 20. In Eq. 33 they are subsets of the gradient vectors of the energy balance and continuity equations, hence obtained through differentiation of the conservation equations.

We will now derive an expression for the variables, Q and H , at the $(m+1)$ th iteration. The derivation presented subsequently is broadly patterned after the work of Todini and Pilati (1987).

Based on Eq. 33 and 34, the incremental change in the variable vector at the $(m+1)$ th iteration can be expressed as

$$\begin{pmatrix} \delta Q^{m+1} \\ \delta H^{m+1} \end{pmatrix} = -(\theta^m)^{-1} \begin{pmatrix} F_e^m \\ F_c^m \end{pmatrix} \quad (35)$$

Table 8. Matrix representation of the linear system of equations solved during each Newton iteration, Eq. 33

$(\Psi_{11})^m$											Ψ_{12}			δQ		F_e					
$F_e'Q_1 _{Q_1^m}$	0	0	1	0	.	.	.	δQ_1	=	F_{e1}			
0	$F_e'Q_2 _{Q_2^m}$	0	0	-1	0	.	.	.	δQ_2	=	F_{e2}			
.	0	$F_e'Q_3 _{Q_3^m}$	0	0	-1	1	0	.	.	δQ_3	=	F_{e3}			
.	.	0	$F_e'Q_4 _{Q_4^m}$	0	0	0	-1	0	.	.		=	.			
.	.	.	0	$F_e'Q_5 _{Q_5^m}$	0	0	0	-1	1	0	.		=	.			
.	.	.	.	0	0	0	-1	0	.		=	.			
.		=	.			
.		=	.			
.	0		=	.			
.	0	$F_e'Q_{nl-1} _{Q_{nl-1}^m}$	0	δQ_{nl-1}	=	F_{ent-1}			
.	0	$F_e'Q_{nl} _{Q_{nl}^m}$	0	0	-1	1	δQ_{nl}	=	F_{ent}
0	0	0	0	0	.	.	0	-1	.	δH_2	=	F_{c2}
1	-1	-1	0	0	δH_4	=	F_{c4}
0	0	1	-1	-1	δH_6	=	.
.	.	0	0	1	=	.
.	.	.	.	0	=	.
.	=	.
.	=	.
.	=	.
.	=	.
.	=	.
0	1	-1	-1	0	δH_{nl-2}	=	F_{ent-2}
0	1	-1	0	δH_{nl}	=	F_{ent}
												0	0	δH	=	F_c

1. The blocks Ψ_{11}' , Ψ_{12} , Ψ_{21} , and the zero matrix in Table 8 constitute the Jacobian matrix, θ , Eqs. 31 and 32;
2. Each row of the Jacobian matrix is the transpose of the gradient vector of the i th link energy balance or the j th nodal continuity equation; the gradient vectors of the link energy balance equations are evaluated based on the m th approximation of the discharge vector, Q^m ; The gradient vectors of the nodal continuity equations are constants that, in the current application, remain unaltered once they are set in the first iteration;
3. $F_e'Q_i|_{Q_i^m}$ is the derivative of the i th link energy balance equation with respect to the i th link discharge, evaluated based on the m th estimate of the i th link discharge;
4. $(\Psi_{11}')^m$ is a diagonal matrix and each of its rows are obtained by truncating the transpose of the gradient vector of the respective link energy balance equations at the vertical dashed line;
5. Each row of matrix Ψ_{12} is a subset of the transpose of the gradient vector of the respective link energy balance equations (i.e., each entry represents the derivative of the link energy balance equation with respect to an unknown nodal head);
6. Each row of matrix Ψ_{21} is obtained by truncating the transpose of the gradient vector of the corresponding nodal continuity equation at the vertical dashed line (i.e., each entry represents the derivative of the continuity equation with respect to a link discharge);
7. δQ is the vector of incremental changes in link discharges;
8. δH is the vector of incremental changes in unknown nodal heads;
9. F_e is the vector of residuals of the link energy balance equations evaluated based on the m th approximation of the variables;
10. F_c is the vector of residuals of the junction continuity equations evaluated based on the m th approximation of the link discharge;

For convenience we label the inverse of the Jacobian as $\boldsymbol{\beta}$ (i.e., $\boldsymbol{\beta} = \left(\boldsymbol{\theta}^m\right)^{-1}$), where

$$\boldsymbol{\beta} = \begin{pmatrix} \boldsymbol{\beta}_{11} & \boldsymbol{\beta}_{12} \\ \boldsymbol{\beta}_{21} & \boldsymbol{\beta}_{22} \end{pmatrix} \quad (36)$$

Substituting Eq. 36 in Eq. 35 and expanding yields an expression for the incremental changes in the system variables, $\delta\mathbf{Q}$ and $\delta\mathbf{H}$, at the $(m+1)$ th iteration in terms of the elements of the inverse of the Jacobian matrix

$$\delta\mathbf{Q}^{m+1} = -\boldsymbol{\beta}_{11}\mathbf{F}_e^m - \boldsymbol{\beta}_{12}\mathbf{F}_c^m \quad (37)$$

$$\delta\mathbf{H}^{m+1} = -\boldsymbol{\beta}_{21}\mathbf{F}_e^m - \boldsymbol{\beta}_{22}\mathbf{F}_c^m \quad (38)$$

Expressions can be obtained for the elements of the $\boldsymbol{\beta}$ matrix in terms of the elements of the Jacobian matrix.

$$\boldsymbol{\beta}_{11} = \boldsymbol{\alpha}^m - \boldsymbol{\alpha}^m\boldsymbol{\Psi}_{12}(\boldsymbol{\Psi}_{21}\boldsymbol{\alpha}^m\boldsymbol{\Psi}_{12})^{-1}\boldsymbol{\Psi}_{21}\boldsymbol{\alpha}^m \quad (39)$$

$$\boldsymbol{\beta}_{12} = \boldsymbol{\alpha}^m\boldsymbol{\Psi}_{12}(\boldsymbol{\Psi}_{21}\boldsymbol{\alpha}^m\boldsymbol{\Psi}_{12})^{-1} \quad (40)$$

$$\boldsymbol{\beta}_{21} = (\boldsymbol{\Psi}_{21}\boldsymbol{\alpha}^m\boldsymbol{\Psi}_{12})^{-1}\boldsymbol{\Psi}_{21}\boldsymbol{\alpha}^m \quad (41)$$

$$\boldsymbol{\beta}_{22} = -(\boldsymbol{\Psi}_{21}\boldsymbol{\alpha}^m\boldsymbol{\Psi}_{12})^{-1} \quad (42)$$

where

$$\boldsymbol{\alpha}^m = \left[\left(\boldsymbol{\Psi}'_{11} \right)^m \right]^{-1} \quad (43)$$

and the expression $\left[\left(\boldsymbol{\Psi}'_{11} \right)^m \right]^{-1}$ is the inverse of matrix $\boldsymbol{\Psi}'_{11}$ evaluated based on the m th

approximation of the link discharge vector. The details of the derivation of Eqs. 39-42 is presented in Appendix I.

Based on Eq. 30, the expressions for the residuals of the link energy balance and nodal continuity equations, evaluated in terms of the m th estimate of the variable vector, can be given as

$$\Psi_{11}^m \mathbf{Q}^m + \Psi_{12} \mathbf{H}^m + \Psi_{10} \mathbf{H}_0 = \mathbf{F}_e^m \quad (44)$$

$$\Psi_{21} \mathbf{Q}^m - \mathbf{q} = \mathbf{F}_c^m \quad (45)$$

In Eq. 44, Ψ_{11}^m is matrix Ψ_{11} (i.e., the diagonal matrix given in Eq. 24) evaluated based on the m th estimate of the discharge vector, \mathbf{Q}^m , and \mathbf{H}^m is estimate of the junction nodal head vector at the m th iteration. Note that matrix operations involving Eq. 45 conveniently exclude the zero matrix, Ψ_{22} , which may contribute to efficient numerical solution.

Eqs. 37-42, 44, and 45 can be used to obtain expressions for the revised estimates of the variables in the current iteration, \mathbf{Q}^{m+1} and \mathbf{H}^{m+1} .

Expression for \mathbf{H}^{m+1} : Substituting Eqs. 41, 42, 44, and 45 in Eq. 38 yields

$$\begin{aligned} \delta \mathbf{H}^{m+1} = & -\left(\Psi_{21} \alpha^m \Psi_{12}\right)^{-1} \Psi_{21} \alpha^m \left(\Psi_{11}^m \mathbf{Q}^m + \Psi_{12} \mathbf{H}^m + \Psi_{10} \mathbf{H}_0\right) \\ & + \left(\Psi_{21} \alpha^m \Psi_{12}\right)^{-1} \left(\Psi_{21} \mathbf{Q}^m - \mathbf{q}\right) \end{aligned} \quad (46)$$

Rearranging terms, Eq. 46 can be written as

$$\begin{aligned} \delta \mathbf{H}^{m+1} = & -\left(\Psi_{21} \alpha^m \Psi_{12}\right)^{-1} \left(\Psi_{21} \alpha^m \Psi_{12}\right) \mathbf{H}^m - \left(\Psi_{21} \alpha^m \Psi_{12}\right)^{-1} \left(\Psi_{21} \alpha^m \right. \\ & \left. \left(\Psi_{11}^m \mathbf{Q}^m + \Psi_{10} \mathbf{H}_0\right) + \left(\mathbf{q} - \Psi_{21} \mathbf{Q}^m\right)\right) \end{aligned} \quad (47)$$

which is equivalent to

$$\delta \mathbf{H}^{m+1} = -\mathbf{H}^m - \left(\Psi_{21} \alpha^m \Psi_{12}\right)^{-1} \left(\Psi_{21} \alpha^m \left(\Psi_{11}^m \mathbf{Q}^m + \Psi_{10} \mathbf{H}_0\right) + \left(\mathbf{q} - \Psi_{21} \mathbf{Q}^m\right)\right) \quad (48)$$

Noting that $\mathbf{H}^{m+1} = \mathbf{H}^m + \delta \mathbf{H}^{m+1}$, the expression for \mathbf{H}^{m+1} can be given as

$$\mathbf{H}^{m+1} = -\left(\Psi_{21} \alpha^m \Psi_{12}\right)^{-1} \left(\Psi_{21} \alpha^m \left(\Psi_{11}^m \mathbf{Q}^m + \Psi_{10} \mathbf{H}_0\right) + \left(\mathbf{q} - \Psi_{21} \mathbf{Q}^m\right)\right) \quad (49)$$

Expression for \mathbf{Q}^{m+1} : Substituting Eqs. 39, 40, 44, and 45 in Eq. 37 yields

$$\begin{aligned} \delta\mathbf{Q}^{m+1} = & -\left(\alpha^m - \alpha^m \boldsymbol{\Psi}_{12} \left(\boldsymbol{\Psi}_{21} \alpha^m \boldsymbol{\Psi}_{12}\right)^{-1} \boldsymbol{\Psi}_{21} \alpha^m\right) \left(\boldsymbol{\Psi}_{11}^m \mathbf{Q}^m + \boldsymbol{\Psi}_{12} \mathbf{H}^m + \boldsymbol{\Psi}_{10} \mathbf{H}_0\right) \\ & + \alpha^m \boldsymbol{\Psi}_{12} \left(\boldsymbol{\Psi}_{21} \alpha^m \boldsymbol{\Psi}_{12}\right)^{-1} \left(\mathbf{q} - \boldsymbol{\Psi}_{21} \mathbf{Q}^m\right) \end{aligned} \quad (50)$$

Expanding and simplifying the first term of Eq. 50 yields

$$\begin{aligned} \delta\mathbf{Q}^{m+1} = & -\alpha^m \left(\boldsymbol{\Psi}_{11}^m \mathbf{Q}^m + \boldsymbol{\Psi}_{12} \mathbf{H}^m + \boldsymbol{\Psi}_{10} \mathbf{H}_0\right) + \alpha^m \boldsymbol{\Psi}_{12} \mathbf{H}^m + \alpha^m \boldsymbol{\Psi}_{12} \left(\boldsymbol{\Psi}_{21} \alpha^m \boldsymbol{\Psi}_{12}\right)^{-1} \\ & \left(\boldsymbol{\Psi}_{21} \alpha^m \left(\boldsymbol{\Psi}_{11}^m \mathbf{Q}^m + \boldsymbol{\Psi}_{10} \mathbf{H}_0\right) + \left(\mathbf{q} - \boldsymbol{\Psi}_{21} \mathbf{Q}^m\right)\right) \end{aligned} \quad (51)$$

Noting that the third term in Eq. 51 is equal to $-\alpha^m \boldsymbol{\Psi}_{12} \mathbf{H}^{m+1}$ (Eq. 49), the expression for $\delta\mathbf{Q}^{m+1}$ can be simplified

$$\delta\mathbf{Q}^{m+1} = -\alpha^m \boldsymbol{\Psi}_{12} \mathbf{H}^{m+1} - \alpha^m \left(\boldsymbol{\Psi}_{11}^m \mathbf{Q}^m + \boldsymbol{\Psi}_{12} \mathbf{H}^m + \boldsymbol{\Psi}_{10} \mathbf{H}_0\right) + \alpha^m \boldsymbol{\Psi}_{12} \mathbf{H}^m \quad (52)$$

which can then be reduced further

$$\delta\mathbf{Q}^{m+1} = -\alpha^m \boldsymbol{\Psi}_{12} \mathbf{H}^{m+1} - \alpha^m \left(\boldsymbol{\Psi}_{11}^m \mathbf{Q}^m + \boldsymbol{\Psi}_{10} \mathbf{H}_0\right) \quad (53)$$

Noting that $\mathbf{Q}^{m+1} = \mathbf{Q}^m + \delta\mathbf{Q}^{m+1}$, the expression for \mathbf{Q}^{m+1} can be given as

$$\mathbf{Q}^{m+1} = \left(\mathbf{I} - \alpha^m \boldsymbol{\Psi}_{11}^m\right) \mathbf{Q}^m - \alpha^m \left(\boldsymbol{\Psi}_{12} \mathbf{H}^{m+1} + \boldsymbol{\Psi}_{10} \mathbf{H}_0\right) \quad (54)$$

In terms of the expression, $\left[\left(\boldsymbol{\Psi}'_{11}\right)^m\right]^{-1}$, Eqs. 49 and 54 (i.e., estimates of the system variables, \mathbf{Q}

and \mathbf{H} , at the $(m+1)$ th iteration) can be given as

$$\mathbf{Q}^{m+1} = \left(\mathbf{I} - \left[\left(\boldsymbol{\Psi}'_{11}\right)^m\right]^{-1} \boldsymbol{\Psi}_{11}^m\right) \mathbf{Q}^m - \left[\left(\boldsymbol{\Psi}'_{11}\right)^m\right]^{-1} \left(\boldsymbol{\Psi}_{12} \mathbf{H}^{m+1} + \boldsymbol{\Psi}_{10} \mathbf{H}_0\right) \quad (55)$$

and

$$\mathbf{H}^{m+1} = \left(\boldsymbol{\Psi}_{21} \left[\left(\boldsymbol{\Psi}'_{11}\right)^m\right]^{-1} \boldsymbol{\Psi}_{12}\right)^{-1} \left(\boldsymbol{\Psi}_{21} \left[\left(\boldsymbol{\Psi}'_{11}\right)^m\right]^{-1} \left(\boldsymbol{\Psi}_{11}^m \mathbf{Q}^m + \boldsymbol{\Psi}_{10} \mathbf{H}_0\right) + \left(\mathbf{q} - \boldsymbol{\Psi}_{21} \mathbf{Q}^m\right)\right) \quad (56)$$

The computational steps for determining the system variables, \mathbf{Q} and \mathbf{H} , at the $(m+1)$ th iteration (Eqs. 55 and 56) within the context of a Newton-Raphson iterative procedure is presented in section 4.3. Before that, however, a discussion on initialization of the variable vectors and on updating the matrices, of Eqs. 55 and 56, in each gradient iteration is presented in section 4.2.

4.2. Initialization of variable vectors and updating matrices in each gradient iteration

In order to compute a revised estimate of the variable vector, \mathbf{Q} and \mathbf{H} , at the $(m+1)$ th iteration, with Eqs. 55 and 56, the matrices Ψ_{10} , Ψ_{12} , Ψ_{21} , Ψ_{11}^m , $(\Psi_{11}')^m$, $[(\Psi_{11}')^m]^{-1}$, $(\Psi_{21} [(\Psi_{11}')^m]^{-1} \Psi_{12})^{-1}$, and the vectors \mathbf{H}_0 , \mathbf{q} , and \mathbf{Q}^m need to be known. The approaches used, in the current model, for initialization of the system variables and for updating these matrices in each iteration are described here.

4.2.1. Initialization of the system variable vectors, \mathbf{Q} and \mathbf{H}

The nodal head at the inlet end of a lateral, H_{01} , is specified as an input. The initial heads at each of the junction nodes downstream of the lateral inlet, \mathbf{H}^0 , are calculated assuming a linear initial nodal head profile that decreases from the inlet to the distal end of the lateral by a total amount of $0.05H_{01}$. Noting that the gradient method does not require the initial discharge vector to satisfy continuity requirement, for each emitter the initial discharges, Q_i^0 , are computed with the emitter head discharge function based on the local nodal heads. The initial emitter discharges along with the residual discharge at the downstream end of the lateral are used to calculate initial lateral pipe segment discharges.

4.2.2. Constant vectors \mathbf{q} and \mathbf{H}_0

The fixed nodal heads, \mathbf{H}_0 , and the constant in- or out-flows at junction nodes, \mathbf{q} , are specified as model inputs. For irrigation laterals the elements of the \mathbf{q} vector are zero except for the residual discharge at the downstream end of the lateral. The elements of the \mathbf{H}_0 vector consists of the known heads at the boundary nodes, which includes the head at the inlet end of the lateral and elevations of the emitters. These vectors are set at the start of the computation ($m = 0$) and remain unaltered in subsequent iterations.

4.2.3. Network connectivity matrices Ψ_{10} , Ψ_{12} , and Ψ_{21} and the vector $\mathbf{A}_{10}\mathbf{H}_0$

The matrices Ψ_{10} , Ψ_{12} , and Ψ_{21} are formed at the variable initialization phase in accordance with Eq. 20. For irrigation lateral, these matrices remain unchanged through

subsequent iterations. The product $\Psi_{10}H_0$ is also a constant vector computed at the start of the simulation and need not be updated in subsequent iterations.

4.2.4. Computation of the Ψ_{11} matrix (Table 6 and Eq. 29) at the $(m+1)$ th iteration

The Ψ_{11} matrix, evaluated based on the link discharge vector at the m th iteration, Q^m , is used in the $(m+1)$ th iteration. This matrix is composed of two sets of alternating rows, the rows related to the head loss equations for pipe segments, on one hand, and those related to the energy equations for riser-emitter ensembles or emitters, on the other. Elements in these rows are computed as follows

(i) *Matrix rows related to lateral pipe segment energy equations (i.e., odd numbered rows in the Ψ_{11} matrix):*

Each element in the i th row of the Ψ_{11} matrix represents the product $\tau_q\theta_i$ for the i th link of the lateral (Eq. 21). As can be noted from Eq. 22 and also Table 6, for the i th row only one of these products (i.e., the diagonal element of Ψ_{11} , the element for which $i = q$) is nonzero.

For the i th pipe segment, the parameter θ_i is the parenthetical expression on the left hand side of Eq. 11. Hence θ_i is the sum of a term related to friction head loss and another term related to local head losses (Table 1). The local head loss terms, in the expression for θ_i , can be evaluated directly given applicable coefficients. However, the friction head loss term is a function of the i th pipe segment discharge at the m th iteration, Q_i^m , and the hydraulic resistance coefficient, β_i (Eq. 12). β_i is a function the pipe segment length, diameter, and Darcy-Weisbach friction factor, f_i . Pipe segment length and diameter are inputs to the model, but f_i needs to be computed as a function of Q_i^m . For flows with Reynolds number, Re , not exceeding 4000, the friction factor can be calculated directly with Eq. 5. For turbulent flow, however, the formula is implicit in the friction factor, thus the friction factor needs to be computed iteratively. The iterative procedure for computing f_i , implemented in the current model, is presented in Appendix II. Note that the numerical algorithm for computing f_i is described within the context of the larger sub-process for computing the Ψ_{11} matrix, which is presented in Appendix III. Observe that at any given iteration - say at the $(m+1)$ th gradient iteration - f_i and matrix Ψ_{11} are computed based on the i th lateral pipe segment discharge at the m th iteration, Q_i^m .

(ii) Rows related to riser-emitter ensemble or emitter (i.e., even numbered rows in the Ψ_{11} matrix):

As noted above, each entry in the i th row of the Ψ_{11} matrix represents the product $\tau_q \theta_i$ for the i th link in the lateral (Eq. 21). Furthermore, for the i th row (i.e., the i th emitter) only one of these products (i.e., the diagonal element of Ψ_{11}) is nonzero (Table 6).

Considering a scenario in which the emitter is placed on a riser, the parameter θ_i for the i th riser-emitter ensemble is given in terms of the expression in parenthesis on the left-hand side of Eq. 16. Hence θ_i is the sum of a term related to the emitter head-discharge characteristic function and another term related to friction head loss in the riser pipe (Table 1). The term related to emitter head-discharge characteristics can be evaluated directly. However, the term related to friction head loss needs to be evaluated following the approach described for a lateral pipe segment in *step i* above.

For the case in which emitters are placed directly on laterals the expression for θ_i consists of only the term related to the emitter head-discharge function (Eq. 17) and can be evaluated directly.

4.2.5. Computation of the Ψ'_{11} matrix (Table 8 and Eq. 33) at the $(m+1)$ th iteration

The Ψ'_{11} matrix, evaluated based on the link discharge vector at the m th iteration, Q^m , is used in the $(m+1)$ th iteration. Each row of the Ψ'_{11} matrix is a subset of the transpose of the gradient vector of the corresponding link energy balance equation (Table 8). As is the case with the Ψ_{11} matrix, the Ψ'_{11} matrix is comprised of two sets of alternating rows, the rows related to the head loss equations for lateral pipe segments, on one hand, and those related to the energy equations for riser-emitter ensembles or emitters, on the other. Elements in these rows are computed as follows

(i) Matrix rows related to lateral pipe segment energy equations (odd numbered rows of the Ψ'_{11} matrix):

It follows from the preceding description of the link energy balance equations (Eq. 21) that for the i th row only one of the elements (i.e., a diagonal element) of the Ψ'_{11} matrix is nonzero (Table 8). Furthermore, it can be observed that the diagonal element on the

i th row of the Ψ_{11}' matrix is equal to the derivative of Eq. 21 with respect to the i th lateral pipe segment discharge, which essentially reduces to the derivative of Eq. 11

$$F'_{eQ_i} = \frac{\partial(\beta_i Q_i^2)}{\partial Q_i} + \sum_p \frac{\partial(\pi_i^p Q_i^2)}{\partial Q_i} \quad (57)$$

where F'_{eQ_i} is the derivative of the i th link energy balance equation with respect to the i th link discharge (Table 8).

Note that Eq. 11 represents a more general form of the head loss equation for a pipe segment, where link flow direction relative to the path is taken into account. However, Eq. 57 has a simpler form, in which the link flow direction relative to the path is not explicitly considered. The reason is that in the simple branched hydraulic network considered here the direction of flow is known and is the same as the path followed in formulating pertinent equations.

Expanding Eq. 57 yields

$$F'_{eQ_i} = Q_i^2 \frac{\partial \beta_i}{\partial Q_i} + 2\beta_i Q_i + 2 \sum_p \pi_i^p Q_i \quad (58)$$

Substituting the expressions for β_i and π_i^p (Eqs. 12 and 13) in Eq. 58 results in

$$F'_{eQ_i} = \left(\left(k_l \frac{L_i}{D_i^5} \right) \left(Q_i \frac{\partial f_i}{\partial Q_i} + 2f_i \right) + 2 \frac{k_3}{D_i^4} \sum_p k_{Li}^p \right) Q_i \quad (59)$$

In Eq. 59, the local head loss terms can be evaluated directly once the appropriate head loss coefficients, k_L , are known. However, the friction head loss term can be fully evaluated only after the derivative of f_i with respect to the pipe discharge, Q_i , is determined. The derivatives of the friction factor with respect to the i th lateral pipe segment discharge, $\frac{\partial f_i}{\partial Q_i}$, are

$$\frac{\partial f_i}{\partial Q_i} = -\frac{64}{Re_i Q_i}, \quad \text{for } Re_i \leq 4000 \quad (60)$$

and

$$\frac{\partial f_i}{\partial Q_i} = -16.25 \frac{f_i}{Q_i \left[R_{ei} \left(\frac{e_i}{D_i} + \frac{9.35}{R_{ei} \sqrt{f_i}} \right) + 8.125 \right]} \quad \text{for } 4000 < R_e \quad (61)$$

Derivation of the expressions in Eqs. 60 and 61 are presented in Appendix IV. The f_i' value calculated with Eq. 60 or 61, as the case may be, is then substituted in Eq. 59 to compute the diagonal element of the i th row of matrix Ψ_{11}' . The numerical algorithm, implemented in the model, for computing matrix Ψ_{11}' is presented in Appendix V. Note that at the $(m+1)$ th gradient iteration, f_i' (Eq. 60 or 61) and the elements of matrix $(\Psi_{11}')^m$ (Eq. 59) are computed based on the i th lateral pipe segment discharge at the m th iteration, Q_i^m .

(ii) *Rows related to emitters (even numbered rows)*: It follows from the energy balance equation (Eq. 21) that for the i th row only one of the elements (i.e., a diagonal element) of the Ψ_{11}' matrix is nonzero (Table 8). Furthermore, considering a scenario in which the emitter is placed on a riser, the diagonal element on the i th row of the Ψ_{11}' matrix is equal to the derivative of Eq. 21 with respect to the i th emitter discharge, which essentially reduces to the derivative of Eq. 16

$$F'_{eQ_i} = \xi_i^l \beta_i^l Q_i^{(\xi_i^l - 1)} + \frac{\partial(\beta_i Q_i^2)}{\partial Q_i} \quad (62)$$

Equation 16 represents a more general form of the energy equation for an emitter/riser-emitter ensemble. However, noting that the flow in a lateral has a known direction and is the same as the path assumed to formulate the equation, a simpler form is used to obtain the derivatives of the energy equation for the i th emitter (Eq. 62). In Eq. 62 the first and second terms, on the right hand side, are the derivatives, with respect to emitter discharge, of the emitter head-discharge function and the friction head loss in the riser pipe, respectively. The first term can be evaluated directly and the second term needs to be evaluated following the same procedure as that described for lateral pipe segments (*step i*). Note that for the case in which emitters are placed directly on the lateral, the friction head loss term in Eq. 62 drops out resulting in a form that can be evaluated directly.

4.2.6. Computation of the inverses of the $(\Psi'_{11})^m$ and $\left(\Psi_{21} \left[(\Psi'_{11})^m \right]^{-1} \Psi_{12}\right)$ matrices

As noted in the preceding section the inverse of matrices Ψ'_{11} and $\Psi_{21} \left[(\Psi'_{11})^m \right]^{-1} \Psi_{12}$ need to be computed before \mathbf{H}^{m+1} and \mathbf{Q}^{m+1} can be evaluated with Eqs. 55 and 56. An approach based on *LU* factorization is used to compute the inverse of these matrices. A detailed discussion of the steps used in computing the inverses of these matrices with the *LU* factorization method, as implemented in the model developed in the current study, is presented in Appendix VI. An outline of the basic concept, broadly based on the discussion by Press et al. (1997), will be presented concisely in this section.

Consider a square matrix, \mathbf{A} , of some arbitrary dimension, $q \times q$, with elements labeled as Δ_{ij} , such that

$$\Delta_{ij} \in \mathbf{R} \quad (63)$$

In Eq. 63, i and j are row and column indices, respectively, of matrix \mathbf{A} ; \mathbf{R} is the set of real numbers; and \in is the standard set notation that implies that Δ_{ij} is a member of the set of real numbers.

Further assume that matrix \mathbf{A} is nonsingular and has an inverse, \mathbf{A}^{-1} , then by definition

$$\mathbf{I} = \mathbf{A}\mathbf{A}^{-1} \quad (64)$$

where \mathbf{I} is identity matrix with the same dimension as \mathbf{A} and can be defined as

$$\lambda_{ij} = \begin{cases} 1, & \text{for } i = j \\ 0, & \text{for } i \neq j \end{cases} \quad (65)$$

In Eq. 65, λ_{ij} is the element of \mathbf{I} on its i th row and j th column. Note that \mathbf{A}^{-1} has the same dimension as \mathbf{A} and its elements, labeled here as σ_{ij} , are real numbers.

We assume here that matrix \mathbf{A} can be factorized into a lower triangular, \mathbf{L} , and an upper triangular, \mathbf{U} , matrices with *LU* factorization method, such that

$$\mathbf{A} = \mathbf{LU} \quad (66)$$

Substituting Eq. 66 in Eq. 64 yields

$$\mathbf{I} = \mathbf{LU}\mathbf{A}^{-1} \quad (67)$$

Letting

$$\mathbf{\Phi} = \mathbf{U}\mathbf{A}^{-1} \quad (68)$$

where $\mathbf{\Phi}$ is a $q \times q$ matrix with elements ϕ_{ij} , such that $\phi_{ij} \in \mathbf{R}$; Eq. 67 can be expressed as

$$\mathbf{I} = \mathbf{L}\mathbf{\Phi} \quad (69)$$

Computation of the inverse of matrix \mathbf{A} , \mathbf{A}^{-1} , with an LU factorization algorithm is then undertaken in the following steps

- i. *Factorize \mathbf{A}* : Factorize matrix \mathbf{A} into a lower, \mathbf{L} , and an upper, \mathbf{U} , triangular matrices (Eq. 66) with Crout's method;
- ii. *Compute $\mathbf{\Phi}$* : Compute $\mathbf{\Phi}$ (Eq. 69) through forward substitution, starting from the first row and proceeding sequentially down to the bottom row;
- iii. *Compute \mathbf{A}^{-1}* : Compute \mathbf{A}^{-1} (Eq. 68) through back substitution, starting from the bottom row and proceeding sequentially up to the first row;

4.3. Numerical algorithm

The lateral hydraulic simulation model presented here is a C++ program, developed based on the numerical procedures described in sections 4.1, 4.2, and Appendix I-VII. Given the hydraulic, geometric, and slope data of a lateral, computation starts with initialization of system variables (\mathbf{Q} and \mathbf{H}), and setting up the network connectivity matrices ($\mathbf{\Psi}_{10}$, $\mathbf{\Psi}_{12}$, and $\mathbf{\Psi}_{21}$), and constant vectors (\mathbf{q} and \mathbf{H}_0). A flow chart depicting the Newton-Raphson iterative procedure for computing the system variables (\mathbf{Q} and \mathbf{H}), as implemented in the current model, is presented in Figure 6. The following is a summary of the computational steps

1. Set $m = 0$ (where m is the gradient iteration index) and proceed to step 2;
2. Initialize system variables: \mathbf{Q}^0 and \mathbf{H}^0 and proceed to step 3;

3. Create matrices: Ψ_{10} , Ψ_{12} , Ψ_{21} , \mathbf{q} , \mathbf{H}_0 , and compute the constant vector $\Psi_{10}\mathbf{H}_0$ and proceed to step 4;
4. Compute matrix Ψ_{11}^m (i.e., the Ψ_{11} matrix at the m th gradient iteration) and proceed to step 5;
(Note: The sub-process implemented in the model for computing Ψ_{11}^m is described in Appendix III);
5. If $0 < m$, proceed to step 6; If $m = 0$, proceed to step 10;
6. Compute residuals of energy balance, \mathbf{F}_e^m , and continuity, \mathbf{F}_c^m , with Eqs. 44 and 45; proceed to step 7;
7. Convergence test, proceed to step 7a:
 - 7a. Energy balance equations: If $|\mathbf{F}_e^m| \leq 10^{-7}$, proceed to step 7b; If not proceed to step 8;
 - 7b. Continuity equations: If $|\mathbf{F}_c^m| \leq 10^{-7}$, proceed to step 14; If not proceed to step 8;
8. If $m \leq \text{MaxIteration}$, proceed to 10; If $\text{MaxIteration} < m$, proceed to step 9; (where MaxIteration is the maximum number of allowable gradient iterations and is internally set in the model to 30);
9. Newton iteration failed to converge, end computation;
10. Compute matrix $(\Psi_{11}')^m$ (i.e., the Ψ_{11}' matrix at the m th iteration) and proceed to step 11;
(Note: the sub-process implemented in the model for computing $(\Psi_{11}')^m$ is described in Appendix V)
11. Compute \mathbf{H}^{m+1} in steps 11.1 to 11.4; (Note: A simplified flow chart depicting the sub-processes for computing \mathbf{H}^{m+1} is shown in Figure 7)

11.1. Compute Θ_1

$$\Theta_1 = - \left(\Psi_{21} \left[(\Psi_{11}')^m \right]^{-1} \Psi_{12} \right)^{-1} \quad (70)$$

and proceed to step 11.2

11.2. Compute Θ_2

$$\Theta_2 = \Psi_{21} \left[(\Psi_{11}')^m \right]^{-1} (\Psi_{11}^m \mathbf{Q}^m + \Psi_{10} \mathbf{H}_0) \quad (71)$$

and proceed to step 11.3;

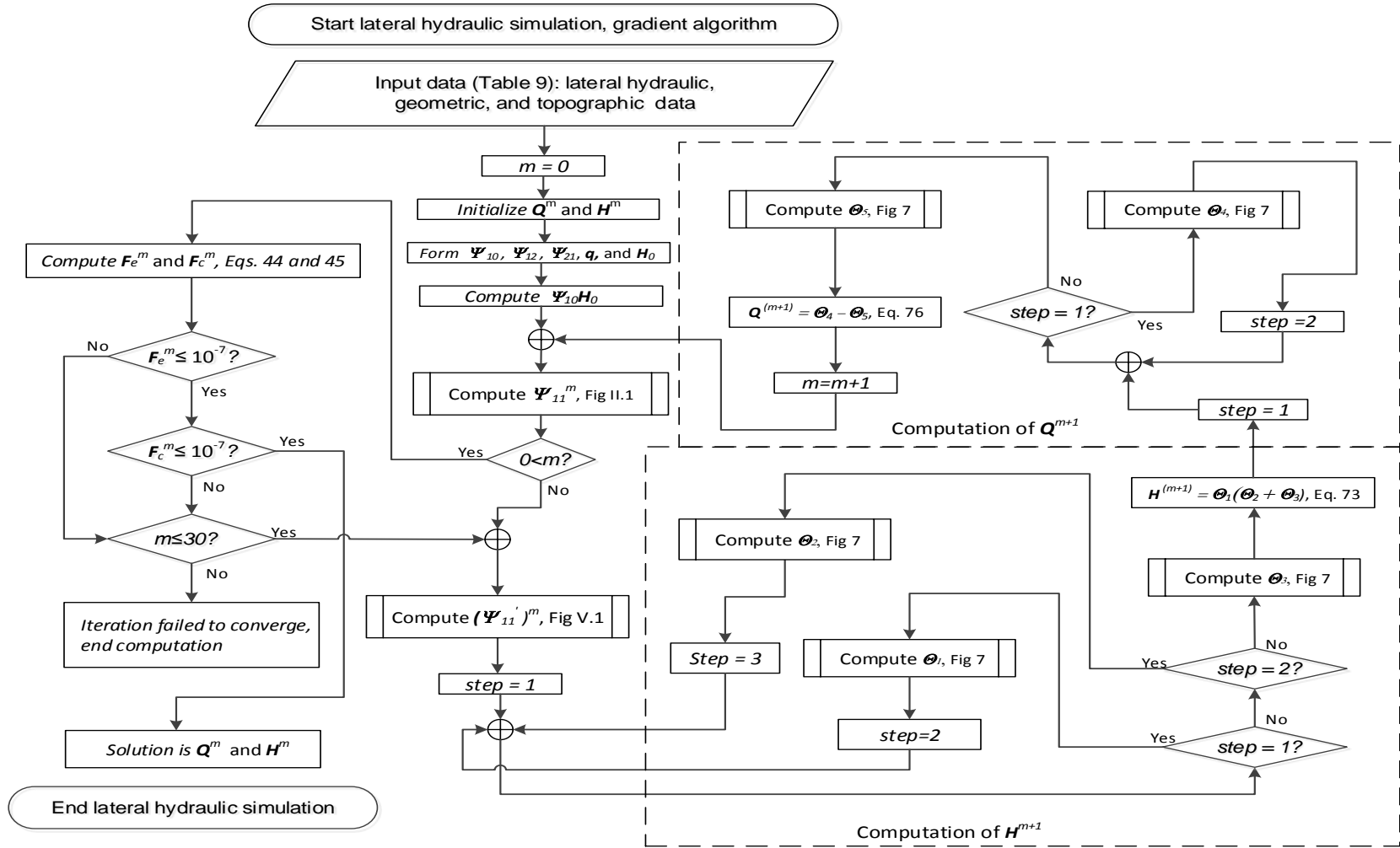


Figure 6. Flow chart depicting the gradient algorithm implemented in the lateral hydraulic model (where m is gradient iteration index; Q and H are link discharge and nodal continuity vectors, respectively; H_0 and q are fixed nodal heads and discharge vectors, respectively; Ψ_{10} , Ψ_{12} , Ψ_{21} are network connectivity matrices; Ψ_{11} and Ψ_{11}' are matrices in Eqs. 29 and 33, respectively; F_e and F_c are residuals of the link energy balance and nodal continuity equations, respectively; $step$ is index of intermediate computational steps; and θ_1 - θ_5 are variables for representing intermediate outputs)

11.3. Compute Θ_3

$$\Theta_3 = \mathbf{q} - \Psi_{21} \mathbf{Q}^m \quad (72)$$

and proceed to step 11.4;

11.4. Determine \mathbf{H}^{m+1}

$$\mathbf{H}^{m+1} = \Theta_1 (\Theta_2 + \Theta_3) \quad (73)$$

and proceed to step 12;

12. Compute \mathbf{Q}^{m+1} in steps 12.1 to 12.3 (*Note: A simplified flow chart depicting the sub-process for computing \mathbf{Q}^{m+1} is shown in Figure 7*):

12.1. Compute Θ_4

$$\Theta_4 = \left(\mathbf{I} - \left[(\Psi'_{11})^m \right]^{-1} \Psi_{11}^m \right) \mathbf{Q}^m \quad (74)$$

and proceed to step 12.2;

12.2. Compute Θ_5

$$\Theta_5 = \left[(\Psi'_{11})^m \right]^{-1} (\Psi_{12} \mathbf{H}^{m+1} + \Psi_{10} \mathbf{H}_0) \quad (75)$$

and proceed to step 12.3;

12.3. Determine \mathbf{Q}^{m+1}

$$\mathbf{Q}^{m+1} = \Theta_4 - \Theta_5 \quad (76)$$

and proceed to step 13;

13. Set iteration index $m = m+1$ and proceed to step 4;

14. Solution vector is \mathbf{Q}^m and \mathbf{H}^m , end computation;

4.4. Model inputs and outputs

The model developed in the current study obtains its input data from space delimited text file. The input data file has a tabular format, which is designed to provide sufficient flexibility for taking into account spatial variations in the input data. In the input data table, each row represents the hydraulic, geometric, and elevation data relating to a hydraulic link, and associated nodes, of the lateral. The specific data items include: lateral pipe segment length, diameter, relative roughness, distance between a node and the inlet end of the lateral, nodal elevation, emitter discharge coefficients, riser pipe data, and local head loss coefficients for pipe appurtenances. The input data file also contains nontabular data, which includes residual discharge at the downstream end of the lateral, total head at the inlet end of the lateral, and data items related to lateral configuration.

The model produces various types of output data following a successful simulation. The main outputs of the numerical simulation are the link discharge vector (discharges in lateral pipe segments and emitters), Q , and total heads at each of the lateral junction nodes, H . In addition, the model generates such outputs as velocity heads and friction head losses in each of the lateral pipe segments, local head losses, head differential across each emitter, pressure head at each junction node, and piezometric head profile along the lateral.

5. Model evaluation

Evaluation of the lateral hydraulic simulation model, developed here, is conducted at different levels. First the consistency of the numerical solution implemented in the model was tested by comparing intermediate and final outputs of the model with manual calculations. Then the outputs of the model are compared with those of EPANET (Rossman, 2000) and another model developed based on manifold hydraulics (Zerihun et al., 2014). The model is further evaluated based on comparisons of its outputs with field measured data. Finally, sensitivity analysis is conducted in order to evaluate the spatial patterns of model predicted lateral hydraulic characteristics under a range of conditions.

5.1. Data description

The data sets used in model evaluation are summarized in Table 9. Data sets 1, 2, and 3 are hypothetical and data sets 4 to 7 are obtained through field measurements (Zerihun et al., 2011). These data sets cover a wide range of hydraulic, geometric, and slope conditions. Lateral

Table 9. Data used in model evaluation

<i>Lateral variables/parameters</i>	<i>Units</i>	<i>Data sets^(a)</i>			
		<i>1</i>	<i>2</i>	<i>3</i>	<i>4-7^(b)</i>
Sprinkler spacing	<i>m</i>	10.0	10.0	10.0	9.14
Coefficient of sprinkler pressure head discharge function, ρ_1 , ^(c)	<i>L/(s m^{ρ₂})</i>	0.0258	0.0258	0.0125	0.0125
Exponent of sprinkler pressure head discharge function, ρ_2 ,	-	0.502	0.502	0.521	0.521
Lateral diameter ^(d)	<i>mm</i>	50.8	101.6	76.2/50.8/38.1	76.2
Lateral length	<i>m</i>	300.0	300.0	400.0	374.7
Lateral slope ^(e)	-	0.0	+0.005	-0.001	-0.0004/-0.0006
Constant total head at the lateral inlet ^(f)	<i>m</i>	50.0	45.0	50.0	152.0-157.0
Residual discharge at downstream end	<i>L/s</i>	1.5	2.75	0.0	0.0

- ^(a) The laterals considered here are those used in solid-set or set-move sprinkler systems and the sprinkler riser pipe height and diameter are 46.0cm and 12.5mm, respectively; furthermore, all laterals are assumed to be consisting of aluminum pipe segments and the corresponding pipe absolute roughness is set at 0.127mm (Keller and Bliesner, 1990);
- ^(b) Data sets 4 to 7 represent measured data along four laterals of a solid-set sprinkler system (Zerihun et al., 2011). The laterals have the same geometric and hydraulic characteristics, except for the average longitudinal slope and total head and elevation at the lateral inlet;
- ^(c) The sprinkler used in these laterals are impact sprinklers and the models and nozzle sizes are: for data sets 1 and 2, WeatherTec 10-20 with nozzle size of 7/64"; for data sets 3 to 7, WeatherTec 10-10 with nozzle size of 5/64"; ρ_1 and ρ_2 are the coefficient and exponent of the sprinkler head-discharge function obtained based on the sprinkler pressure and discharge data in manufacturer's catalogue (<https://www.weathertec.com>);
- ^(d) In data set 3 the lateral has three sections each with different diameters: 76.2mm between 0.0 and 130.0m, 50.8mm from 130.0 to 270.0m, and 38.1mm between 270.0 and 400.0m; the local head loss coefficients used are 0.27 for the location at which pipe size changes from 76.2 to 50.8mm and 0.17 for the location where pipe diameter changes from 50.8 to 38.1mm (Granger, 1995);
- ^(e) Lateral slope for data sets 4 to 7 vary between 0.06% (data sets 4, 6, and 7) to 0.04% (data set 5); furthermore, elevations at the lateral inlets are: 0.0m (data set 1), 10.0m (data sets 2 and 3), and vary between 98.859 and 99.523m for data sets 4 to 7;
- ^(f) Total head at the lateral inlet of data sets 4 to 7 are: 152.0 (data set 7), 153.0 (data set 6), 155.0 (data set 5) and 157.0m (data set 4). Measurements along these lateral (which belong to the same field-scale sprinkler system) were made in the course of different irrigation events, hence the differences in total head along mainline;

diameters range between 50.8mm (data set 1) and 101.6mm (data set 2). Data set 3 represents a lateral with sections that have three different diameters (76.2mm, 50.8mm, and 38.1mm). The slope of the laterals vary from -0.04% for data set 5 to 0.5% for data set 2. Lateral lengths range between 300.0m (data sets 1 and 2) and 400.0m (data set 3). Residual outflow at the downstream end of the laterals vary between 0.0L/s (data sets 3 to 7) and 2.75L/s (data set 2). Total head at lateral inlet vary from 45.0m for data set 2 to 157.0m for data set 4. Lateral inlet elevations vary from 0.0m (data set 1) to 99.523m (data set 4). Two sprinkler models and nozzle sizes with significantly different head-discharge characteristics are used in these laterals.

Data sets 1 to 5 are used in evaluating the consistency of the numerical solution of the model developed in the current study. These data sets are also used in comparing the output of the model, presented here, with EPANET and another model developed, by the same authors, based on manifold hydraulics. Data sets 4 to 7 are used in evaluation of the model with field measured. Data set 4 is used in sensitivity analysis. Note that for simplicity of presentation, where convenient the term lateral is used in place of the term data set in this chapter.

5.2. Consistency test of the numerical solution implemented in the lateral hydraulic simulation model

5.2.1. Test factors and criterion

The consistency of the numerical solution developed based on the gradient method is evaluated by comparing the intermediate and final outputs of the model with manual calculations. The goal is to evaluate if the different functions and component modules of the model are performing the functions they are designed for. Four hydraulic variables and parameters are selected for conducting these tests: the Darcy-Weisbach friction factor for each lateral pipe segment, f , the sprinkler discharges, Q_s , lateral discharges, Q , and total nodal heads, H . Note that in the preceding sections of this document both lateral and sprinkler discharges are labeled as Q . However, in order to simplify discussion, in subsequent sections distinction is made between sprinkler discharge, Q_s , and lateral discharge, Q .

Friction factor, f : The model computes the friction factor, f , for each lateral pipe segment iteratively in accordance with the steps outlined in Appendix II. Given estimates of f and Q for a lateral pipe segment, computed by the model, along with the corresponding pipe diameter, D ,

and absolute roughness, e , specified at the input; a revised estimate of the friction factor, f^r , for the lateral pipe segment can be calculated manually with Eq. 77

$$f^r = \frac{l}{\left(1.14 - 2 \log \left(\frac{e}{D} + \frac{9.35}{R_e \sqrt{f}} \right) \right)^2} \quad (77)$$

Now one may observe that for the model computed f vector to be acceptable, the revised estimates, f^r , calculated manually with Eq. 77 should be sufficiently close to the f array. Accordingly, the absolute difference between f^r and f expressed as percentage of f^r is used here as the criteria for evaluating the acceptability of the f array computed by the model.

Sprinkler discharge, Q_s : From Eqs. 16 and 17 it can be noted that the head differential across a sprinkler is expressed as a power function of the sprinkler discharge. The model computed head differential across sprinklers along with the coefficients and exponents of the sprinkler head-discharge functions, specified as model inputs, can be used to manually calculate the discharges for each sprinkler along the lateral. For the sprinkler head and discharge vectors computed by the model to be considered acceptable, the manually computed and model predicted sprinkler discharges should be close. Accordingly, the differences between the model computed and manually calculated sprinkler discharges, expressed as percentages of the manually calculated discharges, are used to test the consistency of the numerical solution as regards sprinkler head and discharge computation.

Lateral discharges, Q : The discharge vector computed by the numerical model can be checked manually if it meets junction node continuity requirements. Considering the downstream end node of the lateral, one can manually calculate an approximation of the discharge into the node (through the lateral segment immediately upstream) as the sum of the model computed local sprinkler discharge and the constant residual discharge at the downstream end of the lateral (specified as an input). Likewise, for the node immediately upstream, an approximation of the discharge into the node can be calculated manually as the sum of the model computed local sprinkler discharge and the discharge in the lateral segment immediately downstream of the node. This steps can then be repeated for all the junction nodes by moving sequentially upstream along the lateral. It can be observed that the absolute difference between the manually calculated and

model computed lateral discharges, upstream of each junction node, should be within the error tolerance set in the model for the residuals of continuity (which is 10^{-7}). The difference between the manually computed lateral discharge upstream of a junction node and that obtained through numerical solution, expressed as percentage of the manually computed value, is used here in assessing the satisfaction of continuity requirements at junction nodes.

Total head, H : The nodal heads, H , and the link discharges are computed as part of the numerical solution. Consistency tests relating to discharges have been discussed in the preceding paragraphs, hence the discussion here focuses on consistency test for the model computed H values. The total head at the upstream end of a lateral is constant and is specified at the input. The total head at the junction node just downstream of the inlet end of the lateral can be determined by subtracting the manually calculated friction head loss, in the upstream end lateral pipe segment, from the total head at the lateral inlet. The total head at each of the junction node downstream of the first can be calculated following the same approach. The manually calculated and the simulated total nodal heads must be sufficiently close. The difference between the simulated and manually calculated H , expressed as a percentage of the manually calculated H , is used there to assess the consistency of the numerical computation with respect to nodal heads.

5.2.2. Results of consistency test

Five data sets are used in the evaluation of the consistency of the numerical solution implemented in the model developed in the current study (data sets 1 to 5, Table 9). As noted above, the percent differences between the manually calculated and model computed values of each of the parameters and variables considered here (i.e., f , Q_s , Q , and H), expressed as percentages of the manually calculated values, are used as quantitative measures of the consistency of the numerical solution. For each parameter and variable, the minimum, maximum, and average percent differences between the manually calculated and model computed values are presented in Figures 8a-8d. In order to produce sufficient spread between the data points, the ordinates of these graphs are in logarithmic scale. The minimum percent differences, for some of the data sets, are not shown in Figures 8a-8d. The reason is the minimum percent differences at those data sets are 0.0%, hence cannot be shown in a logarithmic scale graph.

Considering all the data sets, the smallest percent difference between model computations and manual calculations are obtained for the friction factor, f (Figures 8a-8d). The maximum

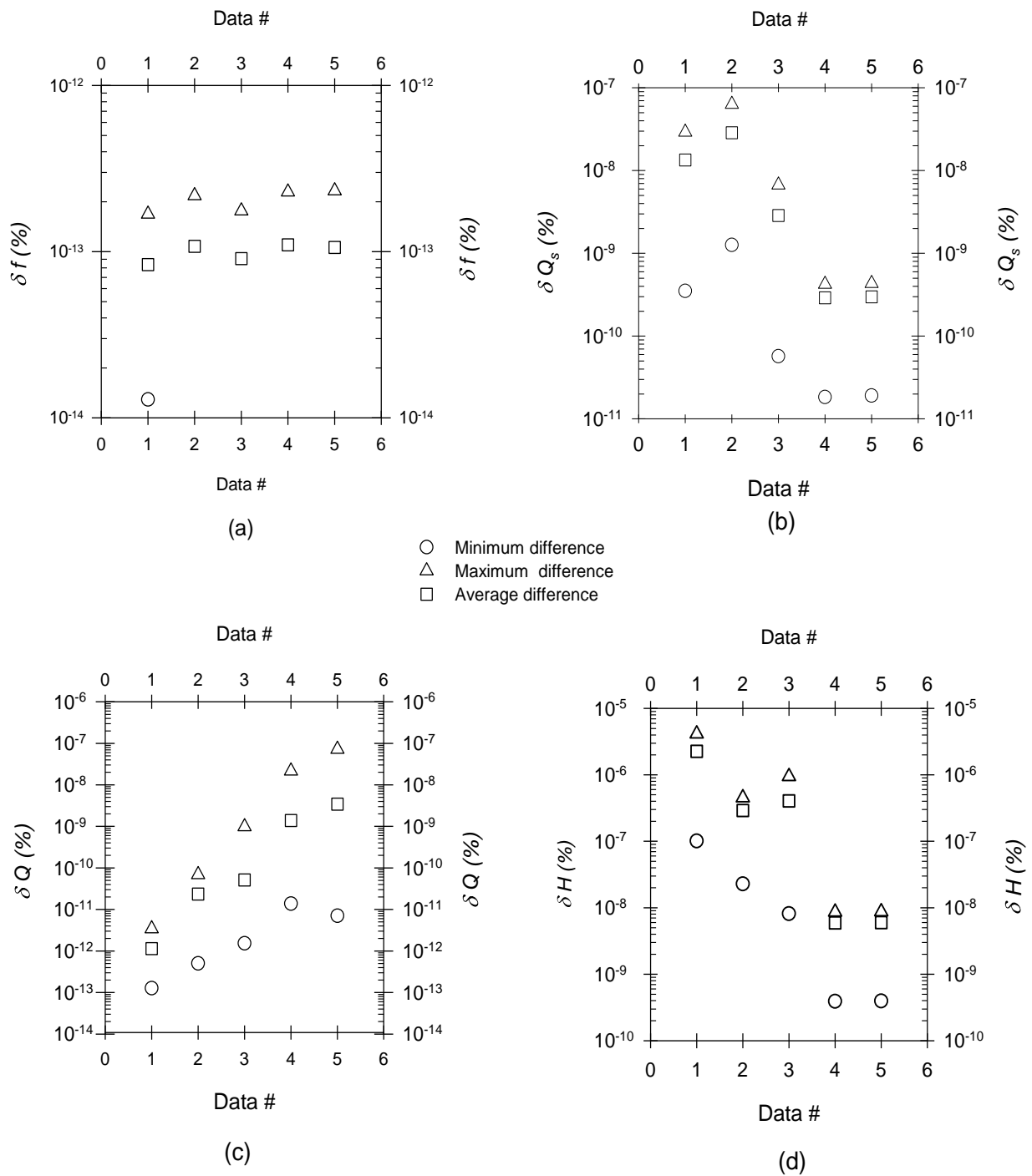


Figure 8. Graphs showing percent differences between model computed and manually calculated hydraulic variables and parameters, expressed as percentage of the manually calculated values: (a) Percent difference in friction factor, δf , (b) Percent difference in sprinkler discharge, δQ_s , (c) Percent difference in lateral discharge, δQ , and (d) Percent difference in total nodal head, δH

percent differences are in the order of $10^{-13}\%$ of the manually calculated f values (Figure 8a). The minimum percent differences, between the manually calculated and model computed f values, for all the data sets are about or less than $10^{-14}\%$ of the manually calculated values. The average percent differences are about half of the maximum differences. The largest difference between model and manual computations is obtained for the total head, H . Considering all the data sets, the maximum percent difference for H vary between about 10^{-8} and $10^{-5.4}\%$ and the minimum percent difference range from about $10^{-9.4}$ to $10^{-7}\%$ (Figure 8d). The average percent difference vary between $10^{-8.2}$ and $10^{-5.6}\%$.

The percent differences between manually calculated and model computed lateral and sprinkler discharges are closer to those obtained for H compared to those calculated for f . The percent differences for the lateral discharges fall somewhere in between those calculated for f and H . Furthermore, a close examination of the Q data show that the absolute differences between the manually calculated and model computed values of Q , for all the data sets, meet the error tolerance criteria set internally in the model for the residuals of continuity. Considering all the parameters and variables, the percent differences between the manual calculations and model computations are overall in the order of $10^{-5.4}\%$ or less (Figures 8a-8d). These results show that the manually calculated and model computed parameters and variables are in good agreement, thus there is no evidence of internally inconsistency in the model computations.

In the preceding discussion, variations can be noted in the percent differences calculated for the different parameters and variables (Figures 8a-8d). It may not be possible to explain with certainty the source of these variations. However, it is likely that they are largely attributable to the differences in the levels of complexity with which each variable and parameter is computed in the model. In order to explain this observation, we will first explore the sources of the differences between model computed and manually calculated values of a parameter or variable.

For the most part model computed values of variables and parameters, listed above, are the results of a series of complex intermediate mathematical operations. By contrast, the manual calculations are based on direct evaluation of simple explicit functions that are dependent on a few input data items and at most two model outputs. Evidently, the elemental formulas and equations used in both approaches are generally based on the same physical principles and the main source of error in both approaches is rounding-off error, associated with the representation of real numbers in computer hardware and software. However, there are significant differences,

between the manual calculations and the numerical computations performed by the model, in terms of the individual mathematical operations originating the errors and the evolution of errors in the course of a calculation/computation aimed at determining a parameter or a variable. These may largely account for the observed differences between the model computed and the manually calculated values of a parameter or variable.

An inference that stems from the preceding discussion is that the variables and parameters computed in the model with relatively simple and direct procedures may lead to results that are relatively closer to the manual calculations. Whereas those variables and parameters computed, in the model, through a long series of intermediate calculations may be, in relative terms, appreciably different from those computed manually. One may note some evidence to this effect in the results presented in Figures 8a-8d. For instance for all the data sets, the friction factor, f , arrays, which are computed in the model with a relatively simple and direct procedure (that requires minimal inputs, only Q , from prior computations), are almost identical to those computed manually. Conversely, the Q , Q_s , and H vectors, computed based on a complex set of iterative steps each requiring various matrix operations on several matrices (section 4), are the variables with the highest percent differences between manual calculations and model computations. The preceding may, at least partially, explain the observed variations between the percent differences computed for the different parameters and variables.

5.3. Comparison of the model based on the gradient method with that based on manifold hydraulics

5.3.1. Introductory discussion

The model developed in the current study treats the pressurized irrigation system lateral as a simple branched hydraulic network. The gradient method is used in the formulation and solution of the lateral hydraulic simulation problem. With the gradient method, the energy conservation equation for steady-state condition is applied across each link and the continuity equation is written for each junction node along a lateral. The equations are then coupled and the resultant system is solved iteratively (section 4). Alternatively, a lateral can be treated as a hydraulic manifold, in which case the continuity equation for each junction node and the energy conservation equations across the links attached to the node can be assembled into a much smaller system and solved iteratively (e.g., Zerihun et al., 2014). This approach requires the solution to be repeated sequentially for each set of link-node combination starting from one end

of the lateral and ending at the other end. Evidently, these two models are based on entirely different numerical methods. However, the fact that both approaches introduce minimal assumptions, in the formulation and solution of the steady-state lateral hydraulic problem, suggests that the outputs of the two models should be reasonably close. Thus a comparison of the two models can be used as an additional model evaluation criterion.

The main differences in problem formulation between the gradient and manifold methods are in the formulation of the sprinkler head-discharge relationship and in the calculation of junction node local head losses. With the manifold method sprinkler discharge is related to pressure head differential across the sprinkler, but with the gradient method sprinkler discharge is related to the total head differential across the sprinkler, i.e., including the velocity head upstream of sprinkler. Typically, sprinkler manufacturers provide head-discharge characteristics of sprinklers in terms of sprinkler pressure heads and discharges. Hence, the use of parameters, derived based on such data, in the context of a model that solves the lateral hydraulic problem with the gradient method involves a level of approximation. However, the pressure head is generally much larger than the velocity head, hence these differences should not have appreciable effects on the results. Furthermore, with the manifold method local head losses at junction nodes can be taken into account. However, the junction node head losses cannot be explicitly considered within the framework of the gradient method. Hence, in order to conduct an accurate comparison between the two models, in all the data sets used in the comparison, junction node local head losses are not considered. In addition, the model developed based on manifold hydraulics does not have a capability to take into account residual discharges at the downstream end of the lateral. Hence, versions of data sets 1 and 2 used here for model comparison have zero residual discharges at the downstream ends of the laterals.

Data sets 1 to 5 summarized in Table 9 are used in comparing the lateral hydraulic model, developed based on the gradient method, with that based on the manifold method. As noted in the preceding discussion, these data sets represent laterals that can be used in solid-set or set-move sprinkler systems and cover a wide range of geometric, slope, and hydraulic conditions (section 5.1).

5.3.2. Results of model comparison

The nodal pressure heads and sprinkler discharges along each of the laterals computed with the two models are depicted in Figures 9a-9e. Although a close look at the data shows that pressure head rises slightly in the downstream reaches of laterals 4 and 5, the dominant trend in

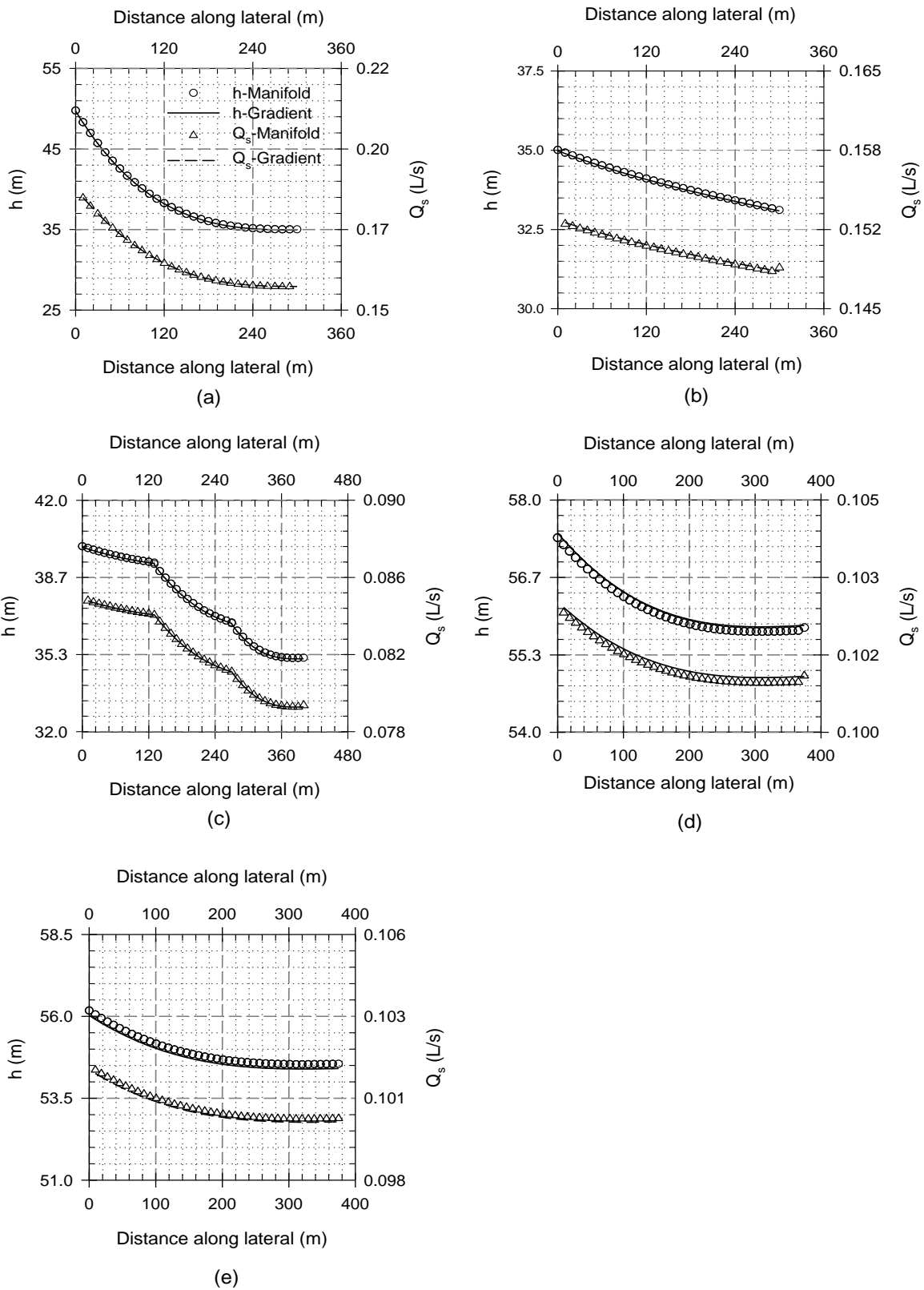


Figure 9. Comparison of lateral pressure heads, h , and sprinkler discharges, Q_s , computed with the lateral hydraulic simulation model, developed based on the gradient method, and that based on the manifold method: Data set 1, (b) Data set 2, (c) Data set 3, (d) Data set 4, and (e) Data set 5

all of the laterals is that the computed lateral pressure heads and sprinkler discharges decrease monotonically with distance. For data set 3 the pressure head and sprinkler discharge profiles have three distinct segments each with different slope and curvature. Note that these segments overlap with the three lateral segments that have different diameters, hence the observed pattern of variation in the pressure head and discharge profiles along the lateral is a function of the diameter of the lateral pipe segments. Overall, the results show that the lateral pressure heads, h , and sprinkler discharges, Q_s , computed with the gradient method closely matches those computed with the manifold method.

In order to obtain a quantitative measure of the differences between the predictions of the gradient and manifold methods, the differences in the lateral pressure heads and sprinkler discharges computed with the two models, expressed as percentage of those computed with the gradient method, were calculated. The resultant maximum, minimum, and average percent differences in lateral pressure heads and sprinkler discharges are depicted in Figures 10a and 10b. The maximum percent difference between the pressure heads computed with the gradient and manifold methods, δh , vary from 0.079% (data set 2) to 0.260% (data set 5) and the minimum range between 0.049 (data set 3) and 0.256% (data set 5), Figure 10a. The average percent difference in h varies between 0.077 for data sets 2 and 0.258 for data set 5. The maximum percent differences between the Q_s computed with the two models, δQ_s , vary from 0.099 (data set 3) to 0.255% (data set 1) and the minimum percent difference range between 0.006 (data set 3) and 0.102% (data set 5), Figure 10b. The average percent difference in Q_s range from 0.018 for data set 3 to 0.108% for data set 4. These results suggest that the outputs of the two models are essentially identical. The fact that the lateral pressure head and sprinkler discharges computed with the two models, which are based on entirely different numerical algorithms, are in good agreement suggests that the formulation and numerical solution of the lateral hydraulic simulation problem in both models is sound. Most importantly, these results lend support to the validity of the numerical algorithm implemented in the current model, which is by far the most complex of the two models compared here.

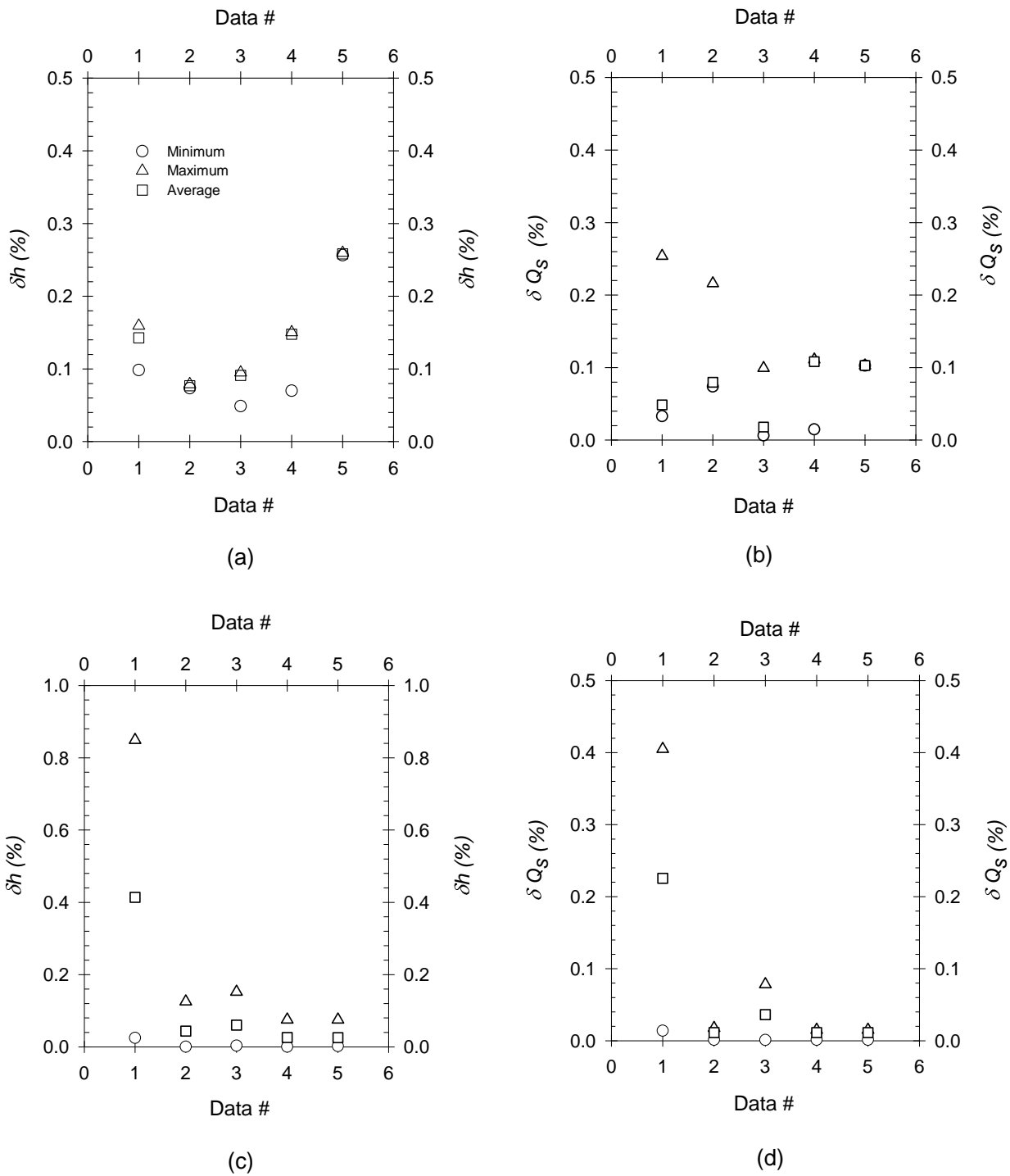


Figure 10. Graphs depicting comparisons of the lateral hydraulic simulation model, presented here, with a model based on manifold hydraulics and with EPANET: (a) Percent differences between lateral pressure heads computed with the gradient and manifold models, δh , (b) Percent differences between sprinkler discharges computed with the gradient and manifold models, δQ_s , (c) Percent differences between lateral pressure heads computed with the lateral hydraulic simulation model and EPANET, δh , and (d) Percent differences between sprinkler discharges computed with the lateral hydraulic simulation model and EPANET, δQ_s .

5.4. Comparison of the lateral hydraulic model with EPANET

5.2.1. Introductory discussion

EPANET is a computer program designed to simulate the hydraulic and water quality characteristics of pressurized hydraulic networks (Rossman, 2000). The lateral hydraulic model, developed here, and the hydraulic modeling functionality of EPANET are both based on a numerical solution of a system of (energy conservation and continuity) equations describing the steady-state flow processes in a pipeline network. Although EPANET is primarily developed for analyses of flow and constituent transport and transformation processes in large-scale water distribution networks with complex topologies, it can also be used to simulate the hydraulics of irrigation laterals with multiple outlets and pressure dependent discharges. Thus comparisons of the outputs of the lateral hydraulic model and EPANET can be used for further validation of the lateral hydraulic model.

Considering the formulation of the lateral hydraulic simulation problem, the main difference between the lateral hydraulic model and EPANET are the formulas used to calculate the friction factor of the Darcy-Weisbach equation. For the case in which flow is laminar ($Re \leq 2000$), both models use Eq. 5. For $4000 < Re$, the model developed here uses the Colebrook-White equation, Eq. 6, to compute the friction factor iteratively and EPANET uses the Swamee and Jain equation (e.g., Rossman, 2000), which expresses the friction factor as an explicit function of pipe relative roughness, pipe diameter, and Re . In the interval $2000 < Re \leq 4000$, EPANET uses a cubic interpolation scheme to estimate the friction factor from the Moody Diagram (Dunlop, 1991). The current model, however, approximates the friction factor by simply extending Eq. 5 over the interval $2000 < Re \leq 4000$. The effects of these differences on the computed friction factors, f , friction head losses, h_f , and lateral pressure heads, h , will be discussed in the next section.

Data sets 1 to 5 presented in Table 9 are used in comparing the lateral hydraulic simulation model with EPANET. As noted in the preceding discussion, these data sets represent laterals that can be used in solid-set or set-move sprinkler systems and cover a wide range of geometric, slope, and hydraulic conditions (section 5.1). Both EPANET and the current model can simulate the hydraulics of laterals with residual outflow at the downstream end. Hence, data sets 1 and 2 used here has residual outflows as indicated in Table 9. Furthermore, EPANET treats emitters as properties of the pipe they are placed on. Hence in order to have a more accurate comparison of the two models, versions of data sets 1 to 5 in which sprinklers are

placed directly on the lateral (i.e., the riser pipe height is set to zero) are used in comparing the two model. Note that the treatment of lateral residual discharges and riser pipes in the current analysis is different from that envisaged in the comparison of the lateral hydraulic model with that based on manifold hydraulics (section 5.3). Thus comparison of the results presented in the following sections with those in section 5.3 needs to take these differences into consideration.

5.4.2. Results of model comparison

The lateral pressure head and sprinkler discharge profiles, computed with the two models, are depicted in Figures 11a-11e. Although a close look at the data shows that pressure head rises slightly in the downstream reaches of laterals 4 and 5, the dominant trend in all of the laterals is that the computed pressure heads and sprinkler discharges decrease with distance from lateral inlet. Overall, the results show that lateral pressure head, h , and sprinkler discharge, Q_s , computed with the lateral hydraulic model closely matches those computed with EPANET.

In order to obtain a quantitative measure of the differences between the predictions of the lateral hydraulic model and EPANET, the differences in the lateral pressure heads and sprinkler discharges computed with the two models, expressed as percentage of those computed with the lateral hydraulic simulation model, were calculated. The resultant maximum, minimum, and average percent differences in lateral pressure heads and sprinkler discharges are depicted in Figures 10c and 10d. The maximum percent difference between the pressure heads computed with the current model and EPANET, δh , vary from 0.075% (data sets 4 and 5) to 0.849% (data set 1) and the minimum ranges between 0.0% (data sets 2 and 4) and 0.025% (data sets 1), Figure 10c. The average percent differences in h vary between 0.026 for data sets 4 and 5 and 0.414 for data set 1. The maximum percent differences between the Q_s computed with the two models, δQ_s , vary from 0.015 (data sets 4 and 5) to 0.405% (data set 1) and the minimum percent difference ranges between 0.001% (data sets 2 to 5) and 0.014% (data set 1), Figure 10d. The average percent difference in Q_s ranges from 0.011% (data sets 4 and 5) to 0.225% (data set 1). These results suggest that the outputs of the two models are essentially identical. The fact that the lateral pressure head and sprinkler discharges computed with the two models are very close lends further support to the validity of the numerical algorithm implemented in the lateral hydraulic simulation model.

Note that the average and maximum percent differences in pressure head and sprinkler discharges for data set 1 differ appreciably from those calculated for the rest of the data sets (Figures 10c and 10d). A close look at the data shows that the friction head loss over the length

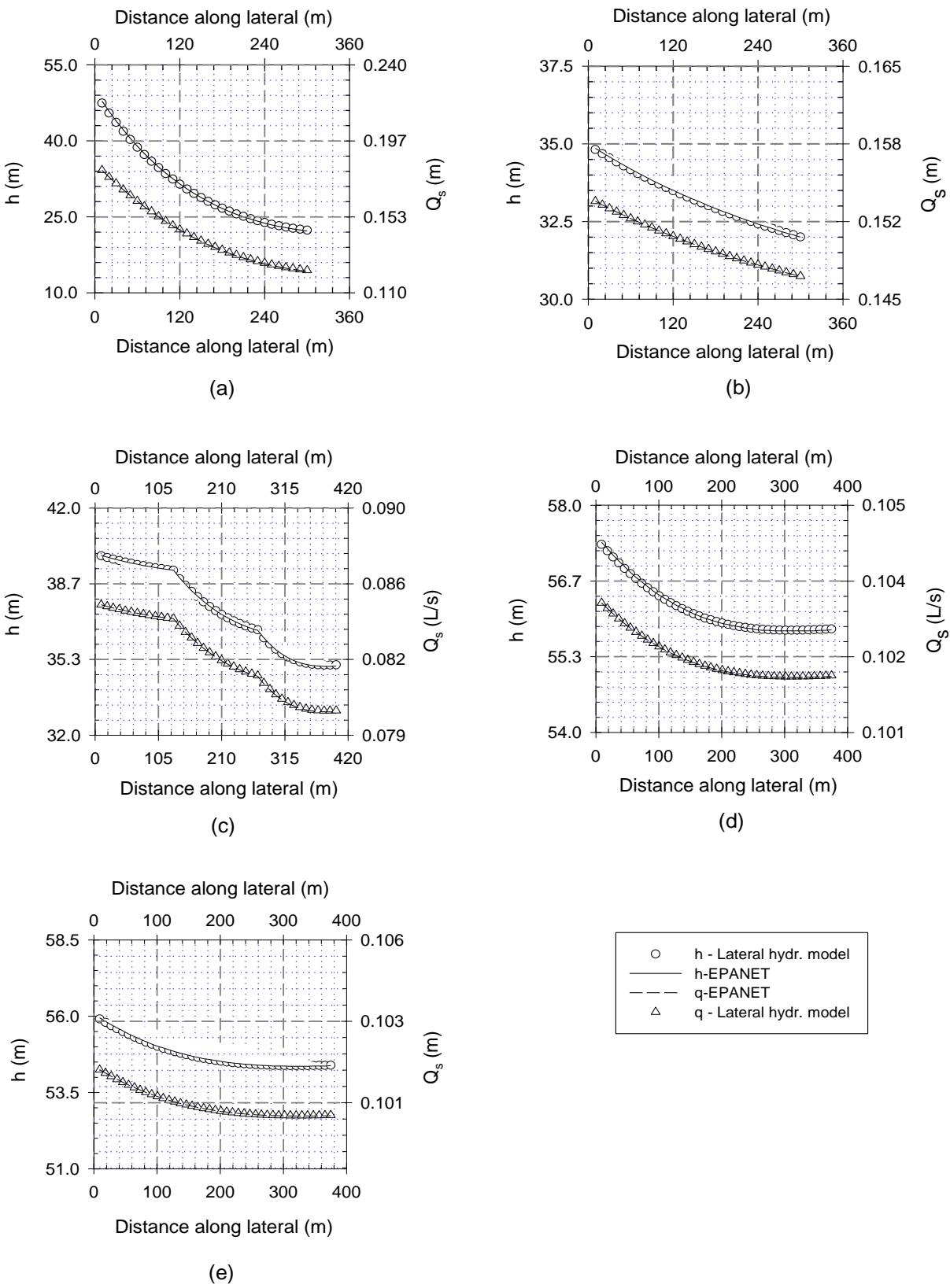


Figure 11. Comparison of lateral pressure heads, h , and sprinkler discharges, Q_s , computed with the lateral hydraulic simulation model and EPANET: (a) Data set 1, (b) Data set 2, (c) Data set 3, (d) Data set 4, and (e) Data set 5

of lateral 1 is about 27.6m, which is more than six times as large as the second largest friction head loss, occurring in lateral 3. More significantly, however, it can be observed that the friction head loss in lateral 1 is of comparable scale as the lateral pressure head, which vary between about 22.4 and 47.5m. Evidently this result implies that the effect of friction head loss on lateral pressure head, and hence on sprinkler discharge, profiles is more significant in data set 1 than is the case in the other laterals. While this observation suggests that the relatively larger friction head loss in data set 1 may have an effect on the percent differences in pressure head, and hence sprinkler discharge, the actual mechanism by which the effect of the larger h_f translates into the relatively larger percent differences in h and Q_s is not clear to the authors.

As noted above, considering the formulation of the lateral hydraulic simulation problem, the main difference between the two models compared here relates to the formulas used to calculate the Darcy-Weisbach friction factor. Evidently, the results summarized above suggest that the effect of these differences on lateral hydraulics is negligible. However, in the following sections estimates of f , and the resultant friction head loss, h_f , obtained with the two approaches, are compared in order to directly evaluate the differences in the estimates of these parameters. Accordingly, the difference between a parameter estimate (e.g., estimate of a lateral pipe segment f) computed with EPANET and the current model, expressed as percent of the parameter estimate computed with the current model, is used here for comparison purposes.

For turbulent flow conditions ($4000 < R_e$)

Turbulent flow occurs over 95.0% of the length of each of the laterals considered in the current analysis. Thus it is the dominant flow condition in these laterals and as such it is far more important, than both laminar and critical flow conditions, in terms of its significance in the overall lateral-wide comparison of estimates of f and h_f obtained with the two models.

Considering all the laterals, the minimum percent difference between estimates of (lateral pipe segment) friction factor, f , computed with EPANET and the lateral hydraulic model is 0.58% and the corresponding minimum percent difference in h_f is 0.61%. The maximum percent differences in f and h_f are 1.78% and 1.65%, respectively. The overall average percent difference in f is 0.89%, compared to a percent difference of 0.82% in h_f . Note that the percent differences calculated for both f and h_f are sufficiently small for the estimates of f and h_f , computed with the two models, to be considered in good agreement.

A close look at the data shows that the minimum percent differences in f and h_f , given above, correspond to the percent differences in f and h_f calculated for the penultimate segment of

the lateral in data set 2. Furthermore, the maximum percent differences in f and h_f , noted above, correspond to the percent differences in f and h_f calculated for the penultimate segment of the lateral in data set 3. Now if all the parameters of a lateral pipe segment in the Darcy-Weisbach equation, except the friction factor, are kept constant, then the relationship between f and h_f becomes linear. In which case, for a given lateral segment, the percent differences in f and, the corresponding, h_f should be equal. In contrast to this observation, however, the result summarized above show that the minimum percent difference calculated for f is slightly at variance with that calculated for the corresponding h_f and the same is true for the maximum percent differences calculated for f and h_f . The question, therefore, is what is the reason for the observed slight variance between the percent differences in (lateral segment) f and h_f , given above?

The explanation for the preceding observation lies in the fact that the lateral pipe section discharge, Q , is not a given quantity but instead it is computed iteratively along with f and h_f . Evidently both f and h_f are functions of the lateral discharge. However, the fact that lateral discharge itself is computed iteratively meant that Q in turn is a function of h_f , and in effect f . The implication is that the differences in the formulas, used for computing f in EPANET and the lateral hydraulic simulation model, not only affect the values of f , and hence h_f , but also has some effect on the corresponding Q . In addition, the numerical errors introduced in the computation of Q will not be exactly the same in the two models. Thus the minimum and maximum percent differences summarized above represent not only the effect of the alternative formulas on f , but also on Q and possibly the effect of differences in the numerical errors associated with the computation of Q . It then follows that the percent differences in f and h_f , calculated for a given lateral segment, need not be equal. It should, nonetheless, be pointed out that a close look at the data shows that these effects are significant only in laterals where friction head loss is relatively large.

For flow in the critical range ($2000 < R_e \leq 4000$)

For the laterals considered here, critical flow occurs in the downstream end lateral segment of data set 3 and in the penultimate segment of data sets 4 and 5. The percent differences in f , calculated for these lateral segments are 21.8% for data set 3 and 95.7% for data set 4. The percent differences in h_f are 21.6% and 95.7% for data sets 3 and 4, respectively. As noted above, in this range of R_e entirely different formulas are used to estimate the friction factor in EPANET and the lateral hydraulic simulation model and to a significant extent this difference

explains the rather large variance between the estimates of f , and hence h_f , computed with the two models. Remarkably, however, the significant percent difference in the h_f , computed with the two models, did not lead to perceptible differences in pressure heads and hence sprinkler discharges (Figures 10c and 10d and 11a-11e). Note that the reason for this is directly related to the magnitude of the friction head loss in the lateral segments where this flow regime occurs. A close look at the data shows that flow rates in the distal segment of lateral 3 and the penultimate segment of lateral 4 are very small, about 0.08L/s and 0.203L/s, respectively. As a result the corresponding friction head losses are negligibly small, about 2mm and 0.5mm for data sets 3 and 4, respectively. Therefore, in absolute terms, the differences between the friction head losses, computed with the two models, are too small to have perceptible effects on the corresponding pressure heads and hence their differences.

Note that for each lateral segment the percent differences in h_f are about the same as that calculated for f . As can be recalled from a discussion in the preceding section, this may possibly be related to the very small friction head loss in the lateral segments where this flow condition occurs.

For laminar flow ($Re \leq 2000$)

Laminar flow occurs in the downstream end segments of the laterals of data sets 4 and 5. The percent differences between the f values computed, with EPANET and the current model, are 1.8% and 3.2% for data sets 4 and 5, respectively. The percent differences between the friction head losses computed with the two models are as well 1.8% (for data set 4) and 3.2% (for data set 5). Given that the two models use exactly the same formula, Eq. 5, to calculate the friction factor in the laminar range, the f estimates within these Re range should in theory have shown the closest agreement compared to the other flow regimes, discussed in the preceding sections. However, the percent differences for the laminar range are greater than the maximum percent difference computed for the turbulent transition and fully turbulent rough zones ($4000 < Re$). A possible explanation for this is that, for both data sets 4 and 5, the pipe segments in which laminar flow occurs are located at the distal end of the laterals and immediately downstream of the pipe segments where the flow regime is critical ($2000 < Re \leq 4000$). Note that this is the pipe segment where the friction factor and friction head loss computed with the two models show the largest relative difference, as high as 95.7%. It is therefore conceivable that these differences may have contributed to the larger than expected percent difference in the computed f and h_f in the pipe segment downstream (where flow is laminar).

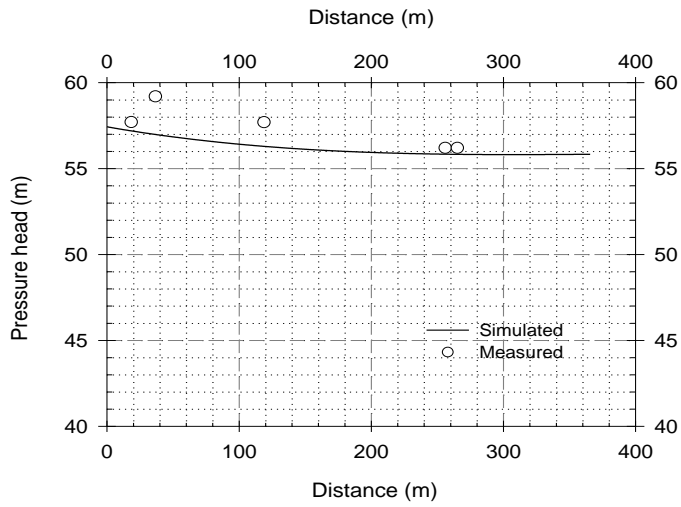
Furthermore, the friction head loss, h_f , computed for the downstream end segments of laterals 4 and 5 are in absolute terms very small: in the order of a tenth of a millimeter. As a result the friction head loss has no perceptible effect on the pressure heads and hence sprinkler discharges computed with the two models (Figures 10c-10d and 11a-11e). Note that for each lateral segment the percent differences in h_f and f are equal. This may possibly be related to the very small friction head loss in the lateral segments where flow is laminar.

5.5. Model evaluation with measured data

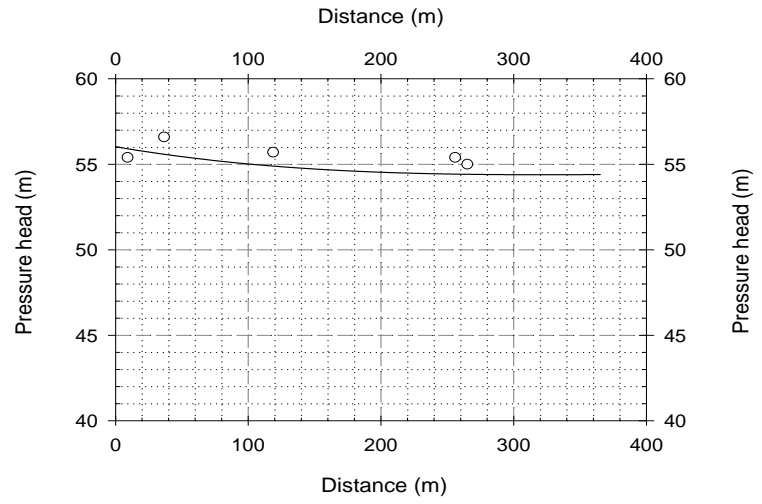
Additional evaluation of the model developed in the current study is conducted based on comparison of its output with pressure head profiles measured along four laterals in a field-scale solid-set sprinkler system (Zerihun et al., 2011). Pertinent hydraulic, geometric, and slope data used in model comparison are summarized in Table 9 (data sets 4 to 7). Comparisons of the measured and simulated pressure heads along the laterals are shown in Figures 12a-12d. In order to provide a quantitative measure of the model prediction error, for each data set the differences between the simulated and measured pressure heads, expressed as a percentage of the measurements, were calculated.

The minimum, maximum, and average percent differences between the simulated and measured pressure heads are shown in Figure 13. For data set 4, the percent differences in lateral pressure heads range between a minimum of 0.6 and a maximum of 3.7%, with an average of 1.6%. The minimum, maximum, and average percent differences for data set 5 are 0.7, 3.6, and 1.6%, respectively. For data set 6, the percent differences between measured and computed pressure heads vary from 0.2 to 3.8% and the average is 1.8%. For data set 7, the minimum, maximum, and average percent differences are 0.9, 1.8, and 1.4%, respectively.

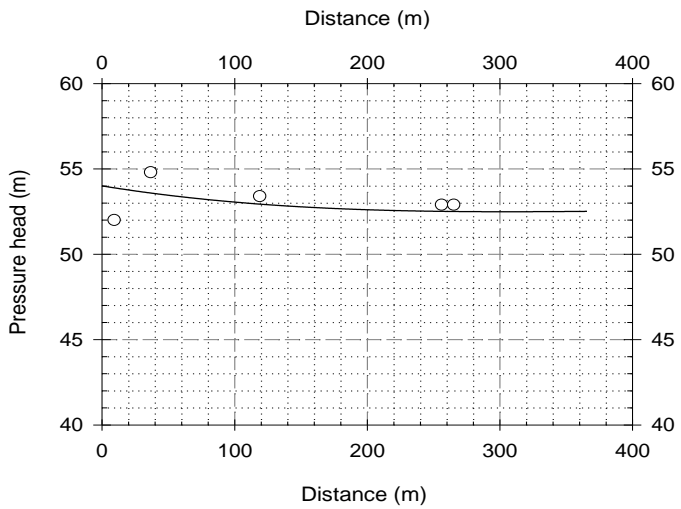
Considering all the data sets, the overall average percent difference between the measured and computed lateral pressure head profiles is 1.6%. The model prediction error for all the data sets is sufficiently low for the simulated pressured head profiles to be considered as reasonably close matches to the measured data.



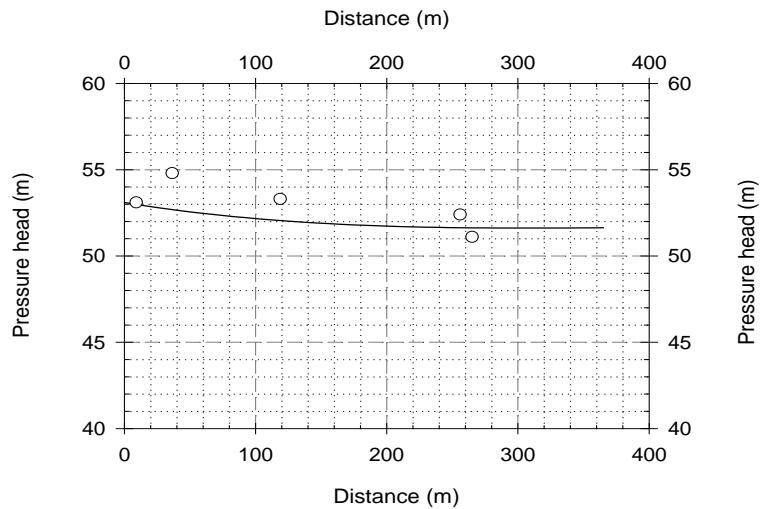
(a)



(b)



(c)



(d)

Figure 12. Comparison of lateral pressure head computed with the lateral hydraulic simulation model, presented here, and measured data: (a) Data set 4, (b) Data set 5, (c) Data set 6, and (d) Data set 7

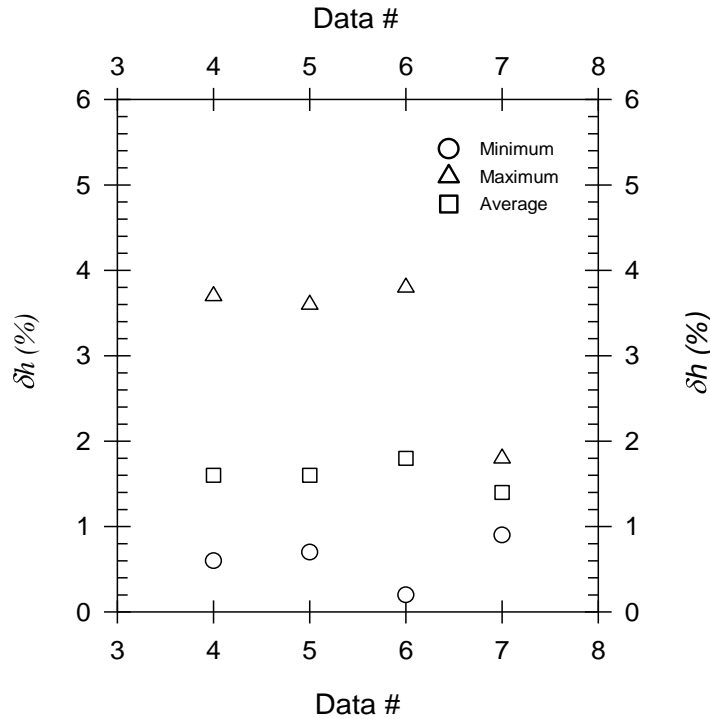


Figure 13. Percent differences between field measured lateral pressure head profiles and those computed with the lateral hydraulic simulation model, δh , expressed as a percentage of measurements

5.6. Sensitivity analysis

5.6.1. Introductory discussion

Sensitivity analysis is conducted in order to further evaluate spatial patterns of model predicted lateral hydraulic characteristics under a range of conditions. A one-dimensional analysis is used to evaluate the sensitivity of lateral pressure head and sprinkler discharge profiles to variations in lateral slope, diameter, and pipe absolute roughness over reasonably large intervals. A one-dimensional sensitivity analysis consists of a procedure in which at any one time only the lateral slope, or diameter, or absolute roughness is varied within a preset range, while all other variables and parameters are kept constant at their field measured values. The analysis is based on data set 4, a field measured data presented in Table 9. It is assumed here that lateral slope, diameter, and pipe absolute roughness are constant over the length of the lateral.

Note that instead of the head differential across a sprinkler (i.e., the difference between total residual head upstream of a sprinkler and sprinkler elevation, $H-Z$), which is directly

proportional to sprinkler discharge, it is the lateral pressure head, h , along with sprinkler discharge that is used in the current analyses. Lateral pressure head is used, because it is less of an abstract quantity, compared to head differential across a sprinkler, and it is more amenable to theoretical analyses that help verify some of the observations that would be deduced based on simulated data. However, it is important to note that since h is only an approximation to $H-Z$, the simulated location of the minimum pressure head and the minimum sprinkler discharge along a lateral may not necessarily be the same, but should be close.

5.6.2. Lateral slope

Hydraulic simulations were conducted, with the gradient model, to evaluate the sensitivity of lateral pressure head profile and sprinkler discharges to variations in lateral slope. Five different lateral slopes ranging between -0.5% to 0.25% were used in the analyses. Simulated lateral pressure head and sprinkler discharge profiles, expressed as a function of lateral slopes, are depicted in Figures 14a and 14b, respectively.

Sensitivity of pressure head profile to lateral slope

Considering the upper limit of the slope range (0.25%), it can be observed that the pressure head profile (Figure 14a) decreases monotonically with distance from a maximum pressure head of 57.44m at the inlet to a minimum of 54.7m at the distal end of the lateral. The same general spatial pattern holds for the pressure head profile along the lateral with 0.0% slope as well.

By contrast, the laterals with negative slopes have a distinct trend in which pressure head decreases with distance from the lateral inlet, reaches a minimum somewhere along the lateral, and then begins to increase, rising to a local peak at the distal end of the lateral. For instance, for the lateral with a slope of -0.06%, pressure head decreases monotonically with distance from a maximum value of 57.44m, at the inlet, to a minimum of about 55.82m at a distance of 310.8m from the inlet. It then increases slightly to about 55.84m at the downstream end of the later (Figure 14a). A similar trend can be noted for the lateral with -0.25% and -0.5% slope. However, as the lateral slope is varied from -0.06, to -0.25, and then to -0.5%, the point at which the minimum pressure head occurs moves further upstream along the lateral, the corresponding minimum pressure head increases, and the magnitude of the pressure head rise in the lateral segment downstream, of the minimum point, becomes larger. For example, for the lateral

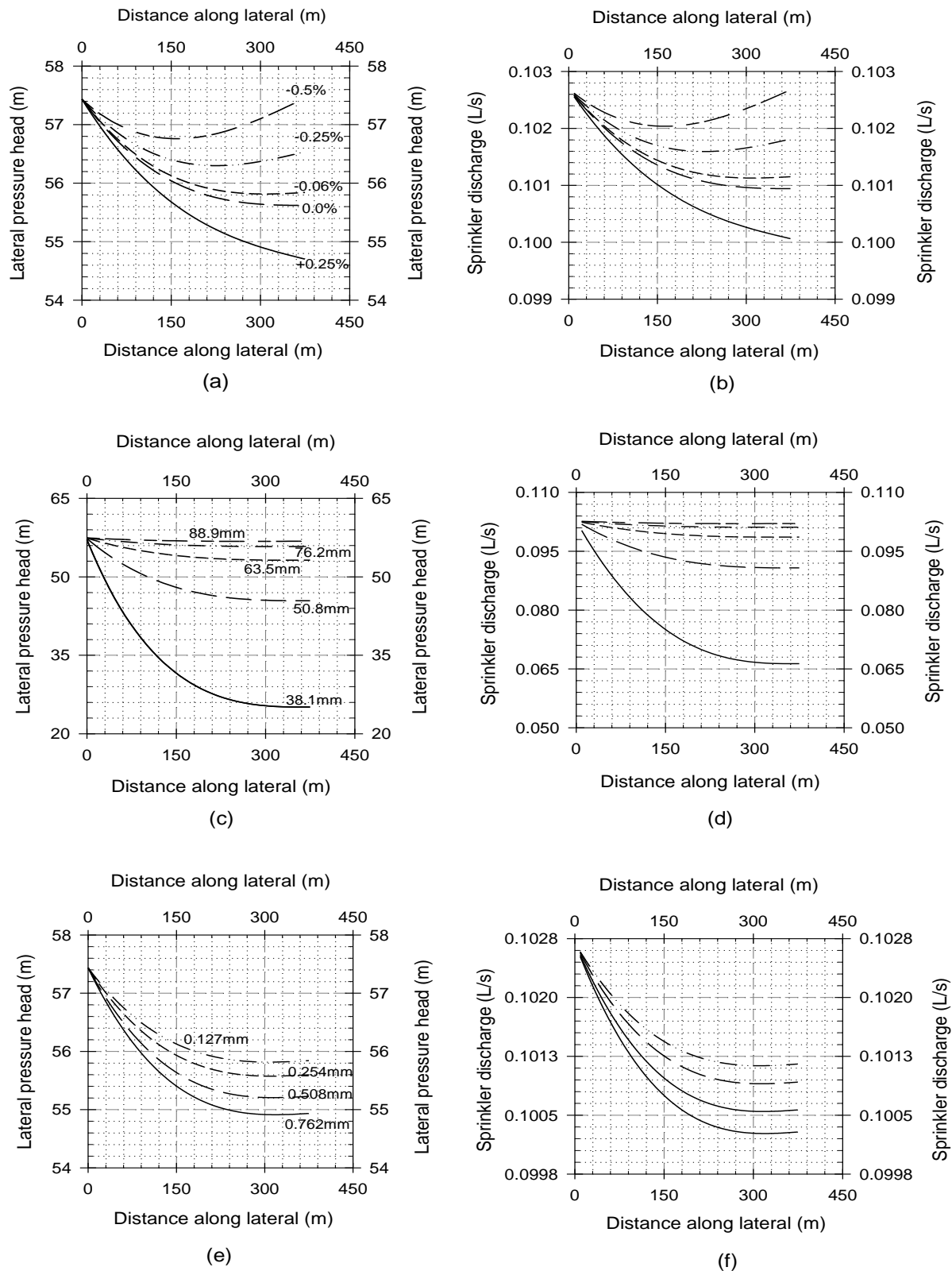


Figure 14. Sensitivity of (a) Lateral pressure head to lateral slope, (b) Sprinkler discharge to lateral slope, (c) Lateral pressure head to diameter, (d) Sprinkler discharge to diameter, (e) Lateral pressure head to pipe absolute roughness, and (f) Sprinkler discharge to pipe absolute roughness

with -0.5% slope, the minimum pressure head is 56.76m, exceeding the minimum pressure head associated with -0.06% slope by about 0.94m. Furthermore, the minimum pressure for this lateral occurs at a distance of about 155.4m from the inlet, compared to a distance of 310.8m from inlet for the lateral with -0.06 slope. In addition, for the lateral with -0.5% slope, the pressure head profile increases from a minimum of 56.76m to a local peak of about 57.46m at the distal end of the lateral, which represents an increment of 0.7m. By contrast, for the lateral with -0.06% slope, the pressure head profile in the downstream reach of the lateral rose by a mere 2cm from the corresponding minimum of 55.82m.

The validity of the broad spatial trends of the lateral pressure head profiles, described above, can be evaluated by analyzing the functional relationship between lateral pressure head profile, $h(x)$, friction head loss, $h_f(x)$, velocity head, $V_h(x)$, elevation profile, $Z(x)$, and total head at the lateral inlet, H_0 , where x is distance from inlet. Such analysis is presented in Appendix VII. Overall, the analysis shows that the general spatial behavior of $h(x)$ (i.e., whether it is increasing or decreasing over the entire length of the lateral or it is increasing over a segment of the lateral and is decreasing over another) depends on the magnitude of the lateral slope, S_0 , relative to that of the friction slope, $h_f'(x)$. A detailed discussion on this is presented in Appendix VII, however, the key results are summarized here:

- (i) If $0 \leq S_0$, then $h(x)$ is a decreasing function of distance from inlet over the entire length of the lateral;
- (ii) If $S_0 < 0$, but $h_f'(0) \leq |S_0|$, then $h(x)$ is an increasing function of distance over the entire length of the lateral;
- (iii) If $S_0 < 0$ and $|S_0| < h_f'(0)$, but $|S_0|$ is sufficiently large to exceed $h_f'(x)$ at some point along the lateral, then $h(x)$ decreases with distance from inlet, reaches a minimum at some point along a lateral, where $h_f'(x) = |S_0|$, and then increases to a local peak at the distal end of the lateral; and
- (iv) If $S_0 < 0$ and $|S_0| < h_f'(x)$ over the entire length of the lateral or $|S_0| = h_f'(L)$, (where L is the lateral length), then $h(x)$ is a decreasing function of distance, from the inlet, over the entire length of the lateral;

As can be noted from Appendix VII, for scenarios *i* and *iv*, above, the maximum and minimum pressure heads occur at the upstream and downstream ends of the lateral, respectively. For

scenario *ii*, the minimum and maximum pressure heads are located at the inlet and distal ends of the lateral, respectively. For scenario *iii*, however, the minimum pressure head occurs at a point along the lateral, where the friction slope is equal to the lateral slope. The maximum pressure head can occur at the inlet or distal end of the lateral depending on the magnitude of S_0 relative to that of $h_f'(x)$.

Note that the spatial trends of the lateral pressure head profiles presented in Figure 14a for all the five lateral slopes are consistent with the inferences deduced in Appendix VII, based on hydraulic theory, and summarized in scenarios *i-iv*, above. For the laterals with +0.25 and 0.0% slopes, the spatial patterns of the simulated pressure head profiles with respect to distance and the location of the maximum and minimum pressure heads along the lateral are consistent with the description given in scenario *i* above for laterals with $S_0 \geq 0$. Likewise, for the laterals with slopes ranging between -0.06 and -0.5% (i.e., $S_0 < 0$), the spatial pattern of the simulated pressure head profiles fall into the category described in scenario *iii* above, where $|S_0| < h_f'(0)$, but that $|S_0|$ is sufficiently large to exceed $h_f'(x)$ at some point along the lateral.

Sensitivity of sprinkler discharge profile to lateral slope

The sensitivity of sprinkler discharge profile to lateral slopes is depicted in Figure 14b. Considering the upper bound of the slope range (0.25), it can be observed that the sprinkler discharge monotonically decreases from a maximum of 0.1026L/s at the lateral inlet to a minimum of about 0.1L/s at the distal end of the lateral. The lateral with 0.0% slope has the same general spatial pattern as the lateral with 0.25% slope. By contrast, the sprinkler discharge profiles of the laterals with negative slopes have two segments with distinctly different spatial patterns: an upstream section in which sprinkler discharge decreases monotonically with distance from a maximum value at the upstream end sprinkler to a minimum somewhere along the lateral, followed by a downstream segment in which discharge profile increases with distance, reaching a local peak at the distal end of the lateral. For example, for the lateral with a slope of -0.5%, the sprinkler discharge decreases from a maximum of 0.1026L/s, for the upstream end sprinkler, to a minimum of about 0.1020L/s at about 164.5m from the inlet. The sprinkler discharge then increases with distance to about 0.1027L/s at the distal end of the lateral.

Overall, it can be observed from Figures 14a and 14b that the pattern of variation of the sprinkler discharge profiles, as a function of lateral slope, is about the same as that observed in

relation to the corresponding lateral pressure head profiles. Note that the similarity in the spatial patterns of the lateral pressure head and sprinkler discharge profiles can be explained by the fact that sprinkler discharges are closely related to local lateral pressure heads.

5.6.3. Lateral diameter

The sensitivity of lateral pressure head profile and sprinkler discharges to variations in lateral diameter was evaluated for five standard pipe diameters ranging between 38.1 and 88.9mm. The resultant pressure head and sprinkler discharge profiles along the lateral are depicted in Figures 14c and 14d, respectively.

Sensitivity of lateral pressure head to diameter

Figure 14c depicts the sensitivity of lateral pressure heads to variations in lateral diameter. Considering the lateral with the smallest diameter (38.1mm), it can be observed that pressure head vary monotonically with distance from a maximum of 57.1m at the inlet to a minimum of 25.1m at the distal end of the lateral, which represents a decrement of 32.0m over the length of the lateral. By comparison, for the largest diameter lateral considered here (88.9mm), pressure head decreases from a maximum of 57.45m at the lateral inlet to a minimum of 56.79m at a distance of about 274.2m from the inlet, representing a decrement of only 0.66m. Pressure head then increases slightly, reaching 56.83m at the distal end of the lateral.

A close look at the simulated data shows that the relatively large pressure loss in small diameter laterals is directly related to the relationship between pipe diameter and friction head loss. For instance, the friction head loss in a lateral with 38.1mm diameter is 32.6m, which exceeds the elevation differential along the lateral, of 0.22m, by an order of magnitude and a half (note that elevation differential is the other important factor that affects pressure head profile). By comparison, for the largest diameter lateral considered here, 88.9mm, the friction head loss is 0.87m, which is only about four times as large as the drop in elevation over the length of the lateral. Evidently these results and physical reasoning suggest that friction head loss is the dominant factor in determining the pressure head profile in smaller diameter laterals (38.1 and 50.8mm), and as such it is the source of the relatively large pressure head loss observed in these laterals. Further examination of the data shows that the pressure head loss, along a lateral, decreases rapidly with increases in pipe diameter from 38.1 to 88.9mm. Given that friction head loss is inversely proportional to a power function of pipe diameter, it can be readily observed that these results are consistent with hydraulic theory.

We will now briefly examine the interactive effects of lateral diameter and slope on lateral pressure head. For the smallest diameter lateral considered here, 38.1mm, the simulated data shows that the pressure head profiles monotonically decrease with distance from a maximum at the inlet to a minimum pressure head at the downstream end of the lateral (Figure 14c). A close look at the data shows that the friction slope at the downstream end of the lateral, $h_f'(L)$, equals $|S_0|$, but $h_f'(x)$ exceeds $|S_0|$ for $x < L$, leading to a pressure head profile that is monotonically decreasing with distance from inlet over the entire length of the lateral. Note that the spatial pattern of the pressure head profile for these laterals is one described by scenario *IId* (Appendix VII).

By contrast, for each of the laterals with diameter ranging between 50.8 and 88.9mm, the pressure head profile decreases monotonically with distance from a maximum at the inlet to a minimum value located somewhere along the lateral and then increases reaching a local peak at the distal end of the lateral. Overall, the simulated data shows that as lateral diameter increases from 50.8, to 63.5, 76.2, and then to 88.9mm, the minimum pressure head as well increases and the point at which the minimum pressure head occurs moves upstream along the lateral. Evidently the spatial patterns of the pressure head profiles for these laterals fall into the category described by scenario *IIf* and Eq. VII.11 (Appendix VII).

Note that the category for the spatial patterns of lateral pressure head profiles transitioned from scenario *IId* (for the lateral with a diameter of 38.1mm) to scenario *IIf* (for diameters ranging from 50.8 to 88.9mm). This implies that the significance of the effect of lateral slope on pressure head profile, relative to that of friction, increases with lateral diameter. Given that friction head loss decreases exponentially with increases in lateral diameter, the relatively rapid decrease in the significance of its effect on pressure head (compared to that of lateral slope) with increases in lateral diameter is consistent with hydraulic theory.

Sensitivity of sprinkler discharge profile to diameter

The sensitivity of the sprinkler discharge profiles to variations in lateral diameter are shown in Figure 14d. Considering the lateral with the smallest diameter, 38.1mm, the simulated data shows that sprinkler discharge decreases monotonically with distance from a maximum of about 0.1003L/s at the upstream end sprinkler to a minimum of 0.0663L/s at the distal end of the lateral. By comparison, for the largest diameter considered in the current analyses (88.9mm), the sprinkler discharge profile has an upstream segment that decreases with distance from a

maximum of about 0.1026L/s at the upstream end sprinkler, reaching a minimum of 0.1021L/s at a distance of about 274.2m from the inlet and then increase with distance. Nonetheless, the increase in discharge over the downstream reach of the lateral is practically negligible, i.e., less than the significant digit considered here. The simulated data, for lateral diameters in the range 50.8 and 76.2mm, show that the spatial trends of the corresponding sprinkler discharge profiles follow about the same overall pattern as that obtained for 88.9mm. Furthermore, the data also show that as lateral diameter increases, the minimum sprinkler discharge as well increases and the point of minimum sprinkler discharge moves upstream along the lateral.

Evidently the pattern of variation of sprinkler discharge profiles, as a function of lateral diameters, are about the same as that observed in relation to the corresponding pressure head profiles (Figure 14c). These similarities in the spatial patterns of the lateral pressure head and sprinkler discharge profiles can be explained by the fact that sprinkler discharges are closely related to local lateral pressure heads.

5.6.4. Lateral pipe absolute roughness

The sensitivity of lateral pressure head profile and sprinkler discharges to variations in lateral pipe absolute roughness was evaluated for roughness values ranging between 0.127mm (recommended for aluminum pipes; Keller and Bliesner, 1990) and 0.762mm. The corresponding lateral pressure head and sprinkler discharge profiles are summarized in Figures 14e and 14f, respectively.

Sensitivity of lateral pressure head profile to pipe absolute roughness

Simulated lateral pressure head profiles as a function of pipe absolute roughness are depicted in Figure 14e. For a roughness value of 0.127mm, lateral pressure head decreases from a maximum of 57.44m at the inlet end to a minimum of about 55.82m at a distance of 310.8m from inlet and then, because of slope effects, pressure head rises slightly to 55.84m at the distal end of the lateral. As the pipe absolute roughness is increased to 0.254, then to 0.508, and 0.762mm the maximum pressure head at the lateral inlet remains the same as that obtained for absolute roughness of 0.127mm. However, the pressure head profile and the minimum pressure head decline slightly with increases in pipe absolute roughness. For instance for the maximum pipe absolute roughness considered here (0.762mm), the minimum pressure head is about 54.91m, relative to the 55.82m associated with the lateral pipe roughness of 0.127mm. The minimum pressure head point, for a roughness value of 0.762mm, moved slightly downstream to

319.9m, compared to the 310.8m for absolute roughness of 0.127mm. In the lateral section between 319.9 and 374.4m, the pressure head profile (for pipe roughness of 0.762mm) rose marginally with distance reaching a local peak of 54.93m at the downstream end of the lateral. A comparable rise in pressure head can be noted over the downstream reach of the lateral with absolute roughness of 0.127mm.

Outputs of the hydraulic simulation summarized above show that increases in pipe absolute roughness led to decreases in the lateral pressure head profile and to a marginal increase in the distance of the minimum pressure head point from lateral inlet. Evidently, pipe absolute roughness affects lateral pressure head profile through its effect on friction head loss. In the analysis presented here it is assumed that all (lateral hydraulic, geometric, and slope) variables/parameters are constant, except pipe absolute roughness. However, lateral discharge is not an input to the model and it varies with pipe absolute roughness. In fact a close look at the energy conservation and the Darcy-Weisbach friction head loss equations suggest that the change in friction head loss resulting from an increase in pipe absolute roughness represents the net effect of a rather complex interaction between pipe absolute roughness and lateral discharge. Note that, at least in theory, this may complicate any analysis regarding the relationship between pipe roughness and friction head loss, and hence pressure head. Nonetheless, the simulated output shows that, for the data considered here lateral discharge is nearly insensitive to pipe absolute roughness (may note related discussion in subsequent section). Thus we assume here that the effect of variations in lateral discharge (due to changes in pipe absolute roughness) on friction head loss is practically negligible.

Under the hydraulic scenario considered here lateral diameter is assumed constant, hence increases in pipe absolute roughness would lead to increases in relative roughness. Given that lateral discharges are nearly constant, it can then be observed from Moody Diagram that increases in lateral pipe relative roughness will result in increases in the friction factor, f , and hence to increases in friction head loss, h_f . Based on the equations presented in Appendix VII, it is therefore a simple matter to show that increases in h_f (due to increases in pipe absolute roughness) would lead to decreases in lateral pressure head profile. Furthermore, under the scenario considered here, it can readily be shown that increases in h_f imply increases in friction slope, h_f' , as well. As can be noted from the discussion in Appendix VII, for a lateral with a constant slope this should result in pressure head profiles in which the minimum pressure head point shift downstream along the lateral.

The model computed friction head loss and friction slope data support the hydraulic reasoning outlined above to explain the observed spatial pattern of the simulated pressure head profile. The lateral friction head loss for pipe absolute roughness of 0.762mm is 2.77m, which is significantly greater than an h_f of 1.86m associated with pipe roughness of 0.127mm. Given that the lateral slope is constant, it can be shown based on the results presented in Appendix VII that the larger friction head loss associated with an absolute roughness of 0.762mm will lead to a lower pressure head profile compared to that associated with roughness of 0.127mm.

Furthermore, the simulated data show that h_f' for pipe absolute roughness of 0.762 and 0.127mm decreases with distance starting from maximum values of 0.021 and 0.014, respectively, at the inlet end. Note that this is consistent with the general spatial behavior of lateral friction slope (Appendix VII). The data also show that, except for the distal lateral segment, the h_f' curve for absolute roughness of 0.762mm is above the friction slope curve for pipe roughness of 0.127mm. However, the h_f' function for roughness of 0.762mm also decreases at a faster pace, with distance from lateral inlet, compared to the h_f' curve associated with roughness value of 0.127mm, but the rate of decrease is not sufficiently large for the h_f' curve to fall below the lateral slope upstream of the 319.9m point. In summary, the simulated data shows that an increase in pipe absolute roughness led to increases in h_f' . Increases in h_f' , in a lateral with a constant slope, in turn resulted in an increase in the distance of the minimum pressure head point from the lateral inlet. Note that these results are consistent with the explanation provided above for the observed downstream shift in minimum pressure head point along the lateral.

Sensitivity of sprinkler discharge profile to pipe absolute roughness

The sensitivity of sprinkler discharge profiles to lateral pipe absolute roughness is depicted in Figure 14f. Considering the lower limit of the pipe absolute roughness range (0.127mm), the sprinkler discharge decreases monotonically with distance from a maximum of about 0.1026L/s at the upstream end sprinkler to a minimum of 0.1011L/s at a distance of about 310.8m. Sprinkler discharge then rises slightly to about 0.1012L/s at the distal end of the lateral. As the pipe absolute roughness is increased to 0.254, then to 0.508, and 0.762mm the broad spatial pattern of the sprinkler discharge profile, along a lateral, remains the same as that obtained for pipe absolute roughness of 0.127mm (Figure 14f). However, the maximum sprinkler discharge decreases marginally from about 0.1026L/s to 0.1025L/s, as absolute roughness is increased from 0.127mm to 0.762mm. The minimum discharge decreases slightly from 0.1011L/s for absolute roughness of 0.127mm to 0.1003L/s for absolute roughness of

0.762mm and the point of minimum discharge, along the lateral, moves slightly downstream from 310.8m for absolute roughness of 0.127mm to 319.9m for a lateral with roughness value 0.726mm. Overall, a 500% increase in pipe absolute roughness led only to a maximum of about 0.8% decrease in the minimum lateral discharge. Thus for the scenario considered here, in practical terms lateral discharge is nearly insensitive to variations in pipe absolute roughness.

The spatial patterns of sprinkler discharge profiles along laterals expressed as a function pipe absolute roughness are about the same as those obtained for the lateral pressure head profiles (Figure 14f). Considering that sprinkler discharges are closely related to local lateral pressure heads, the similarity between the two sets of curves is consistent with intuitive hydraulic reasoning.

6. Summary and Conclusion

A hydraulic simulation model is developed for an irrigation lateral operated under steady-state condition. The formulation and numerical solution of the irrigation lateral hydraulic simulation problem, presented here, is based on an adaptation of the gradient method, developed originally for the simulation of pipeline networks with complex topologies. For computational purpose, an irrigation lateral is described here as a branched hydraulic network comprised of a series of interconnected links, each delimited by nodes. Lateral pipe sections and riser-emitter ensembles (or emitters) are considered as hydraulic links. The network nodes consist of junction nodes with unknown heads (marking the intersections of hydraulic links) and fixed head nodes, comprised of boundary nodes with externally imposed constant heads. Pipe appurtenances such as valves and fittings and other features that introduce local head losses are treated as properties of the lateral pipe segment they are placed on. Inline devices that add energy into or remove energy from the flow are not considered. The hydraulic characteristics of emitters can vary along the lateral. Furthermore, lateral pipe segment diameter, length, spatial orientation, slope, and hydraulic resistance characteristics can differ along a lateral. In addition, a couple of different pipe appurtenances can be fitted into any of the lateral pipe segments. However, a single set of pipe diameter, slope, and hydraulic resistance parameters needs to be used to characterize a lateral pipe segment.

The energy balance and continuity equations for one-dimensional steady incompressible flow are used to describe the hydraulics of this system. The energy balance equation is written across each hydraulic link and the continuity equation is formulated for each junction node.

These equations are assembled to form a nonlinear system, which is then partitioned for block matrix representation. This formulation leads to a system that is amenable to detailed yet compact presentation and possibly to an efficient numerical solution. The resultant system of equations are solved for the variables (i.e., the link discharge, Q , and nodal head, H , vectors) iteratively with the Newton-Raphson method.

Evaluation of the lateral hydraulic simulation model, developed in the study reported here, is conducted at different levels. First the consistency of the numerical solution implemented in the model was tested by comparing intermediate and final outputs of the model with manual calculations. Then the outputs of the model are compared with the outputs of EPANET and of another model developed, by the same authors, based on manifold hydraulics. The model is further evaluated based on comparisons of its outputs with field measured data. Finally, sensitivity analysis is conducted in order to evaluate the spatial patterns of model predicted lateral hydraulic characteristics under a range of conditions. Seven data sets, consisting of both hypothetical and field measured data, covering a wide range of lateral hydraulic, geometric, and slope conditions are used in model evaluation.

The goal of the numerical solution consistency test is to evaluate if the different functions and component modules of the model are performing the functions they are designed for. Four hydraulic variables and parameters are selected for conducting these tests: the Darcy-Weisbach friction factor for each pipe segment of a lateral, the sprinkler discharges, lateral discharges, and nodal heads. The difference between model computed and manually calculated values of the respective parameters or variables, expressed as percent of their manually calculated values, is used as a metric to assess the consistency of the numerical solution. Five data sets were used in this evaluation. Considering all the data sets, the percent differences between the manually calculated and model computed variables or parameters are in the order of $10^{-5.40}\%$ or less. These results show that the manually calculated and model computed parameters and variables are in good agreement, thus model computations can be considered internally consistent.

Additional model evaluation is conducted based on comparisons of pressure head and sprinkler discharge profiles, along a lateral, computed with the current model and with another model, developed based on manifold hydraulics. Five data sets were used in comparing the models. Considering all the data sets, the maximum and average percent differences between the lateral pressure head profiles computed with the two models are 0.260% and 0.143%, respectively. The overall maximum and average percent differences between the sprinkler

discharges computed with the two models are 0.255% and 0.071%, respectively. These results suggest that the outputs of the gradient and manifold models are essentially identical. The fact that the lateral pressure head and sprinkler discharges computed with the two models, which are based on entirely different numerical algorithms, are in good agreement suggests that the formulation and numerical solution of the lateral hydraulic simulation problem in both models is sound. Most importantly, these results lend support to the validity of the numerical algorithm implemented in the current model, which is by far the most complex of the two models compared here.

Furthermore, lateral pressure head and sprinkler discharge profiles simulated with the lateral hydraulic model and EPANET were compared. Five data sets were used in comparing the models. Considering all the data sets, the maximum and average percent differences between the lateral pressure head profiles computed with the two models are 0.849% and 0.114%, respectively. The overall maximum and average percent differences between the sprinkler discharges computed with the two models are 0.405% and 0.059%, respectively. These results suggest that the pressure head and sprinkler discharges simulated with the two models are in close agreement.

Further evaluation of the model, developed in the current study, is conducted based on comparisons of model computed and measured pressure head profiles. Measured pressure head data along four laterals, of a field-scale solid-set sprinkler system, is used in this evaluation. Considering all the data sets, the percent differences between the simulated and measured pressure heads vary between a minimum of 0.2% and a maximum of 3.8% and the overall average percent difference is 1.6%. The model prediction error is sufficiently low for the simulated lateral pressure head profiles to be considered a close match to the measured data.

Sensitivity analysis of lateral pressure head and sprinkler discharge profiles to variations in lateral slope, lateral diameter, and absolute roughness is conducted based on a field measured lateral data set. Five lateral slopes ranging from -0.5 to 0.25%, five standard lateral diameters varying between 38.1 and 88.9mm, and four pipe absolute roughness values ranging from 0.127 to 0.762mm are used in the analysis. The broad spatial patterns of the simulated pressure head profiles are consistent with hydraulic theory.

Application of the numerical algorithm developed here is limited to the hydraulic simulation of irrigation laterals. However, following the approach proposed by Zerihun et al. (2014) and Zerihun and Sanchez (2014), the numerical solution developed here can be readily integrated into a field-scale pressurized irrigation system hydraulic characterization and simulation model.

References

- Boulos, P.F., Lansey, K.E., and Karney, B.W. (2006). *Comprehensive Water Distribution Systems Analysis Handbook for Engineers and Planners*. 2nd Ed., MWH Soft, Pasadena, CA.
- Boulos, P.F., and Altman, T. (1991). A graph theoretic approach to explicit nonlinear pipe network optimization. *Appl. Math. Modelling*, 15:459-466.
- Cross, H. (1936). *Analysis of flows in networks of conduits or conductors*. Bulletin No. 286, University of Illinois Engineering Experimental Station, Urbana, IL.
- Dunlop, E.J. (1991). *WADI Users manual*. Local Government Computers Services Board, Dublin, Ireland.
- Epp, R. and Fowler, A.G. (1970). Efficient code for steady-state flows in networks. *J. Hydraul. Div.*, ASCE, 96(1):43-56.
- Estrada, C., Gonzalez, C., Aliod, R., and Pano, J. (2009). Improved pressurized pipe network hydraulic solver for applications in irrigation systems. *J. Irrig. Drain Eng.*, ASCE, 135(4):421-430.
- Granger, R.A. (1995). *Fluid Mechanics*. Dover Publications Inc., New York, NY.
- Hathoot, H.M., Abo-Ghobar, H.M., Al-Amudi, A.I. (1994). Analysis and Design of sprinkler irrigation laterals. *J. Irrig. Drain Eng.*, ASCE, 120(3):534-549.
- Karney, B.W. (2000). Chapter 2. Hydraulics of pressurized flow. *In Water Distribution Systems Handbook* (Mays, L.W., ed.), McGraw-Hill, New York, NY.
- Keller, J. and Bliesner, R. (1990). *Sprinkle and trickle irrigation*. Van Nostrand Reinhold, New York, NY.
- Lansey, K. and Mays, L.W. (2000). Chapter 4. Hydraulics of water distribution systems. *In Water Distribution Systems Handbook* (Mays, L.W., ed.), McGraw-Hill, New York, NY.
- Larock, B. E., Jeppson, R.W., and Watters, G. Z. (2000). *Hydraulics of pipeline systems*. CRC Press, Washington, D.C.

- Marriott, M.J., Featherstone, R.E., and Nalluri, C. (2009). *Nalluri & Featherstone's Civil Engineering Hydraulics*. John Wiley & Sons Ltd., 5th Ed., West Sussex, UK.
- Martin, D.L., Heermann, D.F., and Madison, M. (2007). *Design and Operation of Farm Irrigation systems. Chapter 15. Hydraulics of sprinkler and microirrigation systems*, Hoffmann, G.J., Evans, R.G., Jensen, M.E., Martin, D.L., Elliott, R.L., eds., 2nd Ed., ASABE, St. Joseph, MI, pp.532-555.
- Miller, D. S. (2009). *Internal flow systems*. Miller Innovations, Bedford, UK.
- Nielsen, H.B. (1989). Methods for analyzing pipe networks. *J. Hydraul. Eng.*, ASCE, 115(2): 139-157.
- Press, W.H., Teukolsky, S.A., Vetterling, W.T., and Flannery, B.P (1997). *Numerical Recipes in C, the art of scientific computing*. Cambridge University Press, New York, NY.
- Rossman, L.A. (2000). *EPANET 2 Users Manual*. Water Supply and Water Resources Division, National Risk Management Research Laboratory, U.S. Environmental Protection Agency, Cincinnati, OH.
- Salgado, R., Todini, E., O'Connell, P.E. (1987). Comparison of the gradient method with some traditional methods for the analysis of water supply distribution networks. *Proceedings of the International conference on computer applications for water supply and distribution*, Leicester Polytechnic, UK, September, 1987.
- Shamir, U. and Howard, C.D.D. (1968). Water distribution systems analysis. *J. Hydraul. Div*, ASCE, 94(1): 219-234.
- Todini, E. and Pilati, S. (1987). A gradient algorithm for the analysis of pipe networks. *Proceedings of the International conference on computer applications for water supply and distribution*, Leicester Polytechnic, UK, September, 1987.
- Wood, D.J and Charles, C.O.A. (1972). Hydraulic network analysis using linear theory. *J. Hydraul. Div*, ASCE, 98(7):1157-1170.
- Wood, D.J. and Rayes, A.G. (1981). Reliability of algorithms for pipe network analysis. *J. Hydraul. Div.*, ASCE, 107(10):1145-1161.
- Zerihun, D. and Sanchez, C.A. (2012). *Field and modeling study of sprinkler irrigation for season long vegetable production in the Yuma Valley Irrigation Districts*. Report submitted to the USBR.
- Zerihun, D., Sanchez, C.A., Nolte, K. (2011). *Evaluation of sprinkler irrigation systems for season long vegetable production in the Yuma Valley Irrigation Districts*. Report submitted to the Arizona Specialty Crops Council.

- Zerihun, D., Sanchez, C.A., Nolte, K. (2014). Field-scale sprinkler irrigation hydraulic model. I: Hydraulic characterization. *J. Irrig. Drain, Eng.*, ASCE, 1407):04014019-1-14
- Zerihun, D. and Sanchez, C.A. (2014). Field-scale sprinkler irrigation hydraulic model. II: Hydraulic simulation. *J. Irrig. Drain, Eng.*, ASCE, 1407):04014020-1-14.

Appendix I. Derivation of the expressions for the elements of the inverse of the Jacobian matrix

In this section expressions for the elements of the inverse of the Jacobian matrix are derived. The form of the Jacobian matrix evaluated based on the estimate of the link discharges at the m th iteration, θ^m (Eq. 34), is

$$\theta^m = \begin{pmatrix} (\Psi'_{11})^m & \Psi_{12} \\ \Psi_{21} & 0 \end{pmatrix} \quad (I.1)$$

With the view of keeping the derivation simple, define a matrix, α , such that

$$(\alpha^m)^{-1} = (\Psi'_{11})^m \quad (I.2)$$

From Eq. 36, we define a matrix β , such that $\beta = (\theta^m)^{-1}$, which is given as

$$\beta = \begin{pmatrix} \beta_{11} & \beta_{12} \\ \beta_{21} & \beta_{22} \end{pmatrix} \quad (I.3)$$

Expressions for the elements of β , in terms of the elements of θ^m (Eq. I.1), are computed in the following steps (Lipschutz, 1991):

1. Form an augmented 2×4 matrix, Π , of the form

$$\Pi = (\theta^m / I) \quad (I.4)$$

where I is identity matrix;

2. Reduce Π to echelon form, Π_{re} . A matrix in echelon form is one in which each leading nonzero element is to the right of the leading nonzero entry in the preceding row and all zero rows, if any, are at the bottom of the matrix. If the row reduction produces a zero row, matrix θ^m is singular and hence not invertible.
3. Reduce Π_{re} into row canonical form, Π_{rc} .

$$\Pi_{rc} = (I / A) \quad (I.5)$$

An echelon matrix is considered to be in row canonical form if each leading nonzero element is I (note that I should be used in place of 1 for block matrices) and each leading nonzero entry is the only nonzero element in its column.

4. Set $(\boldsymbol{\theta}^m)^{-1} = \boldsymbol{\Lambda}$, thus $\boldsymbol{\beta} = \boldsymbol{\Lambda}$;

Now, we will follow these steps to compute the inverse of the Jacobian matrix.

Step 1: Form the augmented matrix, $\boldsymbol{\Pi}$:

$$\boldsymbol{\Pi} = \left(\boldsymbol{\theta}^m \mid \mathbf{I} \right) = \left(\begin{array}{cc|cc} (\boldsymbol{\alpha}^m)^{-1} & \boldsymbol{\Psi}_{12} & \mathbf{I} & \mathbf{0} \\ \boldsymbol{\Psi}_{21} & \mathbf{0} & \mathbf{0} & \mathbf{I} \end{array} \right) \quad (1.6)$$

Step 2: Reduce matrix $\boldsymbol{\Pi}$ to its echelon form, $\boldsymbol{\Pi}_{re}$, through the following row operations

(2a) Replace R_1 by $\boldsymbol{\alpha}^m R_1$ (where R_1 is row 1):

$$\left(\begin{array}{cc|cc} \mathbf{I} & \boldsymbol{\alpha}^m \boldsymbol{\Psi}_{12} & \boldsymbol{\alpha}^m & \mathbf{0} \\ \boldsymbol{\Psi}_{21} & \mathbf{0} & \mathbf{0} & \mathbf{I} \end{array} \right) \quad (1.7)$$

(2b) Replace R_2 by $\boldsymbol{\Psi}_{21} R_1 - R_2$ (where R_2 is row 2):

$$\boldsymbol{\Pi}_{re} = \left(\begin{array}{cc|cc} \mathbf{I} & \boldsymbol{\alpha}^m \boldsymbol{\Psi}_{12} & \boldsymbol{\alpha}^m & \mathbf{0} \\ \mathbf{0} & \boldsymbol{\Psi}_{21} \boldsymbol{\alpha}^m \boldsymbol{\Psi}_{12} & \boldsymbol{\Psi}_{21} \boldsymbol{\alpha}^m & -\mathbf{I} \end{array} \right) \quad (1.8)$$

Step 3: Reduce $\boldsymbol{\Pi}_{re}$ into row canonical form, $\boldsymbol{\Pi}_{rc}$, through the following row operations:

(3a) Replace R_2 by the product $(\boldsymbol{\Psi}_{21} \boldsymbol{\alpha}^m \boldsymbol{\Psi}_{12})^{-1} R_2$

$$\left(\begin{array}{cc|cc} \mathbf{I} & \boldsymbol{\alpha}^m \boldsymbol{\Psi}_{12} & \boldsymbol{\alpha}^m & \mathbf{0} \\ \mathbf{0} & \mathbf{I} & (\boldsymbol{\Psi}_{21} \boldsymbol{\alpha}^m \boldsymbol{\Psi}_{12})^{-1} \boldsymbol{\Psi}_{21} \boldsymbol{\alpha}^m & -(\boldsymbol{\Psi}_{21} \boldsymbol{\alpha}^m \boldsymbol{\Psi}_{12})^{-1} \end{array} \right) \quad (1.9)$$

(3b) Replace R_1 by the expression $R_1 - \boldsymbol{\alpha}^m \boldsymbol{\Psi}_{12} R_2$

$$\boldsymbol{\Pi}_{rc} = \left(\begin{array}{cc|cc} \mathbf{I} & \mathbf{0} & \boldsymbol{\alpha}^m - \boldsymbol{\alpha}^m \boldsymbol{\Psi}_{12} (\boldsymbol{\Psi}_{21} \boldsymbol{\alpha}^m \boldsymbol{\Psi}_{12})^{-1} \boldsymbol{\Psi}_{21} \boldsymbol{\alpha}^m & \boldsymbol{\alpha}^m \boldsymbol{\Psi}_{12} (\boldsymbol{\Psi}_{21} \boldsymbol{\alpha}^m \boldsymbol{\Psi}_{12})^{-1} \\ \mathbf{0} & \mathbf{I} & (\boldsymbol{\Psi}_{21} \boldsymbol{\alpha}^m \boldsymbol{\Psi}_{12})^{-1} \boldsymbol{\Psi}_{21} \boldsymbol{\alpha}^m & -(\boldsymbol{\Psi}_{21} \boldsymbol{\alpha}^m \boldsymbol{\Psi}_{12})^{-1} \end{array} \right) \quad (1.10)$$

Note that the matrix in Eq. I.10 is of the same form as that of Eq. I.5. Thus,

$$\mathbf{A} = \begin{pmatrix} \alpha^m - \alpha^m \Psi_{12} (\Psi_{21} \alpha^m \Psi_{12})^{-1} \Psi_{21} \alpha^m & \alpha^m \Psi_{12} (\Psi_{21} \alpha^m \Psi_{12})^{-1} \\ (\Psi_{21} \alpha^m \Psi_{12})^{-1} \Psi_{21} \alpha^m & -(\Psi_{21} \alpha^m \Psi_{12})^{-1} \end{pmatrix} \quad (I.11)$$

Step 4: $(\theta^m)^{-1} = \mathbf{A}$, thus $\beta = \mathbf{A}$: Comparing Eqs. I.11 and I.3, it follows that

$$\beta_{11} = \alpha^m - \alpha^m \Psi_{12} (\Psi_{21} \alpha^m \Psi_{12})^{-1} \Psi_{21} \alpha^m \quad (I.12)$$

$$\beta_{12} = \alpha^m \Psi_{12} (\Psi_{21} \alpha^m \Psi_{12})^{-1} \quad (I.13)$$

$$\beta_{21} = (\Psi_{21} \alpha^m \Psi_{12})^{-1} \Psi_{21} \alpha^m \quad (I.14)$$

$$\beta_{22} = -(\Psi_{21} \alpha^m \Psi_{12})^{-1} \quad (I.15)$$

Appendix II. Algorithm for the iterative computation of the Darcy-Weisbach friction factor

The following procedure is used to compute the friction factor for the i th link based on the link discharge at the m th iteration, f_i^m . Note that to simplify the discussion, in subsequent presentation the friction factor is referenced simply as f , without the subscript and superscript.

First, write the Colebrook-White equation, Eq. 6, in a form amenable to iterative solution

$$F(f) = \frac{1}{\sqrt{f}} - 1.14 + 2 \log \left(\frac{e}{D} + \frac{9.35}{R_e \sqrt{f}} \right) \quad (II.1)$$

Given the pipe segment absolute roughness, diameter, discharge, and a current estimate of f , f^c , the function $F(f^c)$ represents the residual associated with the error in the current estimate of f . A revised estimate of the friction factor, f^r , is computed as a function of the current estimate f , f^c , with the Newton iterative relationship

$$f^r = f^c - \frac{F(f^c)}{F'(f^c)} \quad (II.2)$$

In Eq. II.2, $F'(f^c)$ is the derivative of $F(f)$ with respect to f evaluated at $f = f^c$ and is given as

$$F'(f) = -\left(\frac{1}{\sqrt{f}}\right)^3 \left(\frac{1}{2} + 4.063 \left/ \left(Re \left(\frac{e}{D} + \frac{9.35}{Re \sqrt{f}} \right) \right) \right) \right) \quad (II.3)$$

The iterative steps for computing f are depicted in the flow chart in Figure II.1 and are summarized as follows:

1. If $Re \leq 4000$ proceed to step 2; If not proceed to step 3;
2. Calculate f with Eq. 5; end computation and return to the sub-process for computing the Ψ_{II} matrix, Appendix III;
3. Set $j = 0$ (where j is the iteration index) and proceed to step 4;
4. Initialize f :
 - 4a. If $m = 0$ (where m is the gradient iteration index), then set f^c to the value of f for the corresponding fully turbulent zone (Eq. II.4) and proceed to step 5; If $0 < m$ then proceed to step 4b

$$f = \left(\frac{1}{1.14 - 2 \log \left(\frac{e}{D} \right)} \right)^2 \quad (II.4)$$

- 4b. Set $f^c = f^{(m-1)}$ (where $f^{(m-1)}$ is the value of f at the $(m-1)$ th gradient iteration) and proceed to step 5;
5. Evaluate $F(f^c)$ with Eq. II.1 and proceed to step 6;
6. Evaluate $F'(f^c)$ with Eq. II.3 and proceed to step 7;
7. Calculate a revised estimate of f , f^r , with Eq. II.2 and proceed to step 8;
8. Test for convergence: proceed to step 8a:
 - 8a. If $|f^r - f^c| \leq 10^{-8}$ proceed to step 10; If not proceed to step 8b;
 - 8b. Set $j = j + 1$ and $f^c = f^r$ and proceed to step 9;
9. If $j \leq 30$, then proceed to step 5; if $30 < j$, iteration failed to converge, end computation;
10. The iteration has converged, set $f = f^r$; end computation and return to the subprocess for computing the Ψ_{II} matrix;

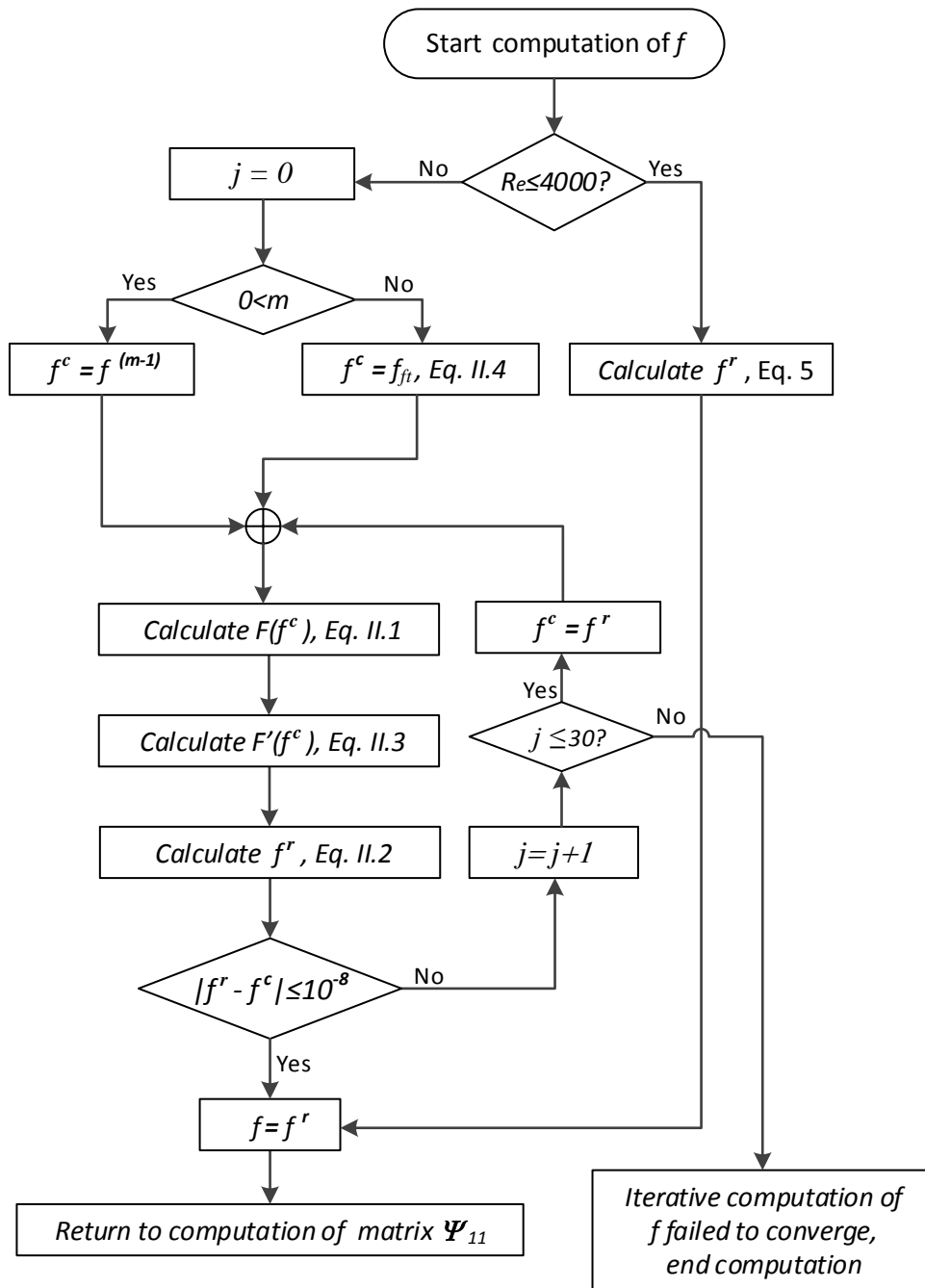


Figure II.1. Flow chart for computing the Darcy-Weisbach friction factor, f , for the i th link (i.e., lateral pipe segment or riser pipe) evaluated based on the link discharge at the m th iteration, Q_i^m (where f^c is current estimate of f ; f^r is a revised estimate of f ; f_{ft} is the value of f for the i th pipe segment when the flow is in the fully turbulent zone)

Appendix III. Algorithm for computing the Ψ_{11} matrix at the $(m+1)$ th gradient iteration

The computational procedure for updating the Ψ_{11} matrix (Eq. 29 and Table 6) at the $(m+1)$ th iteration, based on the discharge vector at the m th iteration, is depicted in Figure III.1.

The following is a summary of the computational steps:

1. Set $i = 1$ (where i is the link index) and proceed to step 2;
2. If i is odd integer proceed to step 3; If not proceed to step 5;

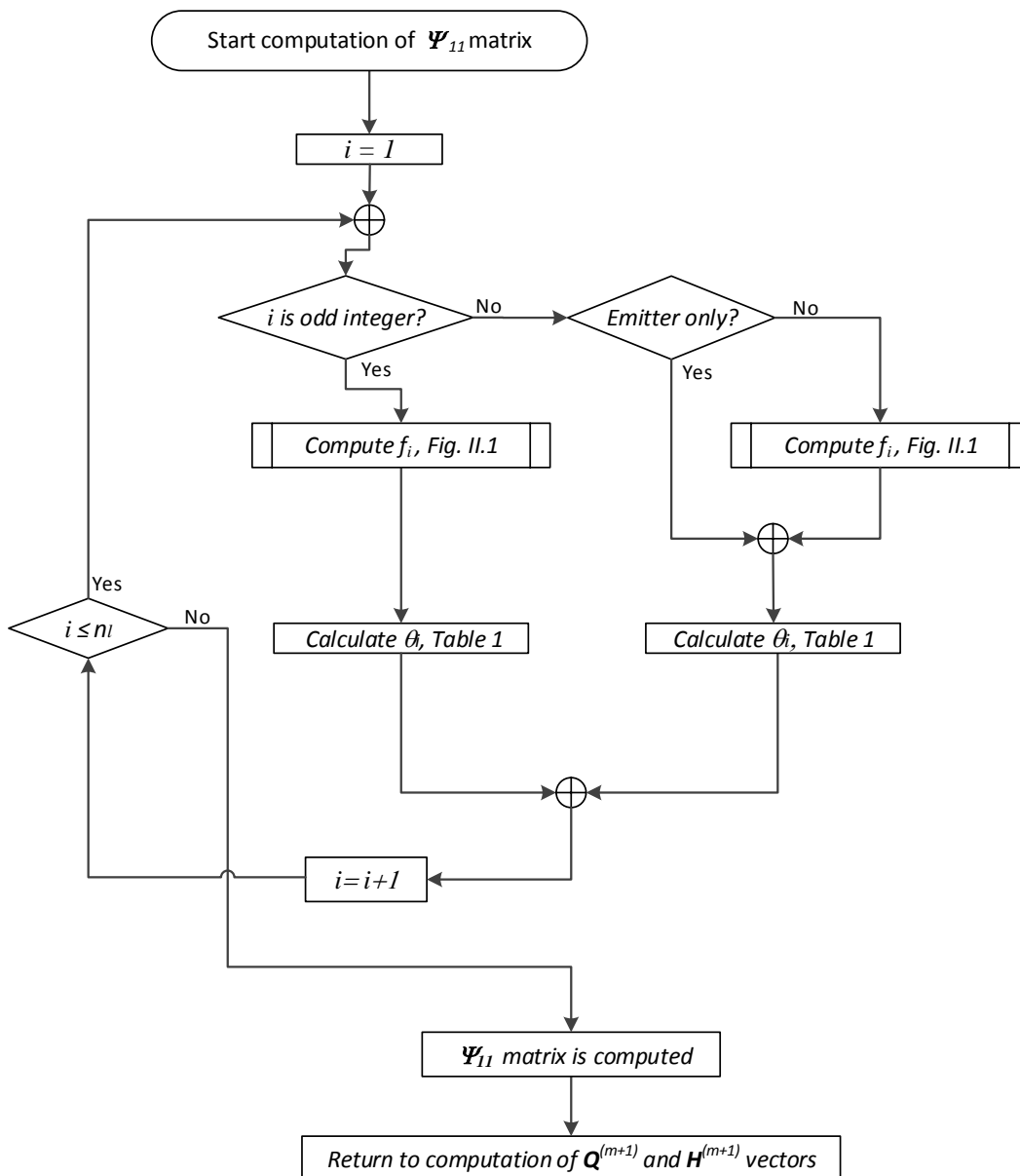


Figure III.1. Flow chart for updating the Ψ_{11} matrix at the $(m+1)$ th iteration based on the discharge vector at the m th iteration, \mathbf{Q}^m (where i is link index, f_i is the friction factor for the i th link computed iteratively based on the link discharge at the m th gradient iteration, and n_l is number of links in the lateral)

3. Compute f_i (where f_i is the friction factor for the i th lateral pipe segment evaluated based on the link discharge at the m th iteration) and proceed to step 4; (*Note: A description of the sub-process for computing f_i is presented in Appendix II*);
4. Calculate θ_i for the i th lateral pipe segment (Table 1) and proceed to step 7;
5. If emitter is placed directly on lateral then proceed to step 5.1; If not (i.e., emitter is placed on riser pipe), proceed to step 6;
 - 5.1. Calculate θ_i for the i th emitter (Table 1) and proceed to step 7;
6. Compute f_i (where f_i is the friction factor for the i th riser pipe segment evaluated based on the emitter discharge at the m th iteration) and proceed to step 6.1; (*Note: A description of the sub-process for computing f_i iteratively is presented in Appendix II*);
 - 6.1. Calculate θ_i for the i th riser-emitter ensemble (Table 1) and proceed to step 7;
7. Set $i = i+1$ and proceed to step 8;
8. If $i \leq n_l$ (where n_l is the number of links in the lateral) proceed to step 2; If not proceed to step 9;
9. The Ψ_{1l} matrix is evaluated based on the m th estimate of the link discharge vector, \mathbf{Q}^m ; end computation and return to the gradient algorithm (Figure 6);

Appendix IV. Expressions for the derivatives of the friction factor with respect to discharge

Expressions for the derivatives of the friction factor for a pipe segment, f , with respect to discharge, Q , are presented in this section.

For $Re \leq 4000$, f can be evaluated with

$$f = \frac{64}{Re} \quad (IV.1)$$

and

$$\frac{\partial f}{\partial Q} = -64 \frac{\partial Re}{\partial Q} \frac{1}{Re^2} \quad (IV.2)$$

Noting that

$$\frac{\partial Re}{\partial Q} = \frac{Re}{Q} \quad (IV.3)$$

The derivative of f with respect to Q for $Re \leq 4000$ can be expressed as

$$f' = -\frac{64}{ReQ} \quad (IV.4)$$

where $f' = \frac{\partial f}{\partial Q}$

For turbulent flow, $4000 < Re$, the friction factor, f , is given as

$$f^{-(1/2)} = 1.14 - 0.869 \ln \rho \quad (IV.5)$$

where

$$\rho = \frac{e}{D} + \frac{9.35}{Re\sqrt{f}} \quad (IV.6)$$

and its derivative with respect to the pipe section discharge is expressed as

$$\frac{\partial(f^{-(1/2)})}{\partial Q} = -0.869 \frac{\partial(\ln \rho)}{\partial Q} \quad (IV.7)$$

which can then be given as

$$\frac{1}{2} f^{-(3/2)} f' = \frac{0.869}{\rho} \frac{\partial \rho}{\partial Q} \quad (IV.8)$$

In Eq. IV.8, $\frac{\partial \rho}{\partial Q}$ is

$$\frac{\partial \rho}{\partial Q} = -9.35 \frac{\left(\frac{\partial(Re f^{(1/2)})}{\partial Q} \right)}{(Re\sqrt{f})^2} \quad (IV.9)$$

Expanding the numerator yields

$$\frac{\partial \rho}{\partial Q} = -9.35 \frac{\left(Re f^{(1/2)} + \frac{1}{2} Q Re f^{-(1/2)} f' \right)}{Q(Re)^2 f} \quad (IV.10)$$

Simplifying and rearranging yields

$$\frac{\partial \rho}{\partial Q} = -4.675 f^{-(3/2)} \frac{(2f + Qf')}{QR_e} \quad (IV.11)$$

Substituting Eqs. IV.6 and IV.11 in Eq. IV.8 and simplifying yields

$$\frac{\partial f}{\partial Q} = -8.125 \frac{2f + Qf'}{QR_e \left(\frac{e}{D} + \frac{9.35}{R_e \sqrt{f}} \right)} \quad (IV.12)$$

The derivative of f with respect to Q for $4000 < R_e$ can then be expressed as

$$f' = -16.25 \frac{f}{Q \left[R_e \left(\frac{e}{D} + \frac{9.35}{R_e \sqrt{f}} \right) + 8.125 \right]} \quad (IV.13)$$

For a pipe section, f' can be calculated directly with Eq. IV.4 for $R_e \leq 4000$ or with Eq. IV.13 for $4000 < R_e$.

Appendix V. Algorithm for computing the Ψ'_{11} matrix at the $(m+1)$ th iteration

The computational procedure for updating the Ψ'_{11} matrix at the $(m+1)$ th iteration based on the link discharges at the m th iteration are shown in Figure V.1.

The following is a summary of the computational steps:

1. Set $i = 1$ (where i is the link index); proceed to step 2;
2. If i is odd integer proceed to step 3; If not proceed to step 5;
3. Compute f_i' with Eq. 60 or 61 and proceed to step 4; (*Note: f_i' is the derivative of the friction factor for the i th lateral pipe segment with respect to the i th lateral pipe segment discharge, evaluated based on the discharge at the m th gradient iteration*)
3. Calculate $F'_{eQ_i} \Big|_{Q_i^m}$ with Eq. 59 and proceed to step 7 (*where Q_i^m is the i th lateral pipe segment discharge at the m th gradient iteration*);
5. If emitter is placed directly on lateral then proceed to step 5.1; If not (i.e., emitter is placed on riser pipe) then proceed to step 6;

5.1. Calculate $F'_{eQ_i} \Big|_{Q_i^m}$ with Eq. 62 for the i th emitter and proceed to step 7 (where Q_i^m is the i th emitter discharge at the m th gradient iteration);

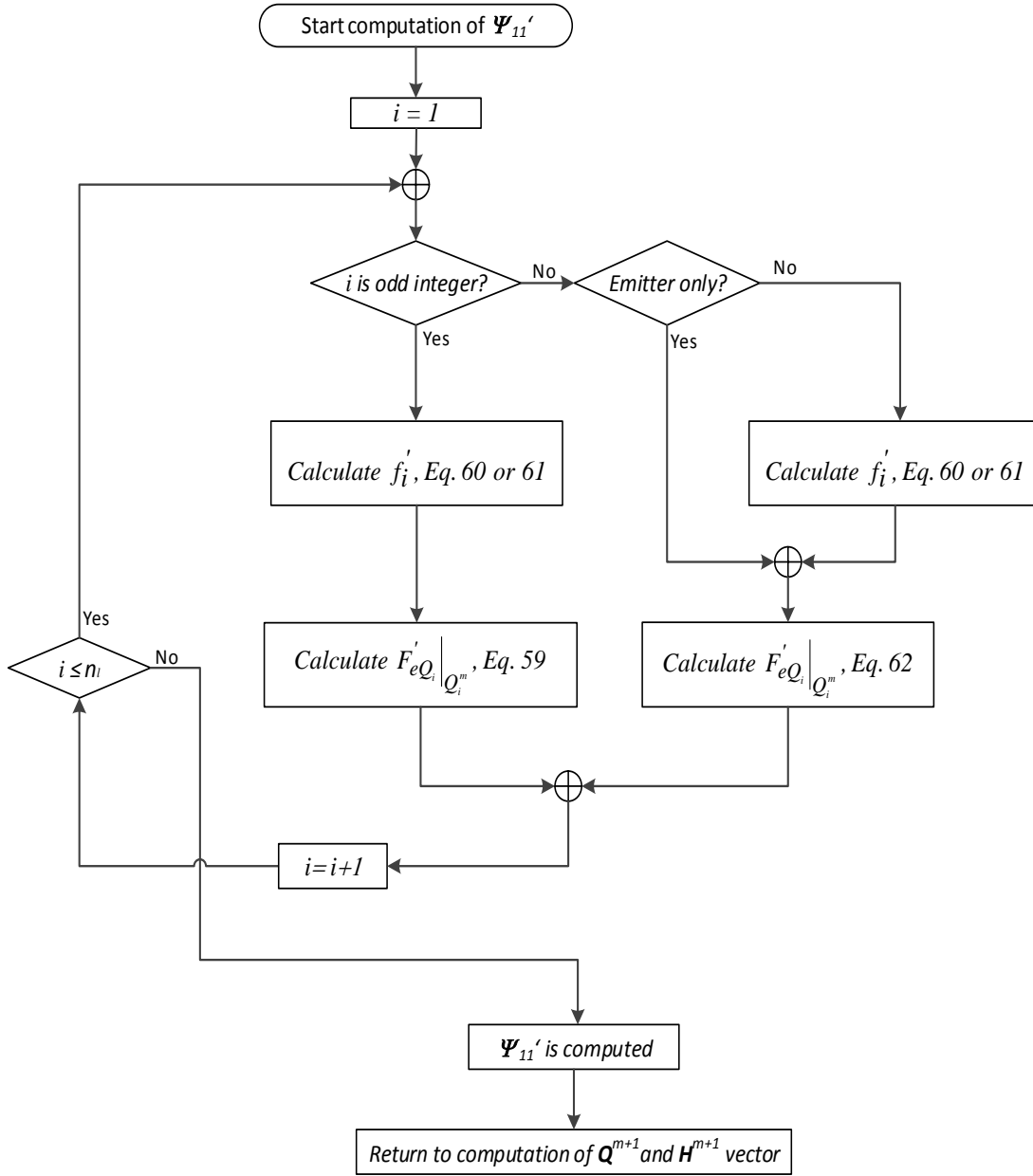


Figure V.1. Flow chart for updating the Ψ_{11}' matrix at the $(m+1)$ th iteration based on the discharge vector at the m th gradient iteration, \mathbf{Q}^m (where $F'_{eQ_i} \Big|_{Q_i^m}$ is the derivative of the i th link energy balance equation with respect to the i th link discharge evaluated based on Q_i^m ; and f_i' is the derivative of f with respect to the i th link discharge evaluated based on Q_i^m)

6. Compute f_i' with Eq. 60 or 61 and proceed to step 6.1 (where f_i' is the derivative of the friction factor for the i th riser pipe with respect to the i th emitter discharge, evaluated based on the discharge at the m th gradient iteration);

6.1. Calculate $F_e' Q_i \Big|_{Q_i^m}$ with Eq. 62 for the i th riser-emitter ensemble and proceed to step 7

(where Q_i^m is the i th emitter discharge at the m th gradient iteration);

7. Set $i = i+1$ and proceed to step 8;

8. If $i \leq n_l$ (where n_l is the number of links in the lateral) proceed to step 2, if not proceed to step 9;

9. The Ψ_{11}' matrix is evaluated based on the m th estimate of the link discharge vector, \mathbf{Q}^m ; end computation and return to the gradient algorithm (Figure 6);

Appendix VI. Computation of the inverse of a matrix with LU factorization

For clarity, Eqs. 63-69 (section 4.2.6) are reproduced here. We consider here a square matrix, Δ , of some arbitrary dimension, $q \times q$, with elements labeled as Δ_{ij} , such that

$$\Delta_{ij} \in \mathbf{R} \quad (\text{VI.1})$$

In Eq. VI.1, i and j are row and column indices, respectively, of matrix Δ ; \mathbf{R} is the set of real numbers; and \in is the standard set notation that implies that Δ_{ij} is a member of the set of real numbers.

Further assume that matrix Δ is nonsingular and has an inverse, Δ^{-1} , then by definition

$$\mathbf{I} = \Delta \Delta^{-1} \quad (\text{VI.2})$$

where \mathbf{I} is identity matrix with the same dimension as Δ and can be defined as

$$\lambda_{ij} = \begin{cases} 1, & \text{for } i = j \\ 0, & \text{for } i \neq j \end{cases} \quad (\text{VI.3})$$

In Eq. VI.3, λ_{ij} is the element of \mathbf{I} on its i th row and j th column. Note that Δ^{-1} has the same dimension and structure as Δ and its elements, labeled here as σ_{ij} , are real numbers.

We assume here that matrix Δ can be factorized into a lower triangular, L , and an upper triangular, U , matrices with LU factorization method, such that

$$\Delta = LU \quad (VI.4)$$

Substituting Eq. VI.4 in Eq. VI.2 yields

$$I = LU\Delta^{-1} \quad (VI.5)$$

Letting

$$\Phi = U\Delta^{-1} \quad (VI.6)$$

where Φ is a $q \times q$ matrix with elements ϕ_{ij} , such that $\phi_{ij} \in \mathbf{R}$; Eq. VI.5 can be expressed as

$$I = L\Phi \quad (VI.7)$$

Computational steps to determine Δ^{-1}

In the model developed here, computation of the inverse of matrix Δ , Δ^{-1} , with an LU factorization algorithm is undertaken in the following steps

- i. *Factorize Δ* : Factorize matrix Δ into a lower, L , and an upper, U , triangular matrices (VI.4) with Crout's algorithm;
- ii. *Compute Φ* : Compute Φ with VI.7 through forward substitution, starting from the first row and proceeding sequentially down to the bottom row;
- iii. *Compute Δ^{-1}* : Compute Δ^{-1} with VI.6 through back substitution, starting from the bottom row and proceeding sequentially up to the first row;

i. *LU factorization of matrix Δ (Crout's method)*

Matrix L is of the same dimension as matrix Δ and has the following properties and structure

$$\left. \begin{array}{l} \ell_{ij} \in \mathbf{R}, \quad \text{for } i = 1, 2, \dots, q \quad \text{and} \quad j = 1, 2, \dots, q \\ \ell_{ij} = 0, \quad \text{for } i < j \\ \ell_{ij} \neq 0, \quad \text{for } i = j \end{array} \right\} \quad (VI.8)$$

where ℓ_{ij} is element of matrix \mathbf{L} on its i th row and j th column. Matrix \mathbf{U} as well is of the same dimension as matrix \mathbf{A} and has the following properties and structure

$$\left. \begin{aligned} u_{ij} &\in \mathbf{R}, \quad \text{for } i = 1, 2, \dots, q \quad \text{and } j = 1, 2, \dots, q \\ u_{ij} &= 0, \quad \text{for } j < i \\ u_{ij} &= 1, \quad \text{for } i = j \end{aligned} \right\} \quad (\text{VI.9})$$

In Eq. VI.9, u_{ij} is element of matrix \mathbf{U} on its i th row and j th column. Computation of the nonzero elements of the \mathbf{L} and \mathbf{U} matrices proceeds alternately, in which calculation of a column of the \mathbf{L} matrix is followed by the corresponding row of the \mathbf{U} matrix:

i.1. Compute the first column of the \mathbf{L} matrix: from row-column operation of matrix multiplication and Eq. VI.4, it can be observed that

$$A_{i1} = \sum_{k=1}^j \ell_{ik} u_{k1}, \quad \text{for } i = 1, 2, \dots, q \quad (\text{VI.10})$$

where i is row index of matrices \mathbf{A} and \mathbf{L} and k is column and row index of \mathbf{L} and \mathbf{U} , respectively. Noting that for $l < k$, $u_{kl} = 0$ (Eq. VI.9), it can readily be observed that computational efficiency can be enhanced by setting $j = 1$ (i.e., j is set to the column index of \mathbf{U} in Eq. VI.10). In which case, Eq. VI.10 reduces to

$$A_{i1} = \ell_{i1} u_{11}, \quad \text{for } i = 1, 2, \dots, q \quad (\text{VI.11})$$

From Eq. VI.9, it can be noted that $u_{11} = 1$, thus the first column of \mathbf{L} can be given as

$$\ell_{i1} = A_{i1} \quad (\text{VI.12})$$

Following the row-column operation of matrix multiplication and the already known values of the elements of the first column of \mathbf{L} , the first row of the \mathbf{U} matrix can now be computed.

i.2. Compute the first row of the \mathbf{U} matrix: from multiplication of matrices, it can readily be observed that the first row of \mathbf{A} is related to the first row of \mathbf{L} and the j th column of \mathbf{U} as follows

$$\Delta_{1j} = \sum_{k=1}^i \ell_{1k} u_{kj}, \quad \text{for } j = 2, 3, \dots, q \quad (\text{VI.13})$$

Observe that in Eq. VI.13 we take note of the fact that in the first row of matrix \mathbf{U} , $u_{11} = 1$ (Eq. VI.9), hence it need not be part of the row computation. Noting that for $1 < k$, $\ell_{1k} = 0$ (Eq. VI.8) it can readily be observed that setting $i=1$ (which is the row index of matrix \mathbf{L} in Eq. VI.13) would reduce Eq. VI.13 into a simple and computationally efficient form

$$\Delta_{1j} = \ell_{11} u_{1j}, \quad \text{for } j = 2, 3, \dots, q \quad (\text{VI.14})$$

Since $\ell_{1,1}$ is known from *step i.1* (Eq. VI.12), the first row of \mathbf{U} can be given as:

$$u_{1j} = \frac{\Delta_{1j}}{\ell_{11}}, \quad \text{for } j = 2, 3, \dots, q \quad (\text{VI.15})$$

i.3. Compute the second column of matrix \mathbf{L} : from *step i.1* and Eq. VI.4, it follows that

$$\Delta_{i2} = \sum_{k=1}^j \ell_{ik} u_{k2}, \quad \text{for } i = 2, 3, \dots, q \quad (\text{VI.16})$$

Observe that in Eq. VI.16 we take note of the fact that in the second column of matrix \mathbf{L} , $\ell_{12} = 0$ (Eq. VI.8), hence it need not be part of the column computation. Following the same reasoning as in *step i.1*, above, and noting that $j = 2$ and $u_{22} = 1$ (Eq. VI.9), the unknown, ℓ_{i2} , can be given as

$$\ell_{i2} = \Delta_{i2} - \ell_{i1} u_{12}, \quad \text{for } i = 2, 3, \dots, q \quad (\text{VI.17})$$

Similarly, it can be shown that the third column of the \mathbf{L} matrix can be expressed as

$$\ell_{i3} = \Delta_{i3} - \ell_{i1} u_{13} - \ell_{i2} u_{23}, \quad \text{for } i = 3, 4, \dots, q \quad (\text{VI.18})$$

Note that in a numerical computation, the third column of matrix \mathbf{L} can be calculated only after the second row of the \mathbf{U} matrix is computed (presented in *step i.4*). However, the expression for ℓ_{i3} , Eq. VI.18, is presented here for simplicity.

Based on Eqs. VI.12, VI.17, and VI.18, a general expression can be deduced for the j th column of the \mathbf{L} matrix

$$\ell_{ij} = \Delta_{ij} - \sum_{k=1}^{j-1} \ell_{ik} u_{kj}, \quad \text{for } i = j, j+1, \dots, q \quad (\text{VI.19})$$

Note that for $j = 1$, Eq. VI.19 simplifies to VI.12. Noting that k is always less than j , it can be observed that for the general case in which $1 < j$, the j th column of \mathbf{L} is obtained based on elements of \mathbf{L} , ℓ_{ik} , that have already been computed in the preceding steps.

i.4. Compute the second row of matrix \mathbf{U} : From *step i.2* and Eq. VI.4, it follows that

$$\Delta_{2j} = \sum_{k=1}^i \ell_{2k} u_{kj}, \quad \text{for } j = 3, 4, \dots, q \quad (\text{VI.20})$$

Observe that in Eq. VI.20 we take note of the fact that in the second row of matrix \mathbf{U} , $u_{21} = 0$ and $u_{22} = 1$ (VI.9), hence they need not be part of the row computation. Following the same reasoning as in *step i.1*, above, and noting that $i = 2$ and ℓ_{22} is known from *step i.3*, the unknown u_{2j} can then be expressed as

$$u_{2j} = \frac{\Delta_{2j} - \ell_{21} u_{1j}}{\ell_{22}}, \quad \text{for } j = 3, 4, \dots, q \quad (\text{VI.21})$$

Similarly, it can be shown that the third row of the \mathbf{U} matrix can be expressed as

$$u_{3j} = \frac{\Delta_{3j} - \ell_{31} u_{1j} - \ell_{32} u_{2j}}{\ell_{33}}, \quad \text{for } j = 4, 5, \dots, q \quad (\text{VI.22})$$

Based on Eqs. VI.15, VI.21, and VI.22, a general expression can be deduced for the i th row of the \mathbf{U} matrix

$$u_{ij} = \frac{\Delta_{ij} - \sum_{k=1}^{i-1} \ell_{ik} u_{kj}}{\ell_{ii}}, \quad \text{for } j = i+1, i+2, \dots, q \quad \text{and } i < q \quad (\text{VI.23})$$

For $i = q$, Eq. VI.9 shows that all the elements, except the one in the main diagonal of the upper triangular matrix \mathbf{U} (i.e., u_{ii}), are all zero and $u_{ii} = 1$.

Note that for $i = I$, Eq. VI.23 reduces to the form given in Eq. VI.15. Noting that k is always less than i , for the general case in which $I < i$, the i th row of U is obtained based on elements of U , u_{kj} , that have already been computed in the preceding steps.

ii. Compute matrix Φ , Eq. VI.7 (Forward substitution)

As noted in a preceding section, matrix Φ has the same dimension and general form as matrix Δ (Eq. VI.1). Based on Eq. VI.7, elements of the Φ matrix can be computed through forward substitution starting from the first row and proceeding sequentially to the bottom row (*i.e.*, $i=1, 2, \dots, q$). From Eq. VI.8 and the structure of matrix L , it can be observed that the i th row of I is related to the row and column, respectively, of the L and Φ matrices as follows

$$\lambda_{ij} = \sum_{k=1}^i \ell_{ik} \phi_{kj}, \quad \text{for } j = 1, 2, \dots, q \quad (\text{VI.24})$$

Following the same reasoning as that used to obtain a general expression for the i th row of matrix U (Eq. VI.23) and noting that for $i < k$, $\ell_{ik} = 0$ (Eq. VI.8), it can readily be shown that the formula for computing the i th row of matrix Φ is

$$\phi_{ij} = \frac{\lambda_{ij} - \sum_{k=1}^{i-1} \ell_{ik} \phi_{kj}}{\ell_{ii}}, \quad \text{for } j = 1, 2, \dots, q \quad (\text{VI.25})$$

It can be observed that for $i = 1$, Eq. VI.25 reduces to a form analogous to Eq. VI.15. Noting that k is always less than i , for the general case in which $I < i$, the i th row of Φ is obtained based on elements of Φ , ϕ_{kj} , that have already been computed in the preceding steps.

iii. Compute matrix Δ^{-1} , Eq. VI.6 (Back substitution)

As noted in a preceding section, matrix Δ^{-1} has the same dimension and properties as matrix Δ (Eq. VI.1). Based on Eq. VI.6, elements of the Δ^{-1} matrix can be computed through back substitution starting from the bottom row and proceeding sequentially to the first row (*i.e.*, $i=q, q-1, \dots, 1$). Considering Eq. VI.6 and the structure of matrix U , it can be observed that the i th row of Φ is related to the row and column, respectively, of the U and Δ^{-1} matrices as follows

$$\phi_{ij} = \sum_{k=i}^q u_{ik} \sigma_{kj}, \quad \text{for } j = 1, 2, \dots, q \quad (\text{VI.26})$$

In Eq. VI.26, σ_{kj} is element of Δ^{-1} on row k and column j . Following the same reasoning as that used to obtain a general expression for computing matrix U and noting that for $k < i$, $u_{ik} = 0$, it can be shown that the formula for computing the i th row of matrix Δ^{-1} is

$$\sigma_{ij} = \phi_{ij} - \sum_{k=i+1}^q u_{ik} \sigma_{kj}, \quad \text{for } j = 1, 2, \dots, q \quad (\text{VI.27})$$

It can be observed that for $k = q+1$ (i.e. $i=q$), Eq. VI.27 reduces to a form analogous to Eq. VI.12. Noting that for the general case in which $i < q$, k is always less than or equal to q and the i th row of Δ^{-1} , σ_{ij} , is calculated based on elements of Δ^{-1} , σ_{kj} , that have already been computed in the preceding steps.

Summary:

- (i) Eqs. VI.19 and IV.23 are used to compute the L and U matrices from matrix Δ (Eq. VI.4),
- (ii) Eq. VI.25 is used to compute matrix Φ from the L and I matrices (Eq. VI.7), and
- (iii) Eq. VI.27 is used to compute Δ^{-1} from the Φ and U matrices (Eq. VI.6)

Appendix VII. The effect of lateral slope on the broad spatial trends of lateral pressure head

In this section the effect of variations in lateral slope on the spatial trends of lateral pressure head is studied by analyzing the functional relationship between lateral pressure head profile, friction head loss, velocity head, elevation profile, and total head at the lateral inlet.

For a given combination of lateral diameter, pipe absolute roughness, residual discharge, sprinkler spacing, sprinkler hydraulic characteristics, elevation profile, and total head at the inlet, the pressure head profile along a lateral, in which local head losses are assumed negligible, can be expressed as

$$h(x) = (H_0 - Z_0) - h_f(x) - V_h(x) - S_0 x \quad (\text{VII.1})$$

where $h(x)$ is lateral pressure head profile (m); x is distance along the lateral, referenced from the inlet (m); H_0 is total head at the lateral inlet (m) and is considered constant for a simulation problem; Z_0 is elevation of the lateral inlet (m), which is also a constant; $h_f(x)$ is the friction head loss in the lateral segment extending between the lateral inlet and a point at distance x from the inlet (m); $V_h(x)$ is velocity head at distance x from the inlet (m); and S_0 is lateral slope (-), considered here constant. Equation VII.1 states that the pressure head at any given point along a

lateral is given as the difference between the sum of the velocity and pressure heads at the lateral inlet, $(H_0 - Z_0)$, and the sum of the friction head loss, $h_f(x)$, the velocity head, $V_h(x)$, and elevation differential, S_0x .

Experience with hydraulic simulations of laterals show that, typically, the effect of the velocity head, V_h , on pressure head, h , is marginal compared to that of friction head loss, h_f , and lateral elevation differential, S_0x . For instance, simulated data for the five lateral slopes, considered in section 5.6.1, show that on the average h_f is greater than V_h by about two orders of magnitude. Furthermore, the data shows that for the laterals with a nonzero slope, lateral elevation differential, S_0x , on the average is at least eight times greater than V_h and typically it exceeds V_h by an order of magnitude and a half. Thus, Eq. VII.1 can be approximated with Eq. VII.2 without significant loss of accuracy

$$h(x) = (H_0 - Z_0) - h_f(x) - S_0x \quad (VII.2)$$

The general spatial behavior of $h(x)$, (i.e., whether it is increasing or decreasing over the entire length of the lateral or it is increasing over a segment of the lateral and is decreasing over another) can be conveniently evaluated based on the derivative of the pressure head profile with respect to distance along the lateral, given as

$$h'(x) = -h_f'(x) - S_0 \quad (VII.3)$$

In Eq. VII.3, $h'(x)$ is the derivative of the lateral pressure head profile with respect to distance along the lateral, $h_f'(x)$ is the derivative of friction head loss with respect to distance, and S_0 is the derivative of the lateral elevation differential, which is the constant slope of the lateral. Equation VII.3 states that at any given point along the lateral, the slope of the pressure head profile, $h'(x)$, can be approximated by the negative of the algebraic sum of the friction slope, $h_f'(x)$, and the lateral slope.

Note that differentiating $h(x)$, Eq. VII.2, with respect to distance presumes that it is a continuous and smooth function of distance. However, this may not be strictly correct, because the lateral pressure head profile can be discontinuous and may not be smooth at the junction nodes, thus not continuously differentiable over the length of the lateral. These limitations to the differentiability of the lateral pressure head profile are associated with local head losses and a step change in

lateral discharge at the junction nodes. Evidently, local head losses are not considered in the current analyses, thus discontinuity in lateral pressure head profile associated with local head losses are impertinent. However, because of discrete changes in lateral discharges across junction nodes, the friction head loss, $h_f(x)$, and hence pressure head, $h(x)$, functions along a lateral are in theory piecewise linear function of distance (i.e., their graphs consist of line segments with different slopes intersecting at junction nodes). Thus $h_f(x)$, and hence $h(x)$, are not smooth and in effect not differentiable at the junction nodes. Evidently this is theoretically important, however, experience with simulated data shows that the $h_f(x)$ and $h(x)$ curves can be represented in terms of smooth nonlinear functions over the entire length of the lateral with a high degree of accuracy. The implication is that issues related to smoothness, and hence differentiability, of the $h_f(x)$ and $h(x)$ curves at junction nodes are of limited practical significance. Nonetheless, in subsequent development we will adhere to the theoretical requirement relating to function differentiability.

Noting that the $h_f(x)$ function is a piecewise linear function of distance, it can be readily observed that the $h_f'(x)$ function is a step function (i.e., it is discontinuous at the junction nodes and is constant over a lateral pipe segment). In addition, the slope of the pressure head function, $h'(x)$, is the sum of a step function (i.e, $h_f'(x)$) and a constant function, S_0 . Thus the slope of the pressure head function itself, $h'(x)$, is a step function. Furthermore, hydraulic theory shows that for an irrigation lateral with a given slope, the slope of the h_f curve, $h_f'(x)$, is a function of the lateral diameter, pipe absolute roughness, residual discharge, sprinkler spacing, sprinkler hydraulic characteristics, and the difference between total head and elevation at the inlet. Overall, lateral $h_f'(x)$ is positive (i.e., $0 < h_f'(x)$), however, because of the decreasing discharge it is a decreasing function of distance from the lateral inlet. By comparison, lateral slope can take both negative and positive values.

Given the properties of $h_f'(x)$ and S_0 , noted above, interesting observations can be made with respect to the general spatial behavior of the lateral pressure head profile, $h(x)$, by considering a semi-infinite lateral (with an arbitrarily set slope) and taking the limit of $h'(x)$, Eq. VII.3, as $x \rightarrow +\infty$. Accordingly, assuming available total head at the lateral inlet is not limiting, the following limits can be noted

$$\lim_{x \rightarrow +\infty} h_f'(x) = 0 \quad \text{and} \quad \lim_{x \rightarrow +\infty} S_0 = S_0 \quad (\text{VII.4})$$

and then

$$\lim_{x \rightarrow +\infty} h'(x) = -S_0 \quad (\text{VII.5})$$

The implication is that the slope of the lateral pressure head profile, $h'(x)$, approaches $-S_0$ as distance from the lateral inlet increases, but it is not clear whether $-S_0$ is an upper or lower limit to $h'(x)$. Next we will determine that. As noted above $h_f'(x)$ is positive but decreasing function of distance, it then follows from Eq. VII.4 that zero is the lower limit of the friction slope.

Conversely, the negative of the friction slope, $-h_f'(x)$, which is the first term on the right hand side of Eq. VII.3, is negative but increasing function of distance. In other words, $-h_f'(x)$ approaches zero as its upper limit, as distance from lateral inlet increases. Noting that S_0 is a constant, it can then be readily observed from Eq. VII.3 that $h'(x)$ approaches $-S_0$ as its upper limit, as distance from lateral inlet increases.

Based on Eqs. VII.3-VII.5, the algebraic sign of S_0 , and the magnitude (absolute value) of S_0 relative to that of $h_f'(0)$, the following scenarios can be discerned with regard to the general behavior of the lateral pressure head profile, $h(x)$.

(i) *Lateral with an elevation profile that is level or that increases at a constant rate with distance from inlet ($0 \leq S_0$)*

Noting that $h_f'(x) > 0$, from Eq. VII.3 it can be observed that

$$h'(x) < 0 \quad \text{for } x \in [0, +\infty) \quad (\text{VII.6})$$

It then follows that $h(x)$ is a decreasing function of distance over the interval $[0, +\infty)$.

(ii) *Lateral with an elevation profile that decreases at a constant rate with distance from the inlet ($S_0 < 0$):*

The following scenarios can be discerned:

(iia) *The magnitude of lateral slope is sufficiently large, such that $h_f'(0) \leq |S_0|$:*

From Eqs. VII.3 and VII.4 it can be observed that

$$0 \leq h'(x) \quad \text{for } x \in [0, +\infty) \quad (\text{VII.7})$$

thus $h(x)$ is an increasing function of distance over the interval $[0, +\infty)$.

(iib) The absolute value of the lateral slope is such that $|S_0| < h_f'(0)$:

From Eq. VII.3 and VII.4 it can be observed that

$$\left. \begin{array}{l} h'(x) < 0 \quad \text{for } x \in [0, x_{min}) \\ h'(x) = 0 \quad \text{at } x = x_{min}, \quad \text{and} \\ h'(x) > 0 \quad \text{for } x \in (x_{min}, +\infty) \end{array} \right\} \quad (VII.8)$$

where x_{min} is distance (from lateral inlet) at which $h_f = |S_0|$ and hence $h' = 0$ and pressure head is minimum (m).

Equation VII.8 shows that, under the scenario considered here, the lateral pressure head profile decreases with distance from the lateral inlet, reaches a minimum at $x = x_{min}$, and then increases with distance over the interval $x_{min} < x$. Note that x_{min} is a function of the friction slope of the lateral, h_f' (and hence all the factors that affect h_f' , listed above), and the lateral slope.

The results summarized above are important in terms of establishing the general behavior of the lateral pressure head profile as a function of lateral slope and friction slope. However, in practice lateral length and total head at the lateral inlet are finite. Thus the preceding observations need to be modified to take into account these limitations in an actual lateral. In the following section each scenario deduced above is recast into a form applicable to an actual lateral with a finite, but arbitrarily set, length.

(I) Lateral with length, L , and slope, S_0 , such that $0 \leq S_0$:

Note that this is a special case of scenario *i*, described above, where lateral length is finite, thus Eq. VII.6 becomes

$$h'(x) < 0 \quad \text{for } x \in [0, L] \quad (VII.9)$$

It follows from Eq. VII.9 that the lateral pressure head profile, $h(x)$, is a decreasing function of distance over the entire length of the lateral. Thus the maximum and minimum pressure heads occur at the inlet and downstream ends of the lateral, respectively.

(II) Lateral with length, L , and slope, S_0 , such that $S_0 < 0$: Depending on the magnitude of S_0 relative to that of $h_f'(x)$ the following scenarios can be discerned.

(IIa) The absolute value of the lateral slope, S_0 , is sufficiently large, such that $h_f'(0) \leq |S_0|$:

This is a special case of scenario *ii*a, described in a preceding section, where lateral length is finite, thus Eq. VII.7 becomes

$$0 \leq h'(x) \quad \text{for } x \in [0, L] \quad (\text{VII.10})$$

It then follows that the lateral pressure head profile, $h(x)$, is an increasing function of distance over the length of the lateral. Thus, the minimum and maximum pressure heads occur at the inlet and distal ends of the lateral, respectively. Note that such a scenario typically occurs in laterals with steep slopes and/or large diameter pipes, thus may not be common in practice.

(IIb) The friction slope at the lateral inlet, $h_f'(0)$, exceeds $|S_0|$ but $|S_0|$ is sufficiently large, such that $h_f'(x) \leq |S_0|$ over a subinterval of the range $0 < x < L$:

It can be noted that this is a special case of scenario *ii*b, described above, where the lateral has a finite but arbitrarily set length, L , and that $x_{min} < L$. Thus Eq.

VII.8 becomes

$$\left. \begin{array}{l} h'(x) < 0 \quad \text{for } x \in [0, x_{min}) \\ h'(x) = 0 \quad \text{at } x = x_{min}, \quad \text{and} \\ h'(x) > 0 \quad \text{for } x \in (x_{min}, L] \end{array} \right\} \quad (\text{VII.11})$$

Equation VII.11 states that, under the scenario considered here, pressure head decreases with distance from the lateral inlet, reaches a minimum at $x = x_{min}$ (where $h_f = |S_0|$ and $h' = 0$) and then increases with distance to a local maximum at the distal end of the lateral.

Keeping all other factors constant and varying lateral slope only, within realistic ranges, will generally have negligible effects on $h_f(x)$ and $h_f'(x)$. Based on this observation and Eq. VII.3, it can be shown that increasing lateral slope, starting from a small value, will lead to a decrease in x_{min} and an increase in the minimum pressure head

of the lateral. Furthermore, it can be shown using Eq. VII.3 that depending on the relative magnitudes of the lateral slope and the friction slope, the maximum pressure head can occur at either ends of the lateral. For a given hydraulic and geometric configuration of a lateral, relatively small lateral slopes tend to produce a scenario in which the maximum pressure head occurs at the inlet end of the lateral. Conversely, relatively larger slopes tend to produce scenarios in which maximum lateral pressure head occurs at the downstream end of the lateral.

(Iic) The absolute value of the lateral slope, S_0 , is small, such that $|S_0| < h_f'(x)$ over the entire length of the lateral:

This is a special case of scenario *iib*, Eq. VII.8, where lateral length is finite and that $L < x_{min}$. Thus, Eq. VII.8 reduces to the form given in Eq. VII.9. It then follows that under such a scenario, $h(x)$ is a decreasing function of distance over the entire length of the lateral. Thus the maximum and minimum pressure heads occur at the inlet and downstream ends of the lateral, respectively.

(IId) The absolute value of the lateral slope, S_0 , is such that $|S_0| = h_f'(L)$:

This is the same scenario as that of scenario *Iic* above, except that here $x_{min} = L$. Thus $h_f'(L) = |S_0|$, $h'(L) = 0$, and $h(L)$ is the minimum pressure head as defined by theoretical optimality condition. Note that $h(x)$ is characterized in terms of Eq. VII.9.

Note that for all the practical scenarios considered above, the $h(x)$ function generally tends toward $-S_0$ as its upper limit with increasing distance from lateral inlet. Experience with hydraulic simulations show that the negative of the lateral slope provides a good approximation of the upper limit of the slope of the pressure head function. However, for sufficiently long laterals, because of velocity head effect (not taken into account in the current analysis), the actual slope of the pressure head function may marginally exceed the absolute value of the lateral slope.